

Characterization of the Interfacial Fracture of Solvated Semi-Interpenetrating
Polymer Network (S-IPN) Silicone Hydrogels with a Cyclo-Olefin Polymer (COP)

Katie Virginia Murray

Thesis submitted to the faculty of the Virginia Polytechnic Institute and State University in
partial fulfillment of the requirements for the degree of

Masters of Science in
Engineering Mechanics

David A. Dillard – Committee Chairman
Scott W. Case
John J. Lesko

February 2, 2011
Blacksburg, VA 24061

Keywords: Keywords: bridging, confinement, debonding, finite element analysis, interfacial
fracture, S-IPN hydrogels, cyclo-olefin polymers, strain energy release rate

Characterization of the Interfacial Fracture of Solvated Semi-Interpenetrating Polymer Network (S-IPN) Silicone Hydrogels with a Cyclo-Olefin Polymer (COP)

Katie Virginia Murray

ABSTRACT

As hydrogel products are manufactured and used for applications ranging from biomedical to agricultural, it is useful to characterize their behavior and interaction with other materials. This thesis investigates the adhesion between two different solvated semi-interpenetrating polymer network (S-IPN) silicone hydrogels and a cyclo-olefin (COP) polymer through experimental, analytical, and numerical methods.

Interfacial fracture data was collected through the application of the wedge test, a relatively simple test allowing for the measurement of fracture properties over time in environments of interest. In this case, the test was performed at discrete temperatures within range of 4°C to 80°C. Two COP adherends were bonded together by a layer of one of the S-IPN silicone hydrogels. Upon the insertion of a wedge between the two adherends, debonding at one of the two interfaces would initiate and propagate at a decreasing rate. Measurements were taken of the debond length over time and applied to develop crack propagation rate versus strain energy release rate (SERR) curves. The SERR values were determined through the application of an analytical model derived for the wedge test geometry and to take into account the effects of the hydrogel interlayer. The time-temperature superposition principle (TTSP) was applied to the crack propagation rate versus SERR curves by shifting the crack propagation rates with the Williams-Landel-Ferry (WLF) equation-based shift factors developed for the bulk behavior of each hydrogel. The application of TTSP broadened the SERR and crack propagation rate ranges and presented a large dependency of the adhesion of the system on the viscoelastic nature of the hydrogels. Power-law fits were applied to the master curves in order to determine parameters that could describe the adhesion of the system and be applied in the development of a finite element model representing the interfacial fracture that occurs for each system. The finite element models were used to validate the analytical model and represent the adhesion of the system such that it could be applied to future geometries of interest in which the S-IPN silicone hydrogels are adhered to the COP substrate.

ACKNOWLEDGMENTS

I am thankful for my advisor, Dr. David Dillard, for his support and guidance throughout my master's work. He both motivated and challenged me over the past few years and played a significant role in my academic, personal, and professional growth as a graduate student. I appreciate the time and effort he has invested into my success.

I would like to thank my committee members, Dr. Scott Case and Dr. Jack Lesko, for their support and efforts that have played a significant role in my graduate career.

I want to thank the Department of Engineering Science and Mechanics, the Macromolecules and Interfaces Institute (MII), the Institute for Critical Technology and Applied Science (ICTAS), and my sponsors. Thank you for the opportunities provided to me in order for me to perform and finish my research. I want to especially thank Dr. Muhammad Hajj, Lisa Smith, Melissa Nipper, Mac McCord, David Simmons, Darrell Link, Daniel Reed, Dr. Romesh Batra and his students, Tammy Jo Hiner, Don Ohanehi, Dr. Wonho Kim, and Dr. Norman Dowling for your all your help and support.

There are many people that have helped me along the way in my research. I want to thank current and past students of the Adhesion Mechanics Lab that have helped me move through challenges in my work and who were good peers and lab mates: Hitendra Singh, Edoardo Nicoli, Kshitish Patankar, Katherine Finlay, Youliang Guan, Justin Klein, Lei Yan, Chase Siuta, and Brad Miller. I want to give special thanks for the other graduate student on this project, Geoffrey Tizard, and the undergraduates who helped with experimentation, Gina Cruz, Cadence Martin, and Kristin McCord.

Last of all, I want to thank my close friends and family who have been very supportive and encouraging throughout my graduate career. Some of my closest friends really stepped up and offered much needed support throughout my work. Thank you.

Table of Contents

ABSTRACT	ii
ACKNOWLEDGMENTS	iii
List of Figures	vii
List of Tables	xi
Chapter 1 : Introduction	1
Motivation	1
Goals.....	1
Thesis Organization	1
Chapter 2 : Literature Review	4
Introduction	4
Materials.....	4
Substrate X	4
Hydrogel A and Hydrogel B	4
Viscoelasticity and Time-Temperature Superposition (TTSP).....	5
Experimental and Analytical Background of the Wedge Test	7
Simple Beam Theory Solution (SBT).....	7
Adjustments to SBT Model.....	9
Double Cantilever Beam with Finite Thick Adhesive layer (DCB-FTAL).....	9
Double Cantilever Sandwich Beam (DCSB).....	11
Confined Film Model.....	12
Comparison of SBT, DCB-FTAL, and Confined Film Models.....	14
Elastomeric Foundation.....	16
Confinement	17
Numerical Modeling of Interfacial Fracture.....	18
Cohesive Zone Model (CZM)	18
Manual Crack Growth.....	21
Summary	21
Chapter 3 : Experimental Methods.....	22
Introduction	22

Sample Preparation	22
Wedge Test Procedure.....	26
Temperature Control.....	26
Wedge Testing	28
Investigating Aging of Samples.....	29
Investigating Interlayer Confinement	30
Investigating Adherend Parameters.....	32
Summary	34
Chapter 4 : Analytical Model for Characterizing Interfacial Fracture.....	35
Introduction	35
Characterization of the Deflection of the Adherends.....	35
Coordinate System.....	35
Governing Equations	36
Application of Boundary Conditions.....	37
Solution.....	39
Defining the Strain Energy Release Rate (SERR).....	42
Comparison of Analytical Models	43
Summary	43
Chapter 5 : Experimental and Analytical Results	45
Introduction	45
Wedge Test Results.....	45
Application of Analytical Model	46
Comparison of Applying Analytical and SBT Models	46
Crack Rate versus SERR Prior to TTSP	47
Application of Time-Temperature Superposition.....	48
Curve Fitting of the Master curves.....	49
Full Results.....	56
Effects of Aging	58
Effects of Confinement	63
Three-Point Bend Results for Substrate X	66

Summary	67
Chapter 6 : Numerical Modeling	70
Introduction	70
Manual Crack Growth.....	70
Cohesive Zone Model	75
Summary	86
Chapter 7 : Conclusions	87
Key Observations and Conclusions	87
Experimental Methods	87
Analytical Model.....	87
Experimental and Analytical Results	88
Numerical Results	89
Future work.....	89
References.....	91
Appendix A: Determining Mesh Size for Adherends.....	94
Appendix B: Finite Element Cohesive Zone Models	96

List of Figures

Figure 2-1: Example of a Wedge Test Configuration.....	7
Figure 2-2: Load versus Displacement for Constant Displacement.....	8
Figure 2-3: Comparison of Plane Strain Solutions at Different Interlayer Thicknesses over Large Range of Crack Lengths.....	15
Figure 2-4: Comparison of Plane Strain Solutions at Different Interlayer Thicknesses for Range of Short Crack Lengths.....	15
Figure 2-5: Comparison of Correction Factor for Confined Film and DCB-FTAL Solution for Different Interlayer Thicknesses.....	16
Figure 2-6: Linear traction-separation law for cohesive elements.....	19
Figure 3-1: Wedge Test Specimen	22
Figure 3-2: Measuring Thickness of Adherend using Mitutoyo® Digital Indicator	23
Figure 3-3: Adherend with Polycarbonate Spacer attached by PSA.....	23
Figure 3-4: Curing Chamber	24
Figure 3-5: Vacuum Chamber	24
Figure 3-6: Vacuum Pump.....	24
Figure 3-7 : Bottom Substrate with Polycarbonate Spacer and Monomer	25
Figure 3-8: Small Scale Temperature Controller.....	26
Figure 3-9: Thermocouple Cured in Hydrogel Interlayer	26
Figure 3-10: Sample Temperature versus Bath Temperature	27
Figure 3-11: Schematic of the Wedge Test.....	28
Figure 3-12: Side View of the Wedge Test	28
Figure 3-13: Image of Definition of Debond Length	28
Figure 3-14: Sample on Enclosed Scale.....	30
Figure 3-15: Undulating Crack Front during the Wedge Test	31
Figure 3-16: Comparison of Thick to Regular Wedge Test Specimen.....	31
Figure 3-17: Three-Point Bend of Substrate X.....	34
Figure 3-18: Three-Point Bend of Substrate X.....	34
Figure 4-1: Wedge Test Geometry and Dimensions	35
Figure 4-2: Coordinate System for the Analytical Model for the Wedge Test.....	36
Figure 4-3: Moment, M_0 , and Shear Force, F_0 at the Crack Front.....	40

Figure 4-4: Deflection of Adherend along Bonded Length	40
Figure 4-5: Deflection at the Crack Tip versus Crack Length	41
Figure 4-6: Reaction Force versus Crack Length for Different Crack Lengths and Interlayer Thicknesses	42
Figure 4-7: Comparison of Analytical Models over Large Range of Crack Lengths	43
Figure 5-1: Crack Length versus Time for Hydrogel A and Substrate X	45
Figure 5-2: Crack Length versus Time for Hydrogel B and Substrate X.....	45
Figure 5-3: Crack Length versus Crack Propagation Rate for Hydrogel A and Substrate X.....	46
Figure 5-4: Crack Length versus Crack Propagation Rate for Hydrogel B and Substrate X	46
Figure 5-5: SERR versus Crack Length for Hydrogel A and Substrate X.....	47
Figure 5-6: SERR versus Crack Length for Hydrogel B and Substrate X	47
Figure 5-7: Crack Propagation Rate versus SERR Prior to Shifting for Hydrogel A and Substrate X.....	47
Figure 5-8: Crack Propagation Rate versus SERR Prior to Shifting for Hydrogel B and Substrate X.....	47
Figure 5-9: WLF equation-based Shift Factors for the Bulk Behavior of Hydrogel A and Hydrogel B [4]	48
Figure 5-10: Crack Propagation Rate versus SERR Master curve for Hydrogel A and Substrate X at $T_{ref} = 45^{\circ}\text{C}$	49
Figure 5-11: Crack Propagation Rate versus SERR Master curve for Hydrogel B and Substrate X at $T_{ref} = 45^{\circ}\text{C}$	49
Figure 5-12: Demonstration of da/dt versus SERR curve with Threshold, Subcritical, and Critical Regions for Hydrogel A at $T_{ref} = 45^{\circ}\text{C}$	50
Figure 5-13: Crack Propagation Rate versus SERR Master Curve with Fit for Hydrogel A and Substrate X at $T_{ref} = 45^{\circ}\text{C}$	52
Figure 5-14: Crack Propagation Rate versus SERR Master Curve with Fit for Hydrogel B and Substrate X at $T_{ref} = 45^{\circ}\text{C}$	52
Figure 5-15: Crack Propagation Rate versus SERR Master Curve with Fit for Hydrogel A and Hydrogel B Results at $T_{ref} = 45^{\circ}\text{C}$	53
Figure 5-16: Crack Propagation Rate versus SERR Master Curve with Fit for Wedge Test and CTF Results for Hydrogel A at $T_{ref} = 45^{\circ}\text{C}$	55
Figure 5-17: Crack Propagation Rate versus SERR Master Curve with Fit for Wedge Test and CTF Results for Hydrogel B at $T_{ref} = 45^{\circ}\text{C}$	56
Figure 5-18: Crack Propagation Rate versus SERR Prior to Shifting for All Hydrogel A and Substrate X	57
Figure 5-19: Crack Propagation Rate versus SERR Prior to Shifting for All Hydrogel B and Substrate X	57

Figure 5-20: Crack Propagation Rate versus SERR Prior to Shifting for All Hydrogel A and Substrate X Data at $T_{ref} = 45^{\circ}\text{C}$	57
Figure 5-21: Crack Propagation Rate versus SERR Prior to Shifting for All Hydrogel B and Substrate X Data at $T_{ref} = 45^{\circ}\text{C}$	57
Figure 5-22: Hydrogel B Samples with Wedge Inserted at Discrete Times after Curing.....	58
Figure 5-23: Schematic of Bridging	58
Figure 5-24: Bridging during Wedge Testing	59
Figure 5-25: Hydrogel B Samples - Wedge Inserted at Discrete Times after Curing at 22°C	59
Figure 5-26: Hydrogel B Samples Tested at 4°C at Discrete Times after Curing Compared to General Wedge Test Results	60
Figure 5-27: Hydrogel A Samples Tested at 22°C approximately 7 Days after Curing Compared to General Wedge Test Results at $T_{ref} = 45^{\circ}\text{C}$	61
Figure 5-28: Percent Change in Hydrogel Mass over Time	62
Figure 5-29: Hydrogel Interlayer Thickness at Center of Sample versus Time.....	63
Figure 5-30: Specimens of High Confinement (Undulating Crack Front) and Low Confinement (Straight Crack Front)	64
Figure 5-31: Comparison of SERR Values for Specimens with High and Low Confinement.....	64
Figure 5-32: Hydrogel B and Substrate X Test with Thick Adherends.....	65
Figure 5-33: 3-Point Bend Tests on Substrate X in Screw Driven Testing Machine	66
Figure 5-34: Three-Point Test on Substrate X in DMA.....	67
Figure 6-1: Finite Element Configuration for the Manual Crack Growth Method.....	70
Figure 6-2: Prescribed Crack Length for Manual Crack Growth	71
Figure 6-3: Comparison of Compliance versus Crack Length for Different Poisson's Ratio Values	73
Figure 6-4: Compliance at Point of Loading v. Crack Length for Increasing Crack Length for Hydrogel A	74
Figure 6-5: Compliance at Point of Loading v. Crack Length for Increasing Crack Length for Hydrogel B	74
Figure 6-6: Finite Element Configuration for the CZM Method.....	76
Figure 6-7: Nominal Stress versus Strain Curve for Hydrogel B Cohesive Elements	78
Figure 6-8: Nominal Stress versus Strain Curve for Hydrogel A Cohesive Elements.....	79
Figure 6-9: Separation versus Traction Curves for variations in Interface Stiffness and Nominal Stress for the Hydrogel A with $G=0.2\text{Jm}^2$	80
Figure 6-10: Increasing Compliance at Point of Loading with Increasing Displacement and Crack Length for Hydrogel B with $G=0.2\text{Jm}^2$	81

Figure 6-11: Increasing Compliance at Point of Loading with Increasing Displacement and Crack Length for Hydrogel A with $G=0.2J/m^2$	82
Figure 6-12: Compliance versus Crack Length for Variations in Interface Nominal Stress for Hydrogel A with $G=0.2J/m^2$	82
Figure 6-13: Compliance versus Crack Length for Variations in Interface Stiffness for Hydrogel A with $G=0.2J/m^2$	82
Figure 6-14: Damage of Cohesive Elements Ahead of the Crack Tip for Hydrogel A Cohesive Elements with Fracture Energy of $16 J/m^2$	83
Figure 6-15: Cohesive Element Damage.....	84
Figure 6-16: Cohesive Element Damage.....	84
Figure 6-17: Cohesive Element Damage.....	84
Figure 6-18: Cohesive Element Damage.....	84
Figure 6-19: Cohesive Element Damage.....	84
Figure 6-20: Cohesive Element Damage.....	84
Figure 6-21: Max Compliance for $Ga=199kPa$, $G=16J/m^2$, $Tult=308.67kPa$, $\alpha=7$	85
Figure 6-22: Max Compliance for $Ga=340kPa$, $G=16J/m^2$, $Tult=954kPa$, $\alpha=6$	85

List of Tables

Table 1-1: List of Acronyms.....	3
Table 2-1: Differences between Hydrogel A and Hydrogel B.....	5
Table 2-2: DCB-FTAL versus Confined Film for the Wedge Test Configuration.....	14
Table 3-1: Shear Moduli for Hydrogel A with Rate and Temperature.....	32
Table 3-2: Shear Moduli for Hydrogel A and Hydrogel B with Rate and Temperature.....	33
Table 3-3: Selected Substrate X Properties Provided by the Manufacturer.....	33
Table 4-1: Parameters for Demonstration of Analytical Model.....	41
Table 5-1: WLF Equation Coefficients for the Bulk Behavior of Hydrogel A and Hydrogel B.....	48
Table 5-2: Critical and Threshold Parameters from Fitting each Interfacial Fracture Master Curve.....	54
Table 6-1: Finite Element Parameters for Adherends for Manual Crack Growth.....	72
Table 6-2: Finite Element Parameters for Interlayer for Manual Crack Growth.....	72
Table 6-3: Cohesive Element Parameters for Hydrogel B and Substrate X Interface.....	77
Table 6-4: Hydrogel A Parameters and Corresponding Cohesive Element Parameters.....	78

Chapter 1: Introduction

Motivation

Hydrogels have many applications related to the hygiene, agriculture, biomedical, and pharmaceutical fields [1]. Characterization of their material properties, behavior, and interaction with other materials aid in producing and using hydrogels. This research is interested in the adhesion of two different semi-interpenetrating polymer network (S-IPN) silicone hydrogels to a cyclo-olefin polymer (COP). It was desired that each S-IPN silicone hydrogel system adhere to the COP substrate with a weak bond in order for debonding to occur without failure of the materials. The influence of temperature and debond rate on the adhesion of each system was investigated by applying the theory of viscoelasticity and time-temperature superposition principle (TTSP) to the experimental and analytical results and to the development of the finite element model.

Goals

The four components of the overall goal of this project were the following: developing, refining, and applying an experimental method; developing and applying an analytical model for the experimental method; applying TTSP to develop a master curve for each system; and, finally, developing and refining a numerical model.

The goal of the experimental method was to measure the adhesion of each system with considerations for the sensitivity of the hydrogel behavior, the temperature of the specimen, and the rate at which debonding occurs. The goal for the development of the analytical model was to account for the properties and deflections of the hydrogel interlayer and employ boundary conditions appropriate for controlled displacement. A customized model increased the accuracy of the results. The goal of applying TTSP to the analyzed results was to gain a better understanding of the influence of rate and temperature on the adhesion of each system. The two goals of numerical modeling were the validation of the analytical model and the development of a general finite element fracture model. The completion of these goals resulted in the characterization of the two systems of interest and laid a foundation for characterizing similar systems.

Thesis Organization

A background on the materials, methods, and concepts applied throughout the research are introduced and discussed in Chapter 2. Work performed by others in related areas is discussed, compared, and used to create a foundation of knowledge for understanding the research presented. The topics include the materials, theory of viscoelasticity and TTSP, the wedge test, existing analytical models for the wedge test, elastomer confinement issues, and numerical

modeling of interfacial fracture. In addition to the background in Chapter 2, each topic is further discussed in the chapter in which it plays a role.

The experimental methods applied to each system are presented in Chapter 3. The methods for sample preparation, temperature control, testing, and data collection for the wedge tests are presented. In addition, side studies were performed to investigate the effects of time passing after the specimen is cured, the confinement of the hydrogel interlayer, and the parameters of Substrate X.

In Chapter 4, the derivation of the analytical model for the wedge test is presented. The deflections of the adherends and the interlayer were derived and then applied in order to define the SERR. The final model was compared to those presented in Chapter 2 to highlight the differences and similarities between the derived model and existing models.

In Chapter 5, the crack length measurements over time from the experiments are presented. The analytical model from Chapter 4 was applied to determinate the SERR for a given crack length. The crack propagation rates were determined and plotted against the SERR. Applying TTSP, the crack propagation rates were shifted with the Williams-Landel-Ferry (WLF) equation-based shift factors developed for the bulk behavior of each hydrogel. The crack propagation rates were shifted to form a master curve of the crack propagation rate versus SERR. Curve-fitting was performed on each master curve to find parameters to describe the adhesion of each system. In addition to characterizing the adhesion between each hydrogel system and Substrate X, the effects of aging and confinement of the hydrogel interlayer are presented and discussed and the results for the three-point bend testing of Substrate X are presented.

In Chapter 6, finite element models were developed to validate the analytical model derived in Chapter 4 and to model the adhesion between the hydrogel systems and Substrate X.

The methods and results presented are brought together to formulate key observations of these systems and to draw conclusions in Chapter 7. In addition, thoughts and suggestions for future work in this area are presented and discussed.

Due to many of the longer terms within this research, a list of abbreviations is provided for reference.

Table 1-1: List of Acronyms

Beam-On-Elastic-Foundation	BEF
Cohesive Zone Modeling	CZM
Cyclo-Olefin Polymer	COP
Double Cantilever Beam	DCB
DCB with a Finite Thickness Adhesive Layer	DCB-FTAL
Double Cantilever Sandwich Beam	DCSB
Governing Differential Equation	GDE
Kilo Pascal	kPa
Linear Elastic Fracture Mechanics	LEFM
Mega Pascal	MPa
Semi-Interpenetrating Polymer Network	S-IPN
Simple Beam Theory	SBT
Strain-Energy Release Rate	SERR
Time-Temperature Superposition Principle	TTSP
Virtual Crack Closure Technique	VCCT
Williams-Landel-Ferry	WLF

Chapter 2: Literature Review

Introduction

The work presented in Chapter 2 focuses on the adhesion between two solvated semi-interpenetrating polymer network (S-IPN) silicone hydrogels and a cyclo-olefin polymer (COP) substrate. In investigating the adhesion of this system, a better understanding of the materials, theory, and methods is necessary. This chapter focuses on the understanding of the materials of interest: the S-IPN silicone hydrogel systems, Hydrogel A and Hydrogel B, and the COP substrate, Substrate X. A background on viscoelasticity and time-temperature superposition (TTSP) and the basis of the experimental methods for this research is provided. The origin and a simple explanation of the wedge test and the methods for transforming the raw data into useful information about the material behavior are discussed along with the numerical methods applied to model the adhesion of the system. Overall, this chapter provides a basic understanding of the materials and methods used during this research as well as the theory applied for characterizing the adhesion of each hydrogel to Substrate X.

Materials

Substrate X

Substrate X is a COP, which is a class of polyolefins, has a very low surface energy. This characteristic causes adhesive bonding to its surface to be very difficult [2]. This is an advantageous trait in cases where weak bonding is desired, such as with each S-IPN silicone hydrogel and Substrate X. Weak bonding is desired between each hydrogel and Substrate X because debonding should occur without damage to the hydrogel occurring. Other valuable traits of Substrate X for its application in this research are a high glass transition temperature, optical clarity, and low moisture absorption, all of which are characteristics of COPs [3]. These features are beneficial for the system because the high glass transition temperature allows for Substrate X to remain glassy at elevated temperatures, the optical clarity allows for curing the hydrogels and imaging the system, and the low moisture absorption is very good for working with the hydrogels.

Hydrogel A and Hydrogel B

Hydrogels are crosslinked polymers with hydrophilic properties that allow them to absorb large quantities of water [1]. Once in a swollen state, they offer moderate to high physical, chemical, and mechanical stability and have many applications related to the hygiene, agriculture, biomedical, and pharmaceutical fields [1]. A simple hydrogel consists of monomer that is crosslinked [1]. The addition of a second polymerization improves mechanical properties and forms what is referred to as a S-IPN hydrogel [1]. In order to increase gas permeability, the hydrophilic chains of the hydrogels can be interconnected with hydrophobic silicones to make S-

IPN silicone hydrogels [1]. In addition to the second polymerization and the silicones, the hydrogels each contain diluents which are often used to help control the final properties of the hydrogel [1]. Prior to being cured into a hydrogel, Hydrogels A and B are monomer mixes containing a crosslinker, an initiator, and a small variety of monomer components. Hydrogel A and Hydrogel B were previously characterized in the solvated and pre-swollen state [4]. This means water was not added but solvents were present. However, the hydrogels do have solvent.

One of the main differences between the two S-IPN hydrogel systems is that Hydrogel A has a much higher crosslink density than Hydrogel B. Increasing the crosslink density causes an increase in the mechanical properties and for swelling to occur faster due to the restricted polymers allowing for the water to freely move in [5]. Hydrogel A was found to have higher mechanical strength and toughness [4]. There are not comparisons on the rate of swelling between the two hydrogels, but Hydrogel A did show greater solvent loss over time than Hydrogel B [4]. The higher mechanical strength and greater solvent loss with time demonstrate the higher crosslink density of Hydrogel A compared to Hydrogel B.

In addition to the differences caused by the higher crosslink density in Hydrogel A, Hydrogel B was found to have relatively little to no viscoelastic behavior and less of a response to changes in temperature compared to Hydrogel A. This may be due to the much lower glass transition temperature of Hydrogel B compared to Hydrogel A. The two hydrogels have similar silicone content but Hydrogel B has a solvent level twice that of Hydrogel A. Some of these comparisons are presented in Table 2-1[4].

Table 2-1: Differences between Hydrogel A and Hydrogel B [4]

		Hydrogel A	Hydrogel B
Solvent Content	% <i>Weight</i>	21	42
Silicone Content	% <i>Weight</i>	30-40	30-40
Glass Transition Temperature	°C	-12	-90

The difference between the two hydrogel systems is further discussed and understood with the characterization of the adhesion of each hydrogel system with Substrate X.

Viscoelasticity and Time-Temperature Superposition (TTSP)

Viscoelasticity is a theory that takes into account elasticity, flow, and molecular motion in order to investigate the time-dependence of a material's properties [6]. Viscoelasticity can also be applied to investigate the adhesion between the S-IPN silicone hydrogels and Substrate X, because the adhesion is not only dependent on the interfacial interactions but also on the viscoelastic properties of the hydrogels [7]. Therefore, the viscoelastic nature of the hydrogel is important in the characterization of the adhesion of the system described.

When characterizing viscoelastic materials, TTSP is a useful tool that allows for mechanical tests at different temperatures to be used to estimate a mechanical property of interest as a function of time [8]. This can be done because of the dependence of the molecular behavior of viscoelastic materials on both time and temperature. As the amount of time a load or a strain is applied increases, the molecules relax and have a greater amount of movement, causing the behavior of the material to change [8]. This relaxation can be described by the relaxation time, τ . Increasing the temperature also enhances the molecular mobility and has the same effect on the behavior as a constant applied load [8]. The similar effects of increasing, or decreasing, the time and temperature allow for correlating behavior due to change in temperature and change in time [8]. An example of a parameter dependent on both the temperature and time is the relaxation modulus, $E(t, T)$, estimated by Equation (2-1) [8].

$$E(t', T_0) = E(t = a_T t', T) \quad (2-1)$$

Equation (2-1) takes the relaxation modulus measured at time t and temperature T and shifts it to the reference temperature T_0 that relates to the new time t' [8]. The shift factor $a_T = \tau/\tau_0$ is the ratio of the original relaxation time to the new relaxation time [8]. The relaxation modulus can be collected over a time t at various temperatures and then all the values can be shifted to a reference temperature in order to cover a range of time much greater than that tested. The results would be a master curve of the relaxation modulus as a function of time. Master curves are curves that are built from data sets collected at different temperatures but over the same periods of time, or same rates. Data collected at temperatures higher than the chosen reference temperature are shifted to longer times, or smaller rates, and data collected at temperatures lower than the chosen reference temperature are shifted to shorter times, or higher rates [8]. The data collected at the reference is not shifted [8].

By taking the logarithm of the relationship between of shift factor, the time the parameter is being shifted to, and the time the parameter was measured at, the new time can be expressed by Equation (2-2) [8].

$$\log(t') = \log(t) - \log(a_T) \quad (2-2)$$

Such shift factors are typically found experimentally or using the Williams-Landel-Ferry (WLF) equation above T_g [8]. To find the shift factors experimentally, they are estimated, applied, and then adjusted until they create a smooth master curve. The WLF equation, originally an empirical equation that can be derived from Doolittle's equation for viscosity of a liquid, is often used to establish the shift factors as a function of the temperature at which the data is collected,

$$\log(a_T) = \frac{-C_1(T - T_{ref})}{C_2 + (T - T_{ref})} \quad (2-3)$$

where C_1 and C_2 are constants that depend on the material and T_{ref} is the reference temperature [8]. The WLF equation is only valid above the glass transition temperature of a material, T_g , but it is often applied in a modified manner to data collected below the glass transition temperature [8]. The appropriate equation for determining a fit for the shift factors depends on the test conditions, the material properties, and the information that is desired. If the data is shifted experimentally, it is important to establish a relationship between the shift factors and the corresponding temperatures.

Application of TTSP and the shifting of data are useful when working with, characterizing, and understanding viscoelastic materials. However, TTSP is also useful for characterizing and understanding the adhesion of a system containing one or more viscoelastic materials. Bistac, Guillemenet, and Schultz investigated a system with a viscoelastic adhesive and established a quantitative relation between the rate dependence of the strain energy release rate (SERR) and the rate dependence of the modulus of the adhesive. They concluded that the viscoelastic behavior of the adhesive governed the adhesive behavior of the system [7]. This led to the conclusion that TTSP can be applied when characterizing interfacial fracture for a system in which at least one of the materials is viscoelastic.

Experimental and Analytical Background of the Wedge Test

The Boeing wedge test is a fairly simple and useful method described in both ASTM 3762 and ISO 10354 that is often implemented to investigate mode I fracture [9-11]. An example of a wedge test configuration is shown in Figure 2-1,



Figure 2-1: Example of a Wedge Test Configuration

where t is the adherend thickness, Δ is the thickness of the wedge, and a is the crack length. During the test, a wedge is inserted between two adhesively bonded adherends and causes the two adherends to bend. The energy stored in the deformed adherends provides the driving force to cause a crack to form and grow between the two adherends [9-12]. As the crack between the two adherends propagates, the crack area increases and new surfaces are created that consume energy [13].

Simple Beam Theory Solution (SBT)

Griffith explained the behavior of a crack in a body using an energy balance. He proposed that the strain energy of the cracked body decreased by an amount equal to the increase in the surface energy [13, 14]. The SERR, expressed by \mathcal{G} , is the energy that is released per unit area of new surface area and can be described by the change of the total energy of the system with respect to

the change in the crack area [13, 14]. The SERR is dependent on the geometry, materials, and loading of the system [15]. For the wedge test configuration, the change in the total energy of the system can be described by the change in the elastic energy of the system through the application of linear elastic theory [13]. The graph in Figure 2-2 shows the change in the potential energy of the system, Π , with the change in the crack length when linear elastic fracture mechanics (LEFM) is applied to describe a linear relationship between the load, P , and the constant displacement, δ , applied to the system during the wedge test [13].

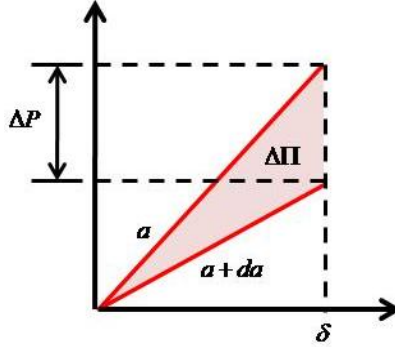


Figure 2-2: Load versus Displacement for Constant Displacement

The applied displacement is the difference of the wedge and interlayer thicknesses. As the crack length, a , increases at constant applied displacement, the compliance of the system increases. The SERR is defined as a function of the compliance of the system, C , shown in Equation (2-4), by applying the relationship in Figure 2-2 [14].

$$\mathcal{G} = -\frac{\partial \Pi}{\partial A} = -\frac{\delta}{2} \frac{\partial P}{\partial A} = -\frac{\delta^2}{2} \frac{\partial}{\partial A} \left(\frac{1}{C} \right) \quad (2-4)$$

The debonded area, $A = ba$, is the new surface area produced as the crack length increases, where b is the width of the bonded area [16]. An analytical model for the wedge test can be derived from Equation (2-4) by defining the compliance of the system using the geometry of the wedge test. The compliance can be defined using one of many methods including simply beam theory (SBT), which is recommended in ASTM D3762 and ISO 10354 [10, 11]. The mode I SERR for the wedge test using SBT is defined in Equation (2-5),

$$\mathcal{G}_{SBT} = \frac{9EI\delta^2}{4ba^4} \quad (2-5)$$

where E and $I = bt^3/12$ are the modulus and second moment of area of the cross section of the adherends, respectively. The SBT solution assumes the adherends are effectively clamped at the crack tip and neglects the rotation and displacement at the crack tip [16, 17]. Error occurs during the application of the SBT solution because it neglects the contribution of the adhesive. Methods

to reduce this error include corrected beam theory, experimental compliance method, and the addition of an elastic foundation in the bonded region that permits deflection and rotation [16].

Adjustments to SBT Model

Corrected beam theory is applied by subtracting a correction term \hat{a} from the crack length before applying Equation (2-5) to find the SERR [16]. To determine the correction term, the cubic root of the experimentally measured compliance is plotted against the measured crack length. The negative crack length value for zero compliance is determined as the correction term.

For the experimental compliance method, the experimentally collected compliance is plotted against the corresponding measured crack lengths on paper and a power law fit is performed in order to find the compliance as a function of the crack length [16, 17]. This resulting compliance function is applied to Equation (2-4) to find the SERR as a function of the crack length.

The corrected beam theory and experimental beam theory work well in accounting for an adhesive of finite thickness as they are methods for tailoring the solution to a given system. However, these methods can be very time consuming in that they involve collecting data to develop the solution. For this reason, others have developed analytical models that account for the behavior of the adhesive of finite thickness.

Double Cantilever Beam with Finite Thick Adhesive layer (DCB-FTAL)

Kanninen developed a beam-on-elastic-foundation (BEF) solution for the double cantilever beam (DCB) fracture specimen that accounted for behavior in the region beyond the crack tip [18]. This was done by considering the region without the crack present as an adherend resting on a Winkler foundation [18]. Kanninen's solution was developed for cohesive fracture to take into account the effects of transverse stresses and strains and for rotations around the crack tip [18]. Although for cohesive fracture, the BEF model has often been a basis for similar fracture cases including those for interfacial fracture with a finite thick adhesive [19].

One example would be the double cantilever beam with a finite thickness adhesive layer (DCB-FTAL) solution by Komatsu and Sasaki [19]. The DCB-FTAL solution was formulated to account for the effects of the adhesive of finite thickness on the compliance of the system [19]. This solution was developed by considering one of the adherends as a beam on a double layered elastic foundation in the bonded region where one of the two layers was prescribed as half of the adhesive and the other was prescribed as half the other adherend [19]. The double layered foundation was considered as infinite rows of elastic springs that provide a reaction force, $q(x)$, in the bonded region that is described by Equation (2-6),

$$q(x) = W(x) \left(\frac{2bEE_a}{2hE + tE_a} \right) \quad (2-6)$$

where E_a is the elastic modulus and h is half the thickness of the adhesive, respectively, and t is the thickness of the adherends [19]. The governing differential equation (GDE) for the deflection of the adherend in the DCB-FTAL solution is the same as that for the BEF model with the exception of the definition of the characteristic root. Defined in Equation (2-7), the GDE employs simple beam theory in the debonded region and a Winkler foundation in the bonded region, as in Kanninen's BEF model,

$$\frac{d^4W}{dx^4} + 4\lambda^4 H(x)W = 0 \quad \text{where} \quad H(x) = \begin{cases} 1 & \text{Debonded } (x < 0) \\ 0 & \text{Bonded } (x > 0) \end{cases} \quad (2-7)$$

where $W(x)$ is the deflection of the adherend and λ is the characteristic root defined by Equation (2-8) [19].

$$\lambda_{FTAL} = \frac{1}{t} \left(\frac{6tE_a}{2hE + tE_a} \right)^{\frac{1}{4}} \quad (2-8)$$

The solution to Equation (2-7) was determined by making similar assumptions as for the classical BEF solution: the solution decays for long crack lengths, continuity at the crack tip, the unloaded end is a free end, and a shear force acts at the point of loading [18, 19]. The solution was assumed to decay by having the deflection, slope, and bending moment equal zero at the unloaded end of the specimen [19]. Continuity was applied by equating the deflection, slope, and bending moment at the crack tip [19]. In addition to the conditions similar to the BEF model, the sum of the reaction force for the length of the bonded area was considered equal to the load applied as defined in Equation (2-9) [19].

$$P = \int_0^{\infty} q(x) dx \quad (2-9)$$

The resulting deflection of the adherend was determined to be that shown by Equations (2-10) and (2-11) [19].

$$\text{(Debonded)} \quad x < 0: \quad W_{FTAL}(x) = \frac{6P}{Ebt^3} \left(\frac{x^3}{3} + ax^2 - \frac{(1+2a\lambda)x}{\lambda^2} + \frac{1+a\lambda}{\lambda^3} \right) \quad (2-10)$$

$$\text{(Bonded)} \quad x > 0: \quad W_{FTAL}(x) = \frac{6P}{Ebt^3} e^{-\lambda x} \left(\left(\frac{1}{\lambda^3} + \frac{a}{\lambda^2} \right) \cos \lambda x - \left(\frac{a}{\lambda^2} \right) \sin \lambda x \right) \quad (2-11)$$

The compliance at the point of loading was determined and applied to Equation (2-4) to determine the SERR for the system, shown in Equation (2-12),

$$\mathcal{G}_{FTAL} = \frac{9EI\delta^2}{4ba^4} \left[\frac{4(a\lambda)^4 (1+a\lambda)^2}{\left(3aEt^2\lambda^3 + 5G_a \left(3 + 6(a\lambda) + 6(a\lambda)^2 + 2(a\lambda)^3\right)\right)^2} \right] \quad (2-12)$$

where G_a is the shear modulus of the adhesive [19]. The DCB-FTAL solution is compared to the simple beam solution in Figure 2-3.

Double Cantilever Sandwich Beam (DCSB)

Another approach to the issue of a finite thick adhesive would be to consider the adhesive as a confined adherend such as the double cantilever sandwich beam (DCSB) specimen developed by Lefebvre [20]. The DCSB specimen consists of a soft adherend that is adhered to and constrained between the rigid adherends, and the adhesion measured for the system is between the soft and rigid adherends [20]. This is similar to the variation of the wedge test applied in this research in that the interest is in the adhesion between the hydrogel and Substrate X adherend and not between the two Substrate X adherends via the hydrogel. A closed-form BEF solution based on the work by Hetenyi was developed in order to analyze DCSB results with the foundation stiffness predicted by implementing a procedure by Gent [20]. The compliance at the point of loading was determined by considering the deflection and rotation of the crack tip in addition to SBT deflection of the adherend. The solution for the compliance at the point of loading is expressed by Equation (2-13) for the case in which the beam is considered long by equating the non-dimensional quantity $\rho = \lambda(L - a)$ to π .

$$C_{DCSB} = \frac{2\left(a^3k + 6EI\lambda\left(\text{Coth}(\pi) + 2a\lambda(1 + \text{Coth}(\pi)\lambda)\right)\right)}{3EI k} \quad (2-13)$$

The characteristic root, λ , is expressed by Equation (2-14).

$$\lambda^4 = \frac{k}{4EI} \quad (2-14)$$

The foundation stiffness, k , was defined as twice the product of the shape factor, f_c , and elastic modulus of the interlayer and the modulus. The foundation stiffness established a dependency of the solution on the parameters of the confined adherend.

Equations (2-13) and (2-14) are applied to Equation (2-4) in order to find the SERR of the system. The solution is then Equation (2-15).

$$G_{DCSB} = \frac{9EI\delta^2}{4ba^4} \left[\frac{a^4k(a^2k + 4EI\lambda^2(1 + \text{Coth}(\pi)\lambda))}{(a^3k + 6EI\lambda(\text{Coth}(\pi) + 2a\lambda(1 + \text{Coth}(\pi)\lambda)))^2} \right] \quad (2-15)$$

This solution agreed well with the experimental results in which the crack length of the DCSB specimen was manually increased and the loads acting on and the strain of the adherends was measured [20].

Confined Film Model

Another model that can be applied to the wedge test with a finite thick adhesive is the confined film model developed by Ghatak et al [21]. The confined film model considered a flexible plate on an elastic film that was adhered to a very rigid substrate [21]. The purpose was to measure the adhesion between the confined elastic layer and the flexible plate while taking into account the material and geometrical parameters of both the film and plate [21]. The adhesion between the confined elastic layer and the flexible plate was measured while taking into account the material and geometrical parameters of both the film and plate [21]. Although the confined film model considers the case of a single cantilever beam test, it can be applied to approximate the wedge test solution by considering the configuration as half of the wedge test. For the confined film model, the elastic film was assumed to be linearly elastic, loaded in plane strain, and incompressible by Equation (2-16) [21].

The film was assumed to be perfectly bonded to the rigid slide underneath the film such that there are no deflections of the film at this interface as shown by Equation (2-17),

$$\frac{\partial u}{\partial x} + \frac{\partial w}{\partial z} = 0 \quad (2-16)$$

$$u(x,0) = 0 \quad w(x,0) = 0 \quad (2-17)$$

where $u(x, z)$ and $w(x, z)$ are the components of displacement within the film in the x and z directions, respectively [21]. Ghatak et al. defined the pressure field within the film using the Navier-Stokes equation for incompressible fluids and reduced the definition to Equation (2-18) by applying the lubrication approximation for thin film flow,

$$\frac{\partial q}{\partial x} = G_a \frac{\partial^2 u}{\partial z^2} \quad \frac{\partial q}{\partial z} = 0 \quad (2-18)$$

where q is the hydrostatic restoring pressure in the film (2-21) [21]. The lubrication approximation for thin film flow exploits the significant difference in the thickness of the film to the length and aligns with the assumptions that the film was loaded in plane strain [21, 22]. By

assuming small deflections, the deflection of the film at the interface with the plate was assumed to be equal to the deflection of the plate, as shown in Equation (2-19),

$$w(x, h) = W(x) \quad (2-19)$$

where $W(x)$ is the deflection of the plate [21]. By integrating Equation (2-18) twice and applying the boundary conditions described, the deflection of the film in the x-direction and the GDE of the bonded region were defined by Equation (2-20) and Equation (2-22), respectively [21]. In the debonded region, the plate and film do not interact, allowing for simple beam theory to apply in this region, as shown in Equation (2-21) [21].

$$u(x, z) = \frac{D}{2G_a} \frac{\partial^5 W(x)}{\partial x^5} (z^2 - hz) \quad (2-20)$$

$$x > 0: D \frac{\partial^4 W(x)}{\partial x^4} = 0 \quad (2-21)$$

$$x < 0: \frac{\partial^6 W(x)}{\partial x^6} - \lambda^6 W(x) = 0 \quad \text{where} \quad \lambda^6 = \frac{12G_a}{Dh^3} \quad (2-22)$$

The flexural rigidity of the plate, D , is defined by Equation (2-23),

$$D = \frac{Et^3}{12(1-\nu^2)} \quad (2-23)$$

where ν is the Poisson's ratio of the plate. This solution was developed for both perfect adhesion and perfect slippage between the film and plate. It is important to note that the solution for perfect adhesion is presented in this summary. Similar to other models such as the BEF and DCB-FTAL, continuity was established at the crack tip and the solution was assumed to decay towards the fixed end [18, 19, 21]. Continuity was applied by equating the deflection, slope, bending moment, and shearing force at the crack tip [21]. The solution was assumed to decay by letting the deflection, slope, bending moment, and shearing force approach zero as approaching the far end of the bonded area [21]. Since this model was designed for the case of an applied displacement, the point of loading was assumed to be a hinged support with a known displacement of the spacer's thickness with no moment acting at that point [21]. The pressure gradient at the crack tip was assumed to be zero due to the pressure in the film becoming maximally tensile in the area near the crack tip [21]. The deflection of the plate and the deflection within the film were determined by applying these conditions to Equations (2-21) and (2-22). Once the deflection of the plate was established, the total energy was determined by summing the bending energy of the plate, the elastic energy in the film, and the interfacial energy of adhesion. The change of the total energy with respect to the crack length was set to zero to solve for the SERR, as shown in Equation (2-24) [21].

$$\frac{\partial \Pi}{\partial a} = \frac{\partial}{\partial a} \left[\int_{-\infty}^a \frac{D}{2} \left(\frac{d^2 W}{dx^2} \right) dx + \int_{-\infty}^0 \int_0^h \frac{G_a}{4} \left(\frac{\partial u}{\partial z} + \frac{\partial w}{\partial x} \right)^2 dz dx + \mathcal{G}a \right] = 0 \quad (2-24)$$

The solution for the SERR from solving Equation (2-24) was the product of the classical solution for the single cantilever beam and a correction factor, $g(a/\lambda)$, defined by Equation (2-25) [21].

$$g(a/\lambda) = \frac{8(a/\lambda)^4 \left(12 + 46(a/\lambda) + 72(a/\lambda)^2 + 56(a/\lambda)^3 + 21(a/\lambda)^4 + 3(a/\lambda)^5 \right)}{3 \left(6 + 12(a/\lambda) + 9(a/\lambda)^2 + 2(a/\lambda)^3 \right)^3} \quad (2-25)$$

By considering the configuration of the confined film model as half of the wedge test, the solution can be transformed to be the product of the simple beam solution of the wedge test and the correction factor, $g(a/\lambda)$, as shown by Equation (2-26). This allows for using the confined film model as an approximate solution to the wedge test with an adhesive of finite thickness.

$$G_{Film} = \frac{9D\delta^2}{a^4} g(a/\lambda) \quad \text{where} \quad \lambda^6 = \frac{12G_a}{D(h/2)^3} \quad (2-26)$$

Comparison of SBT, DCB-FTAL, and Confined Film Models

The most significant differences between the DCB-FTAL, DCSB, and confined film models are laid out in Table 2-2.

Table 2-2: DCB-FTAL versus Confined Film for the Wedge Test Configuration [19-21]

	DCB-FTAL	DCSB	Confined Film
Order of GDE	4	4	6
Characteristic Root	$\lambda_{FTAL} = \frac{1}{t} \left(\frac{6tE_a}{2hE + tE_a} \right)^{\frac{1}{4}}$	$\lambda = \left(\frac{E_a}{6EI} \left(4 + \left(\frac{b}{h} \right)^2 \right) \right)^{\frac{1}{4}}$	$\lambda = \left(\frac{12G}{D(h/2)^3} \right)^{\frac{1}{6}}$
Loading	Force P at x = - a	Force P at x = - a	Displacement Δ at x = a
Interlayer	Series of Discrete Springs	Classical Elastic Foundation	Continuous and incompressible film

The difference in the order of magnitude of the GDE relates to how the interlayer was considered. Considering the interlayer as a simple series of discrete springs resulted in a fourth-order equation combining simple beam theory and Winkler foundation. Considering the interlayer as an elastic film resulted in a sixth-order equation combining classical plate theory and lubrication theory. Due to considering the interlayer as a continuous rather than discrete system, the confined film model has a greater order GDE than the DCB-FTAL and DCSB

models. The confined film model, however, was derived for the case of a bending plate from an elastic film on a rigid substrate and further changes would need to be applied in order to derive a similar model for the wedge test.

A comparison of SBT, DCB-FTAL, DCSB, and Confined Film models is shown in Figure 2-3 for constant applied displacement and the case of plane strain.

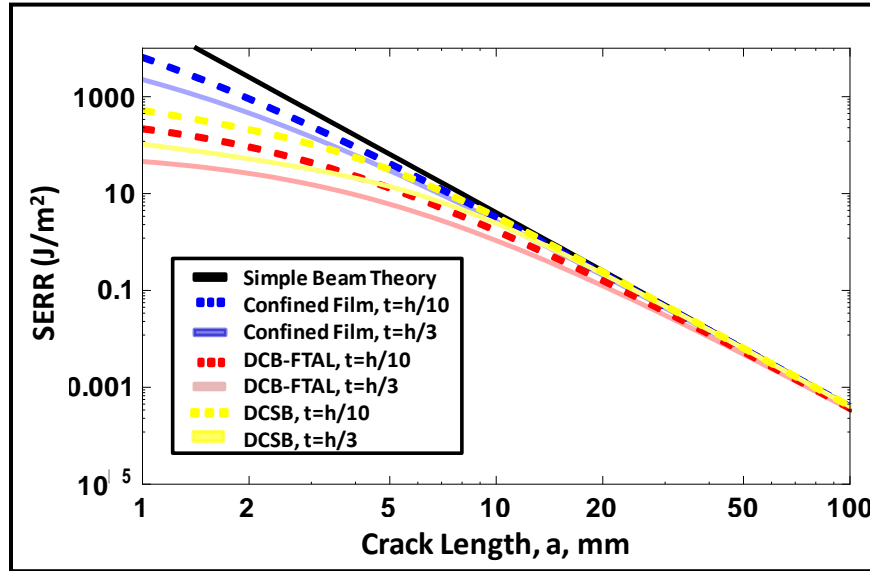


Figure 2-3: Comparison of Plane Strain Solutions at Different Interlayer Thicknesses over Large Range of Crack Lengths

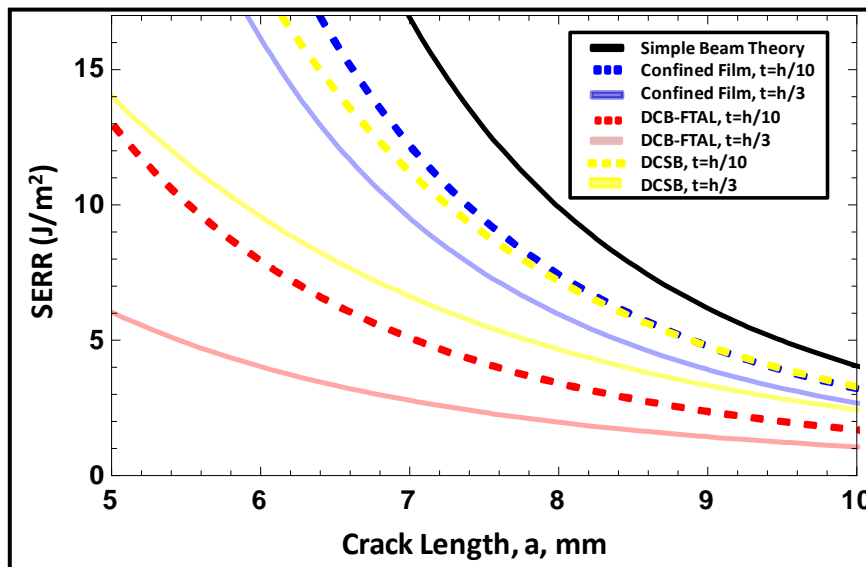


Figure 2-4: Comparison of Plane Strain Solutions at Different Interlayer Thicknesses for Range of Short Crack Lengths

There is a significant difference between the models for short crack lengths that decreases as the crack lengths increase. This difference is due to accounting for the interlayer and reduces as the

crack length increases. The DCB-FTAL model reduces the simple beam theory solution by a greater amount than the DCSB and confined film models. To better understand the role of the crack length and the hydrogel thickness for each of the models, the correction factors are observed with increasing crack length in Figure 2-5. The correction factor was determined for each solution by dividing each solution by the simple beam solution.

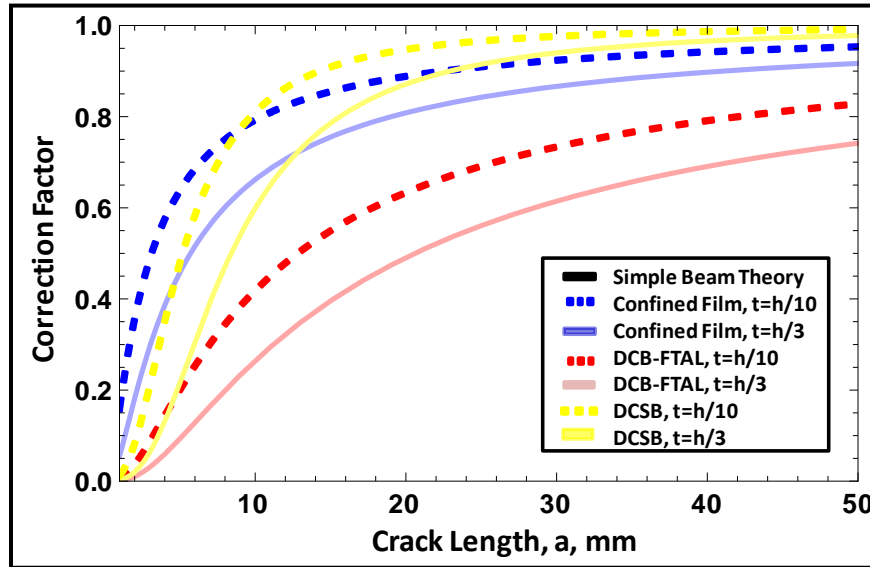


Figure 2-5: Comparison of Correction Factor for Confined Film and DCB-FTAL Solution for Different Interlayer Thicknesses

The correction factor approaches, but does not necessarily reach, unity as the crack length increases. This represents each solution approaching the SBT solution as the crack length increases, as expected and observed in Figure 2-3. The effect of the interlayer on the SERR decreases as more of the adherend is no longer bonded. In addition, the initial slope for each correction factor in Figure 2-5 increases as the interlayer thickness decreases. This is due to the solution approaching the SBT solution at a greater rate as the thickness decreases. This is expected since the effect of the interlayer in the behavior of the system will decrease as more as the interlayer thickness decreases, causing the behavior of the system to approach that of the SBT model. The correction to the SBT decays the fastest for the DCSB model.

Elastomeric Foundation

A very similar model to the confined film model but with a very different approach is the general solution for bending plates on an elastomeric foundation developed earlier by Dillard [23]. Dillard's solution for a bending plate on a relatively thin elastomeric foundation, like the confined film solution, provides an improvement over the Winkler foundation and reduces error by considering the foundation as continuous [23]. Dillard began with classical plate theory GDE as shown in Equation (2-27),

$$\frac{\partial^4 W(x, y)}{\partial x^4} + 2 \frac{\partial^4 W(x, y)}{\partial x^2 \partial y^2} + \frac{\partial^4 W(x, y)}{\partial y^4} = \frac{p - q}{D} \quad (2-27)$$

where p is the distributed load applied to the plate and q is the restoring pressure [23]. For the cases of the DCB or wedge test, there is no distributed load. The incompressibility of the foundation was defined by Equation (2-28) [23].

$$\frac{\partial u}{\partial x} + \frac{\partial v}{\partial y} = \frac{3}{2} \frac{W(x, y)}{h} \quad (2-28)$$

The variation in the length and thickness directions equates to the product of the shape factor of the interlayer and the strain in the thickness direction [23]. In addition to the incompressibility, the shear stresses and strains that occur in the interlayer were defined by Equation (2-29) and the normal stresses were assumed to be equal to each other and to the restoring pressure [23].

$$\frac{\partial \sigma_x}{\partial x} = -\frac{\partial q}{\partial x} = \frac{8G}{h^2} u \quad \frac{\partial \sigma_y}{\partial y} = -\frac{\partial q}{\partial y} = \frac{8G}{h^2} v \quad (2-29)$$

The definition of the normal stresses assumes the elastomer bulges under pressure in a parabolic fashion, similar to the discussion in other works on bulging of bonded elastic blocks [24]. Equation (2-29) was differentiated twice to find the Laplacian of the pressure gradient shown in Equation (2-30) which was substituted back into Equation (2-27) [23].

$$\frac{\partial^2 q}{\partial x^2} + \frac{\partial^2 q}{\partial y^2} = -\frac{8G}{h^2} \left(\frac{\partial u}{\partial x} + \frac{\partial v}{\partial y} \right) \quad (2-30)$$

If the solution is assumed independent of the width direction, the GDE of the system described by Equation (2-27) becomes the GDE for the confined film model described by Equation (2-22) [23]. Although the two models are based on very different approaches, the confined film and elastomeric foundation models have the same GDE and characteristic root. This provides further confidence that Equation (2-22) is the foundation for the analytical model for the wedge test with a finite thickness elastomeric interlayer.

Confinement

Another interest is the confinement of the hydrogels when adhered between the two COP adherends. When the adhesive is highly confined, the crack front relieves stress by extending forward periodically, causing the crack front to have an undulating pattern [25]. Adda-Bedia and Mahadevan studied the same geometry as Ghatak for thin elastomeric films [25]. They found that the elastic instability was dependent on the ratios involving the thicknesses of the film and the stiffness of the plate and the film. They were able to take these ratios and derive a confinement parameter, α , to describe the confinement of the film [25].

$$\alpha = \left(\frac{D}{Gh^3} \right)^{1/3} \quad (2-31)$$

It was found that there was some critical confinement threshold such that the crack front goes from undulating to straight as the confinement decreases [25]. For a given set of materials, as the ratio of the adhesive thickness to that of the adherend thickness increases, the confinement decreases. The confined film model was derived for the case of a highly confined elastomer. However, comparison of the effect of interlayer thickness and confinement is of interest. According to the analytical models in Figure 2-5, the effect of the interlayer on the solution decreases as the thickness decreases while keeping other properties of the specimen, such as the adherend thickness, constant. It can be assumed that increasing confinement results in decreasing effects of the interlayer on the system. Although confinement has been shown to affect the crack front geometry, possible effects on the adhesion of the system are unknown.

Numerical Modeling of Interfacial Fracture

Numerical methods are useful for finding an approximate solution to more complex problems [26]. One can apply a generic model that agrees with experimental results to other systems and can be used to find preliminary results prior to more testing and can be applied to other geometries [26]. The finite element method is a numerical method in which the entire domain of the system, governed by differential equations, is broken down into subdomains, governed by algebraic equations [26]. The subdomains are referred to as the finite elements and are connected to one another by nodes to build the finite element mesh [26]. The solution of the problem is approximated by developing solutions over the elements [26].

Cohesive Zone Model (CZM)

A useful method for modeling interfacial fracture is cohesive zone modeling (CZM), a damage mechanics approach which involves modeling the interface with a damageable material that fails and results in the crack increasing [27, 28]. An initial flaw is not necessary for CZM, but the crack can only occur where cohesive zone elements or surfaces are present [27]. CZM is fundamentally based on energy principles and a traction-separation law [28-34]. It has often been implemented in finite element analysis programs such as Abaqus with cohesive surfaces or with cohesive elements that follow a cohesive law such as that shown in Figure 2-6 [27-32, 35, 36].

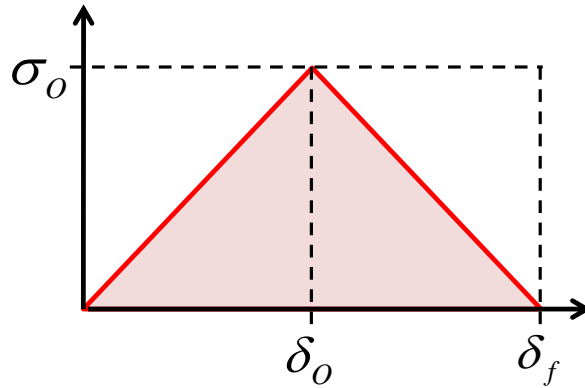


Figure 2-6: Linear traction-separation law for cohesive elements

The onset of damage occurs when the traction acting on the cohesive element reaches the maximum value of σ_0 , which is referred to as the strength of the interface, and the separation of δ_0 . The traction then reduces as damage accumulates and complete failure occurs when the traction is zero at the separation of δ_f [27-32, 35, 36]. An effective thickness of unity is often applied for cohesive elements. This leads to interchanging the stress and traction, the strain and separation, and the elastic modulus and stiffness. Although Figure 2-6 depicts a linear relationship between the strength of the interface and the separation, this relationship can be depicted in other forms as well such as an exponential form, trapezoidal form, sinusoidal form, and others depending on the behavior of the adhesion [27-32, 35, 36].

Many different methods have been developed in order to determine the parameters of cohesive elements. This is an area of continual interest due to the difficulties in estimating the parameters of the cohesive elements. Methods applied in Chapter 6 are those performed by Diehl and Turon [29, 31]. Diehl used a penalty cohesive zone finite element approach in which CZM was converted into a ‘rigid’ assumption similar to the Griffith criterion so that the traction-separation law was only dependent on the critical strain energy release rate [29]. Turon developed a methodology to determine the parameters of the cohesive element while accounting for the size of the cohesive element and the length of the cohesive zone [31]. A method of estimating the minimum penalty stiffness, K_{eff} , for when coarse meshes are desired was also developed [31]. Both Diehl and Turon applied the linear traction-separation law in Figure 2-6 in which the slope of the initial part of the curve is the effective stiffness of the interface, K_{eff} , and the area under the curve is the critical strain energy release rate, \mathcal{G}_{crit} [28, 29, 31].

The penalty cohesive zone finite element approach can be implemented to calculate approximate values for the parameters of the cohesive elements, such as the effective stiffness and the strength, using the critical strain energy release rate [29]. This method is useful because it helps determine the cohesive zone parameters. Using the linear relationship shown in Figure 2-6 and an effective thickness of unity, approximations of the strength and effective stiffness of the interface are provided by Equations (2-32) and Equation (2-33) [29].

$$\sigma_o = \frac{2G_{crit}}{\delta_f} \quad (2-32)$$

$$K_{eff} = \frac{\sigma_o}{\delta_o} \quad (2-33)$$

These approximations are useful for initial modeling and can then be adjusted by comparing the numerical results to the experimental results and the analytical model.

For the second approach, the methodology for determining the parameters of the cohesive elements accounted for the size of the element and the length of the cohesive zone [31]. These factors need to be accounted for to prevent the cohesive elements from affecting the global compliance of the model prior to debonding and to allow for an accurate representation of the tractions in the cohesive zone [31]. The cohesive zone is the area from the crack tip to the point at which the maximum traction occurs in which the tractions and separations governing the adhesion occur [31]. To ensure there are enough elements in the cohesive zone, the cohesive zone length needed to be determined and compared to the cohesive element length. The cohesive zone length, ℓ_{CZM} , was predicted by Dugdale, Barenblatt, Hui et al., Falk et al., Hillerborg, and Rice to be dependent on the elastic modulus and thickness of the adjacent layer, E and t , and to have the form of Equation (2-34) [31].

$$\ell_{czm} = M \frac{E_s G_{crit}}{t} \quad (2-34)$$

The coefficient M depends on the model applied [31]. The number of elements along the cohesive zone length must be great enough to allow for accurate representation of the traction ahead of the crack tip [31]. The number of elements necessary for an accurate representation is not well established and varies from one author to another [31].

The strength of the interface can be determined by a desired ratio of cohesive zone length to element length by Equation (2-35) [31].

$$\sigma_o = \sqrt{\frac{9\pi E_s G_c}{32\ell_{czm}}} \quad (2-35)$$

It was determined that the effective elastic properties of the entire system were not affected by the cohesive elements if the interface stiffness was much higher than the young's modulus of the adjacent layer such that Equation (2-36) applies [31].

$$K_{eff} = \psi \frac{E_s}{t} \quad (2-36)$$

The parameter ψ needs to be much greater than unity to prevent the cohesive elements from affected the global compliance [31]. The value of fifty was suggested for ψ to reduce the effect of the interface on the compliance of the system to less than two percent, but it was also noted that too large of an interface stiffness can result in numerical problems [31].

Manual Crack Growth

Not only can the finite element method be used to model the interface and predict behavior, but it can be used to validate the analytical model. This can be done using CZM as well as comparing the analytical solution with a numerical model in which the crack length is increased manually. This method is similar to the experimental method performed by Lefebvre in which the debond length was increased manually and the strain in the adherends was compared to that predicted by the analytical model [20]. This method allows for more control in validating the analytical model but involves a more meticulous process.

Summary

The work presented here focuses on the adhesion between two solvated S-IPN silicone hydrogels and a COP substrate. In the process of characterizing the adhesion of the systems of interest, an understanding of the methods, theory, and principles applied are of importance. This includes the theory of viscoelasticity, TTSP principle, wedge test and corresponding analytical models, and numerical modeling methods for interfacial fracture. An understanding of these principles and methods provides a strong foundation for understanding the experimental methods applied, the analytical model derived, and the numerical model built in order to characterize the adhesion of the systems of interest.

Chapter 3: Experimental Methods

Introduction

This chapter describes the experimental methods applied to the bonded hydrogel and substrate systems of interest. This includes the sample preparation, the testing procedure, and the data collection. In order to investigate the effects of rate and temperature on the systems and apply time-temperature superposition (TTSP), the experimental method included a small temperature control unit to perform tests over a range of discrete temperatures. The effect of the length of time between curing and testing on the behavior of the specimens was investigated through samples tested at different times after curing. The amount of solvent loss and the possible effects was investigated through the observation of the specimen mass and thickness with increasing time after curing. In addition, the effect of the ratio of the adherends to the hydrogel thickness, and thus the confinement of the hydrogel, on the behavior of the specimens was investigated by comparing wedge test samples of different adherend or interlayer thicknesses. Lastly, testing was performed on the adherend material, Substrate X, in order to confirm the modulus used for this material in the analysis. The results of these experimental methods are presented, analyzed, and discussed in Chapter 5.

Sample Preparation

Each wedge test sample consisted of two rectangular substrates adhered to each other by a hydrogel interlayer that extended across the entire width but not to each end of the sample, as shown in Figure 3-1.

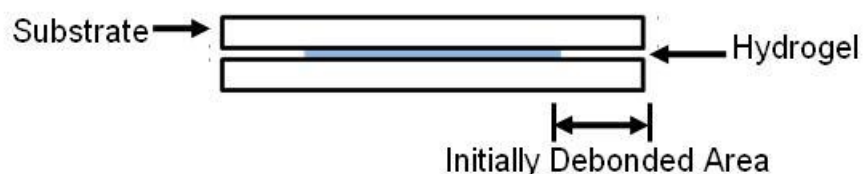


Figure 3-1: Wedge Test Specimen

Prior to making the samples, the thicknesses of the rectangular cyclo-olefin polymer (COP) substrates were measured using a Mitutoyo® digital indicator (Model ID-H530E), as shown in Figure 3-2, which reports an accuracy of 0.0015mm.



Figure 3-2: Measuring Thickness of Adherend using Mitutoyo® Digital Indicator

After measuring the thickness of each adherend, they were rinsed in reverse osmosis water (RO water) to remove any debris that would cause flaws in the final specimen and dried with a lint free cloth. The adherends were shipped and stored such that they would not be contaminated. Although the adherends had some debris on the surface that needed to be removed, they were not contaminated in such a way that a more involved cleaning process would be necessary. Polycarbonate sheets (thickness of 0.12 ± 0.01 mm) were used to create spacers to control the thickness of the hydrogel interlayer and to allow for an area at each end of the sample in which the hydrogel is not present, as shown in Figure 3-1. A square strip of the polycarbonate was taped to each end of one of the two substrates with tape (Scotch Brand Tape, Core series 2-1300, 3M), shown in Figure 3-3 and Figure 3-7, such that the polycarbonate strips were on the side of the adherend where the hydrogel would be applied and the tape on the opposite side.

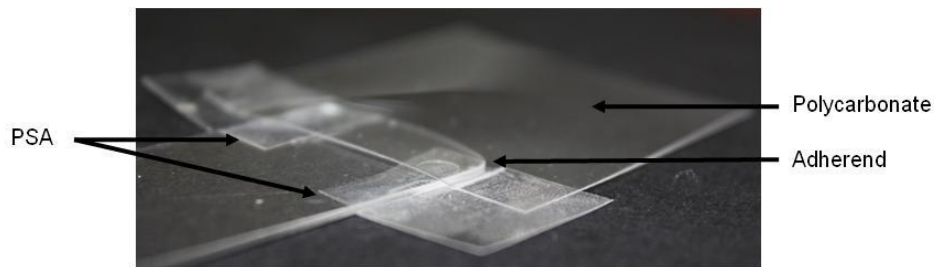


Figure 3-3: Adherend with Polycarbonate Spacer attached by PSA

Both substrates for the wedge specimen were set in the curing chamber, which is the acrylic glove box shown in Figure 3-4. The curing chamber was filled with nitrogen with a minimum purity level of 98% at a rate of 10 CFH (cubic foot per hour) for a minimum of eight hours prior to curing. This process purged the chamber of oxygen, which could adversely affect the

specimens since the monomer needs an oxygen-free environment in order to properly cure into a hydrogel.

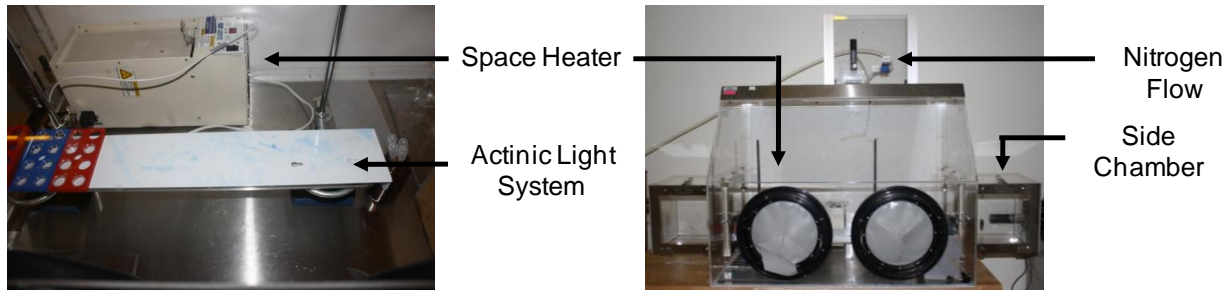


Figure 3-4: Curing Chamber

Approximately two hours before curing, the nitrogen flow was increased to 25 CFH and a space heater within the chamber was turned on and set for 65°C. This was done in order to bring the nitrogen level and temperature of the environment to that necessary for proper curing. Before working with the monomers, all natural light was blocked from the room, the overhead lighting was turned off, and a yellow fluorescent lighting with longer wavelengths was used to light the work area. The change of lighting was to prevent the monomer from prematurely curing as could happen if exposed to the lower wavelengths of natural or incandescent lighting. The monomer was placed in the vacuum chamber shown in Figure 3-5 that was attached to the vacuum pump shown in Figure 3-6. The monomer was left in the vacuum at a gage pressure of approximately -85kPa (-635 mmHg) for 30 minutes.



Figure 3-5: Vacuum Chamber



Figure 3-6: Vacuum Pump

After the monomer was vacuumed for 30 minutes, nitrogen was leaked into the vacuum chamber until the pressure within the chamber reached that of the atmosphere. The monomer was removed from the chamber and immediately placed into the curing chamber with the substrates for 30 minutes. The materials underwent this process of remaining in the heated nitrogen environment and/or being vacuumed prior to curing to flush out oxygen from the substrates and monomer. Oxygen in the materials or in the curing chamber can affect the results by interfering with the curing process. There were large amounts of variability in early testing in which the

oxygen was not properly purged. This variation was greatly reduced after implementing the process to flush out the oxygen.

To begin the process of curing a sample, a transfer pipette was used to place a small volume of the monomer on the bottom substrate to which the polycarbonate spacers were attached, as shown in Figure 3-7.

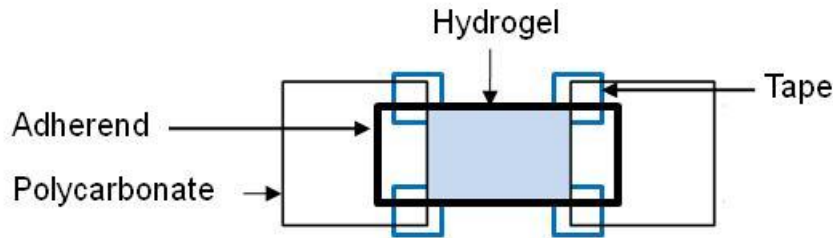


Figure 3-7 : Bottom Substrate with Polycarbonate Spacer and Monomer

The other substrate, without polycarbonate spacers attached, was gently placed on top such that no air bubbles formed in the monomer. After the monomer spread to fill the area between the two substrates, the specimen was placed under a actinic lights and exposed to an intensity of $0.5mW/m^2$ in order for the monomer to cure into a hydrogel and adhere to the substrates. After 30 minutes under the actinic lights, curing was complete and the specimen was removed from under the lights. The PSA tape was removed along with any residual hydrogel that may be on the outside of the specimen. The specimen was directly transferred to a small side chamber attached to the larger curing chamber. This smaller chamber contained nitrogen but was at room temperature. The sample remained in this small chamber for approximately thirty minutes.

Upon removal, the bonded sample thickness was measured along the width and length for later analysis in the same manner that the adherends were measured. The total average thickness of the two adherends was subtracted from the total average thickness of the bonded specimen. Although the method of using the polycarbonate spacers worked fairly well for controlling the thickness, there was still some variation in thickness throughout and between samples due to the polycarbonate spacers bending and the hydrogel flowing underneath.

The variance of the measurements of the total thickness of given sample was assumed to equal the variance of the hydrogel interlayer and applied to find the dispersion over the mean value of the hydrogel interlayer thickness. The dispersion over the mean of the hydrogel interlayer thickness of a given sample tended to be 18% to 20% for all samples and ranged from 6% to 41% for Hydrogel A samples and ranged from 18% to 87% for Hydrogel B samples. This is a high amount of dispersion and could be reduced by further refining the specimen preparation process, but this was not achieved in the duration of the project. However, when the thickness in a sample varied along the length or width, this was noted to insure that the hydrogel thickness in the area of crack growth was used in the calculations. This could be done since the final crack area in samples covered a small portion of the completed specimen.

After the specimen was measured, each polycarbonate spacer was removed to leave an area in which no hydrogel was present at each end as shown in Figure 3-1. The sample was then ready to be tested.

Wedge Test Procedure

Temperature Control

In order to control the temperature of the wedge specimens, each bonded specimen was set on the flat surface on top of an aluminum liquid heat exchanger block attached to a refrigerated circulating water bath with a temperature range of -20°C to 150°C , as shown in Figure 3-8.

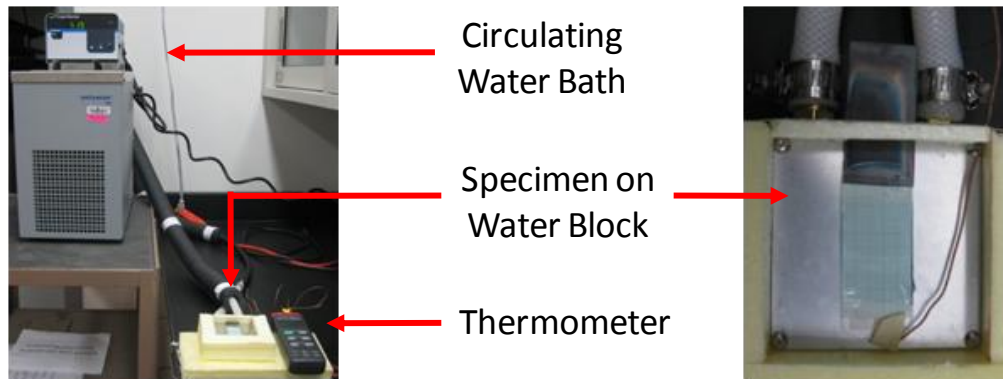


Figure 3-8: Small Scale Temperature Controller

The temperature for the water bath was set in order to bring the temperature of the specimen to that desired, spanning a range of interest of -5°C to 75°C . To establish a relationship between the temperature of the specimen and the water bath, a specimen was cured with a thermocouple in the hydrogel interlayer, as shown in Figure 3-9, and the temperature of this specimen was recorded for different water bath temperatures.

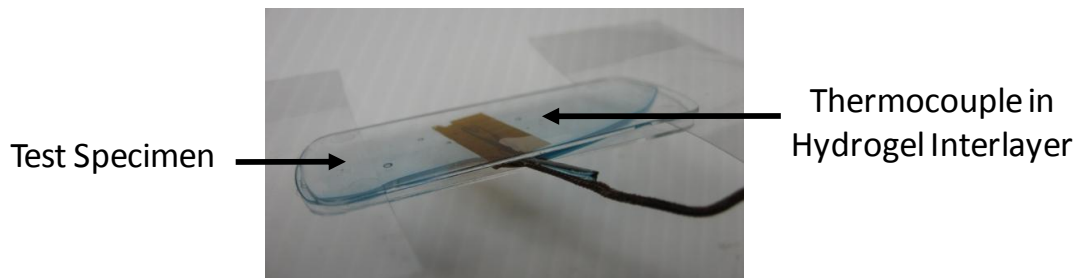


Figure 3-9: Thermocouple Cured in Hydrogel Interlayer

The sample with a thermocouple cured within the interlayer was set on the water block with the water bath set to a specific temperature, and the temperature of the specimen was recorded at 5, 10, and 15 minutes after being set on the block. A least-squares fitting was applied and a linear

fit was established for the results above room temperature, Equation (3-1), and for the results below room temperature, Equation (3-2).

$$T_{Bath} > T_{room} : \quad T_{specimen} = 0.94T_{Bath} + 1.68 \quad (3-1)$$

$$T_{Bath} < T_{room} : \quad T_{specimen} = 0.76T_{Bath} + 4.27 \quad (3-2)$$

The average of the three recorded specimen temperatures for each prescribed water bath temperature is compared to the respective fit in Figure 3-10.

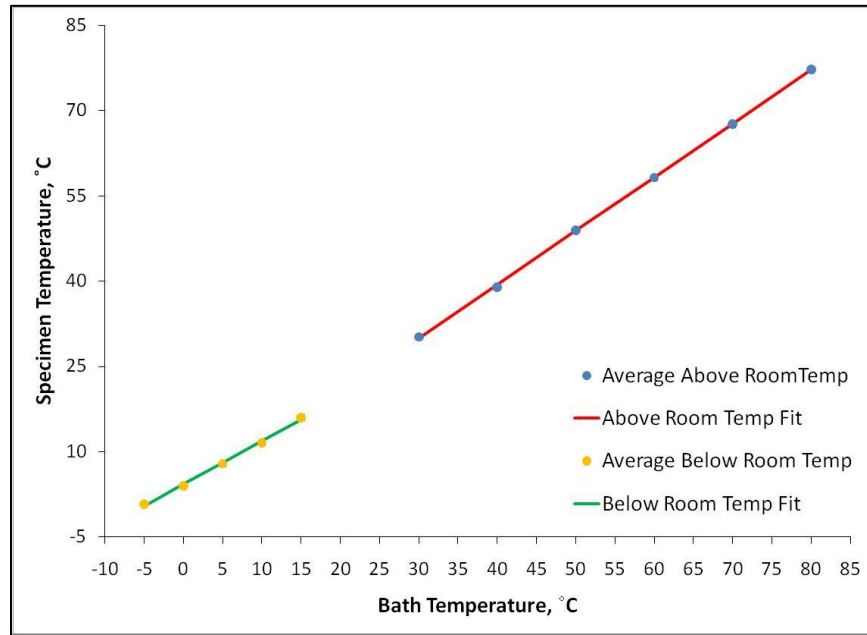


Figure 3-10: Sample Temperature versus Bath Temperature

The temperature range of 15°C to 30°C was not investigated because all samples tested within this range were tested at room temperature without the use of temperature control. Controlling the temperature near room temperature is difficult due to heating or cooling the water by only a small amount. For the samples tested at room temperature, the temperature of the atmosphere was recorded as the temperature of the specimen. Two different temperature fits were performed since the temperatures below room temperature were reached by refrigeration and those above room temperature by heating. During large scale testing, a specimen was placed on the water block and the water bath was set to a temperature above or below room temperature. Equations (3-1) and (3-2) were applied to the recorded water bath temperature to determine the temperature of the specimen during crack propagation. This temperature was used in the analysis to apply TTSP.

Wedge Testing

The Boeing wedge test, described in both ASTM 3762 and ISO 10354, is a fairly simple and useful method implemented to investigate mode I fracture durability [10, 11]. An adaption of the wedge test was applied to measure the adhesion between the hydrogel systems and the substrate of interest. The crack length over time was collected and used to establish a relationship between the crack propagation rates and the applied SERR. The only equipment necessary for the wedge test is the wedge specimen and a wedge to initiate the test. Other equipment was used in order to perform the wedge test at different temperatures and to record images of the crack growth during the wedge test. A wedge test specimen consisted of two adherends that were bonded to each other with an area at each end of the specimen in which no hydrogel was present. The test was initiated by inserting a wedge between the two adherends in one of the areas without hydrogel present. The wedge stayed in place for the remainder of the test and was not driven in further. The wedge insertion typically initiated debonding at one of the two hydrogel/substrate interfaces that increased in length with time. The rate at which the crack grew was very high at the initiation of the test and decreased over time until crack growth appeared to halt. Images of the wedge specimen were taken over time and these were used to record the crack length at discrete times throughout the test. The crack length was defined as the distance between the shoulder of the wedge in contact with the substrate and the crack front, as shown in Figure 3-11, Figure 3-12, and Figure 3-13.

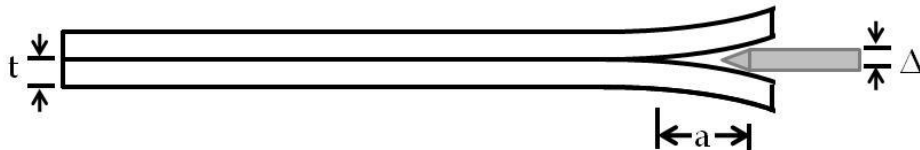


Figure 3-11: Schematic of the Wedge Test

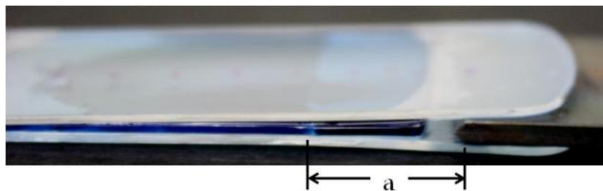


Figure 3-12: Side View of the Wedge Test

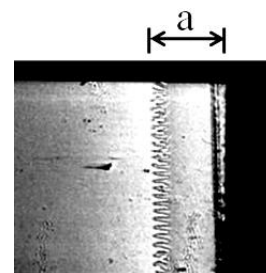


Figure 3-13: Image of Definition of Debond Length

Images of the test were taken and recorded with either the Phrotron® Fastcam APX-RX high speed camera with a 105mm lens or with a digital camera. The digital camera was used to record images over a period of an hour to a week. These images provided much useful data, but they did not capture the very short crack lengths during the initial portion of the crack growth when the crack propagation rate was the highest. For this reason, the high speed camera was utilized in order to take images at sixty frames per second for the first two minutes of testing.

Throughout most of the testing, the length of the crack was determined using graph paper placed above or below the specimen. As the crack grew, the length was measured with the graph paper as reference. However, this method was limiting in the increments in which the crack length could be measured. In later testing, this method was changed. Rather, a ruler was placed in the image so the pixels for a given length could be determined. This information was used to translate the number of pixels from the shoulder of the wedge to the crack tip into a length in millimeters. This method allowed for reading smaller changes in length and was especially useful for the high speed camera data, in which very small changes in length were captured between frames. The raw data, the crack lengths at discrete times, is presented in Chapter 5 for each hydrogel system.

Investigating Aging of Samples

The effect of the amount of time between curing and testing was investigated in more than one way. The different methods addressed the effects time after cure could have on the resulting SERR values, the behavior of the specimens during testing, the mass and thickness of the specimens, and the behavior of the specimens in which no wedge was inserted. The investigation of aging was focused on Hydrogel B due to the higher amount of scatter in Hydrogel B results and due to the greater number of issues with Hydrogel B in the application of these material systems.

One method for investigating the effects of time after cure involved taking a set of samples in which all the samples were cured at the same time and inserting the wedge to initiate crack growth at different amounts of time after curing. One of these sets remained in the 65°C nitrogen environment after curing. Once time to perform the wedge test on a given sample, the specimen was transferred from the curing chamber into an air environment at room temperature. The thickness of the sample was measured and recorded and the sample was immediately tested. Some sets of samples were removed from the curing chamber immediately after they were finished curing and the thickness of each samples was measured at room temperature. After the thicknesses were measured and recorded, the samples were placed on the water block with the water bath set to 0°C. Each of these samples remained on the block until after the wedge test was performed.

The second method for investigating the effects of time after cure consisted of tracking the mass of the samples after curing them. The purpose of tracking the mass was to investigate solvent loss and to correlate this to the results from the tests in which each wedge test was performed at a different lengths of time after cure. After the adherends for a specimen were prepared with the polycarbonate spacers, their mass was measured on an enclosed analytical balance and recorded. After taking three measurements of the adherends' mass, a wedge specimen was made by bonding the adherends with the hydrogel. After the sample was cured, the specimen was placed in the balance, as shown in Figure 3-14, and the mass was measured and recorded over time.



Figure 3-14: Sample on Enclosed Scale

To reduce noise, the sample remained in the balance until no more mass recordings were to be taken. Each of these recordings consisted of three readings so any noise in the readings could be considered.

The third method for investigating the effects of time after cure involved tracking the thickness of the samples over time. A change in thickness with time could be compared to the change in mass and the change in wedge test results over time. If a significant change in the thickness occurred over time, this would need to be considered in the analysis of the wedge tests results. Prior to making each sample, the thickness of each of the two adherends was measured in nine locations. After curing, the thickness was measured in these same locations repeatedly over time. Measuring the sample in multiple locations for a given sample and in the same locations between samples reduced error due to thickness variation across the sample.

The last method for investigating the effects of time after cure involved observing the appearance of untested specimens over time. The appearances of cured specimens were observed such as a change in color in the hydrogel or debonding at the edges.

Investigating Interlayer Confinement

Once a wedge was inserted, the resulting crack front often formed an undulating pattern as shown in Figure 3-15 [37].

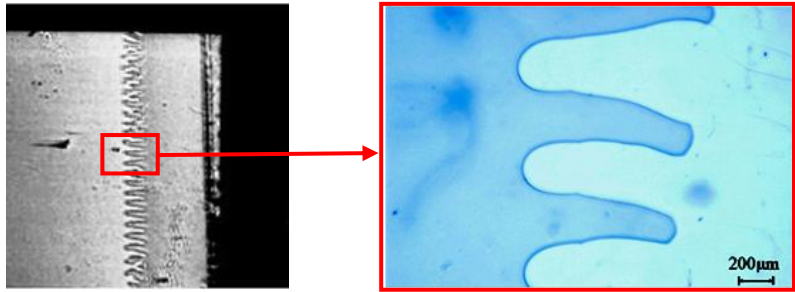


Figure 3-15: Undulating Crack Front during the Wedge Test

This pattern depends on the confinement of the hydrogel interlayer. As the confinement increases, the stress concentrated at the crack front increases and is relieved by the crack extending forward to form an undulating pattern. This concentrated stress is not accounted for in the analytical model and its effect on the behavior of the system is not entirely known. This pattern has been characterized by a confinement parameter, Equation (3-3), that can determine the extent of the confinement and whether the undulating pattern will be present [37].

$$\alpha = \left(\frac{D}{G_a h^3} \right)^{1/3} \quad (3-3)$$

The confinement parameter is related to the ratio of the adherend to the interlayer thickness and the ratio of the adherend to the hydrogel modulus. Since there is control of the thickness of the hydrogel interlayer and not the moduli of the materials, the effect of the adherend to hydrogel thickness ratio on the confinement was of greater interest. As the adherend to hydrogel thickness ratio increases, the confinement of the interlayer increases. For the research presented, tests were performed in order to show that the confinement, and thus the undulating crack growth, is based on the ratio of the adherend to the interlayer thickness and not solely the interlayer thickness. This was done by acquiring Substrate X adherends that were approximately 2.0mm thick and curing specimens in which the interlayer was approximately equal to the thinner Substrate X adherends used in the majority of the wedge testing.

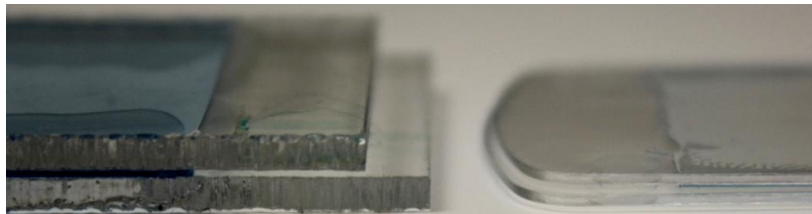


Figure 3-16: Comparison of Thick to Regular Wedge Test Specimen

The thick adherends allowed for high confinement of an interlayer with a thickness that was large compared to the interlayer thickness in the samples tested to characterize the system. To investigate possible effects of the confinement on the SERR values, specimens of high and low

confinement (undulating and straight crack fronts, respectively) were tested and the results were compared.

Investigating Adherend Parameters

Material properties for the materials used in the testing were needed for analyzing the results. Each material parameter was measured in another study, provided by the manufacturer, assumed based on similar materials, or measured experimentally. The shear modulus of each hydrogel system was determined from uniaxial tensile testing by applying an approximation for small to moderate stress-strain behavior for elastomeric materials defined by Equation (3-4) [4].

$$G_a = \frac{\sigma}{\lambda - \lambda^{-2}} \quad (3-4)$$

The extension ratio, $\lambda = 1 + \varepsilon$, and strain, σ , were collected during uniaxial tensile testing performed over a range of temperature and loading rates. The shear moduli values for Hydrogel A are presented in Table 3-1[4].

Table 3-1: Shear Moduli for Hydrogel A with Rate and Temperature [4]

Temperature, °C	Shear Modulus, <i>kPa</i>			
	10 <i>mm/s</i>	1 <i>mm/s</i>	0.1 <i>mm/s</i>	Average over all Rates
-5	1767±58	1099±73	755±11	1207±514
0	849±67	489±34	291±14	543±283
15	392±22	260±17	199±8	284±99
20	272±15	199±5	167±6	213±54
30	229±5	181±4	167±11	192±33
45	192±3	168±3	167±3	176±14
60	186±6	187±5	172±11	182±8
Average over all Temperatures	555±582	369±341	274±217	

The shear modulus is dependent on the rate and temperature and so these factors needed to be considered when using the shear modulus of Hydrogel A in the analysis. The shear modulus ranges from 1767*kPa* at fastest rate and lowest temperature to 167*kPa* at the slowest rate and multiple higher temperatures. However, it does appear that the shear modulus is more affected by the temperature than the rate. The information in Table 3-1 was used in order to estimate the shear modulus at a given testing temperature. Due to the sudden load at the beginning of the test with the insertion of the wedge and without any additional load applied through the test, the loading rate could be neglected. The slowest loading rate described in Table 3-1 was used to determine the shear modulus values for given testing temperatures. A greater emphasis was placed on the effects of temperature since this played a greater role in the behavior than the rate.

The shear moduli values for Hydrogel B obtained from uniaxial tensile testing at different rates and temperatures are presented in Table 3-2 [4].

Table 3-2: Shear Moduli for Hydrogel A and Hydrogel B with Rate and Temperature [4]

Temperature, °C	Shear Modulus, <i>kPa</i>			
	10 <i>mm/s</i>	1 <i>mm/s</i>	0.1 <i>mm/s</i>	Average over all Rates
-5	96±3	69±3	67±2	77±16
0	77±2	69±2	63±4	69±7
15	72±2	71±1	67±3	70±3
20	76±3	74±2	73±3	74±1
30	75±5	66±7	63±5	68±6
45	72±3	75±4	75±1	74±2
60	75±4	74±1	69±1	73±3
Average over all Temperatures	78±8	71±3	68±5	

The shear modulus of Hydrogel B was also more affected by temperature than rate. However, the shear modulus of Hydrogel B was overall less affected by temperature and rate than the shear modulus of the Hydrogel A. The average shear modulus for all temperatures and rates for Hydrogel B was $72\pm7\text{ kPa}$. Since the overall average has a standard deviation similar to the averages for given temperature and rate combinations in Table 3-2, this value was used for all testing temperatures and rates for Hydrogel B.

The flexural modulus, modulus of elasticity, and the glass transition temperature for Substrate X were provided by the manufacturer and presented Table 3-3.

Table 3-3: Selected Substrate X Properties Provided by the Manufacturer

Flexural Modulus, <i>MPa</i>	2100
Modulus of Elasticity in Tension, <i>MPa</i>	2100
Glass Transition Temperature, °C	100

The modulus of Substrate X was further investigated to compare with the value provided by the manufacturer and to see the effects that temperature may have on its behavior since the wedge test is performed over a range of temperatures. To find the elastic modulus of Substrate X, three-point bending was performed on a screw-driven testing machine, shown in Figure 3-17, and in a DMA, shown in Figure 3-18.



Figure 3-17: Three-Point Bend of Substrate X on Instron Testing Machine

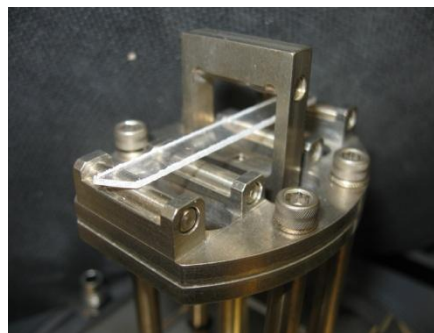


Figure 3-18: Three-Point Bend of Substrate X in DMA Testing Machine

The results from these three-point bend tests were analyzed in order to calculate the flexural modulus of the substrate which was assumed to be equal to the elastic modulus. The Poisson's ratio was not provided by the manufacturer for Substrate X. However, the manufacturer did provide a Poisson's ratio of 0.41 for another cyclo-olefin polymer (COP) similar to Substrate X. MatWeb, an online database of material properties, reports a Poisson's ratio range of 0.37 to 0.41 for the COP materials in its database [38]. This further supports using a value of 0.41. However, no testing was performed to validate this value.

Summary

A variation of the wedge test was performed in order to characterize the adhesion between each hydrogel, Hydrogel A and Hydrogel B, and Substrate X. The testing was performed at various temperatures within a range of interest so that TTSP could be applied during the analysis. The experimental method, from sample preparation to temperature control, was developed throughout the course of this research. The methods presented are the final methods and those used to collect the results in Chapter 5. Changes were made to reduce variation between samples. Not only were possible sources of variation removed, but some were investigated as well. Side studies were performed to investigate the effects of time between curing and wedge insertion on the behavior of each system. These side studies shed light on reasons for variations and difficulties during the large scale testing. They also allowed for greater insight of the materials and possible attributes to the phenomena of bridging. In the analysis in Chapter 5, the parameters of the materials need to be known. The parameters for hydrogel were drawn from previous work performed on them. For Substrate X, testing was performed to check the elastic modulus provided by the manufacturer and to observe the influence of temperature on the modulus. All of the results for the methods described are presented in Chapter 5, along with the analysis that involves the analytical model derived in Chapter 4.

Chapter 4: Analytical Model for Characterizing Interfacial Fracture

Introduction

An analytical model was needed to take the crack length measurements collected from the experimental process described in Chapter 3 and find the corresponding applied strain energy release rate (SERR) values. The simple beam solution (SBT) is often applied to the wedge test but does not account for the effects that a finite thickness interlayer has on the system. For this reason, an appropriate analytical model needed to be derived for the configuration shown in Figure 4-1,



Figure 4-1: Wedge Test Geometry and Dimensions

where h is the thickness of the interlayer, Δ is the wedge thickness, a is the crack length, and t is the thickness of each adherend. The analytical model was formulated by characterizing the deflection of the adherend and the deflections that occur within the interlayer. These deflections were then used to find the applied strain energy release rate. The methods applied to develop the analytical model have a strong basis in the work performed by Komatsu et al. [19], Ghatak et al. [21] and Dillard [23].

Characterization of the Deflection of the Adherends

Coordinate System

The deflection of each adherend was determined with the assumption that the test was symmetrical. The coordinate system for developing the analytical model, shown in Figure 4-2, was established with the origin placed at the far edge of the debond. The origin remained at the crack tip as the crack grew.



Figure 4-2: Coordinate System for the Analytical Model for the Wedge Test

The bonded region was defined as $x < 0$ and the debonded region was defined as $x > 0$. Although the interlayer remained on one of the two adherends after debonding, as shown in Figure 4-1, the interlayer was not considered in determining the adherend stiffness in the debonded region for simplicity. This was a good assumption due to the low moduli considered for the interlayer. As a result, the parameters of the hydrogel interlayer were assumed to not affect the flexural rigidity of the adherend such that $D = Et^3/12(1 - \nu^2)$. This is an area in which more accuracy and complexity could be added to the model by including the interlayer in the definition of the flexural rigidity for one of the two adherends in the debonded region. For an interlayer with a greater stiffness, the interlayer would need to be considered in determining the stiffness of the adherend of which the interlayer remains bonded to in the debonded region.

Governing Equations

Each adherend was considered as a plate on an elastic foundation. Therefore, the classical differential equation describing a plate on an elastic foundation, presented by Equation (2-27), was applied to initially describe the deflection of each adherend, $W(x)$,

$$\frac{\partial^4 W}{\partial x^4} + 2 \frac{\partial^4 W}{\partial x^2 \partial y^2} + \frac{\partial^4 W}{\partial y^4} = \frac{p(x, y) - q(x, y)}{D} \quad (4-1)$$

where $p(x, y)$ is the distributed load and $q(x, y)$ is the restoring pressure from the foundation [39]. The behavior of the wedge test did not vary with width with the exception of the undulating crack front described in Chapter 3. This undulation was neglected and the solution was assumed independent of the width of the system. Despite the undulation, this assumption is valid since the amplitude and frequency of the undulating crack front do not vary with the width. The assumption that the solution was independent of the sample's width reduces the governing differential equation to Equation (4-2).

$$\frac{\partial^4 W}{\partial x^4} = \frac{p(x) - q(x)}{D} \quad (4-2)$$

The only load applied to the wedge test was that applied at the point of contact between the adherend and the wedge. Since no distributed load was applied, Equation (4-2) further reduces to Equation (4-3).

$$\frac{\partial^4 W}{\partial x^4} = -\frac{q(x)}{D} \quad (4-3)$$

Equation (4-3) is the general governing equation for the behavior of the adherends in both the bonded and debonded region. In the bonded region, the interlayer acts as an elastomeric foundation and applies a restoring pressure on the adherend. However, this does not occur in the debonded region. In the debonded region, the interlayer no longer reacts with the adherend such that $q(x) = 0$. The GDE for the debonded region became the GDE for simple beam theory as shown by Equation (4-4).

$$\frac{\partial^4 W}{\partial x^4} = 0 \quad (\text{debonded}) \quad (4-4)$$

For the bonded region, it was assumed that the restoring pressure was equal but opposite to the hydrostatic pressure within the interlayer such that $q(x) = -Q$. The GDE for the bonded region then became Equation (4-5).

$$\frac{\partial^4 W}{\partial x^4} = \frac{Q(x)}{D} \quad (\text{bonded}) \quad (4-5)$$

Once the governing equations for the debonded and bonded areas of the wedge test were established, the coordinate system and boundary conditions were needed in order to define the deflection of the adherends in the bonded and debonded regions.

Application of Boundary Conditions

The interlayer was assumed to be incompressible. This assumption allows for the solution to be applied to the wedge test configurations with an elastomeric interlayer, such as a hydrogel. The incompressibility of the interlayer is described by Equation (4-6) in which the sum of the strains in the interlayer in the thickness and length direction are zero where $u(x, z)$ and $w(x, z)$ are the deflections that occur within the interlayer in the x and z directions.

$$\frac{\partial u}{\partial x} + \frac{\partial w}{\partial z} = 0 \quad (4-6)$$

Applying the pressure method by Gent, the deflection in the thickness direction can be described by the volume change due to the deflection of both adherends, which is defined as the product of the shape factor of the cross section of the incompressible interlayer and the deflection of the two adherends over the thickness of the interlayer [23, 24, 40]. The spatial variations in the length direction of the interlayer are described by Equation (4-7).

$$\frac{\partial u}{\partial x} = \frac{4}{3} \left(\frac{2W(x)}{h} \right) \quad (4-7)$$

The change in the normal stress, σ_x , due to the spatial variations can be described by Equation (4-8),

$$\frac{\partial \sigma_x}{\partial x} = \frac{8G_a}{h^2} u \quad (4-8)$$

where G_a is the shear modulus of the interlayer [23]. Due to the interlayer being very thin, the normal stress can be assumed as approximately equal to the hydrostatic pressure, $\sigma_x = Q$. Differentiating Equation (4-7) and substituting into Equation (4-8) results in Equation (4-9).

$$\frac{\partial^2 Q}{\partial x^2} = \frac{64G_a}{3h^3} W(x) \quad (4-9)$$

The GDE of the adherend deflection in the bonded region, shown by Equation (4-10), is defined by substituting Equation (4-9) into the second derivative of Equation (4-5).

$$\frac{\partial^6 W}{\partial x^6} - \lambda^6 W(x) = 0 \quad \text{where} \quad \lambda^6 = \frac{64G_a}{3Dh^3} \quad (\text{bonded}) \quad (4-10)$$

The general solutions for the bonded and debonded regions described by Equation (4-11) and Equation (4-12) [23].

$$x < 0: \quad W(x) = A_1 e^{\lambda x} + A_2 e^{-\lambda x} + e^{\frac{\lambda}{2}x} \left(A_3 \cos \frac{\sqrt{3}}{2} \lambda x + A_4 \sin \frac{\sqrt{3}}{2} \lambda x \right) + e^{-\frac{\lambda}{2}x} \left(A_5 \cos \frac{\sqrt{3}}{2} \lambda x + A_6 \sin \frac{\sqrt{3}}{2} \lambda x \right) \quad (4-11)$$

$$x > 0: \quad W(x) = C_1 x^3 + C_2 x^2 + C_3 x + C_4 \quad (4-12)$$

Ten boundary conditions were then needed to solve for the coefficients in Equations (4-11) and (4-12). First, the wedge was assumed to be a simple support at the point of contact with the adherend, resulting in both a known displacement and no moment acting at the point of loading, as shown by Equation (4-13) [21].

$$W(a) = \frac{\delta}{2} \quad \frac{\partial^2 W}{\partial x^2}(a) = 0 \quad (4-13)$$

The deflection of the adherend due to the applied displacement at $x = a$ was assumed to decay far from the point of loading, as shown in Equation (4-14), which removed the dependency of the solution on the bonded length of the specimen [21, 23].

$$W(x)\Big|_{x \rightarrow -\infty} = 0 \quad \frac{\partial W(x)}{\partial x}\Big|_{x \rightarrow -\infty} = 0 \quad \frac{\partial^2 W(x)}{\partial x^2}\Big|_{x \rightarrow -\infty} = 0 \quad (4-14)$$

As with the DCB-FTAL and confined film models, continuity of the deflection of the adherend was assumed at the crack tip. Continuity was established by equating the deflection, slope, bending moment, and shearing force of the bonded and debonded regions at the crack tip, as shown by Equation (4-15) [21, 23].

$$W(0-) = W(0+) \quad \frac{\partial W(0-)}{\partial x} = \frac{\partial W(0+)}{\partial x} \quad \frac{\partial^2 W(0-)}{\partial x^2} = \frac{\partial^2 W(0+)}{\partial x^2} \quad \frac{\partial^3 W(0-)}{\partial x^3} = \frac{\partial^3 W(0+)}{\partial x^3} \quad (4-15)$$

The normal stress in the interlayer, σ_x , becomes maximally tensile near the edge of the debond. This causes the change in the normal stress with respect to x is assumed to be zero at the edge of the debond. Since the normal stress is approximately equal to the hydrostatic pressure in the thin interlayer, the change in the pressure gradient at the edge of the debond is also assumed to be equal to zero such that Equation (4-16) applies [21].

$$\frac{\partial Q}{\partial x}(0,0) = 0 \quad (4-16)$$

This assumption expressed by Equation (4-16) was made in the derivations performed by Ghatak for the confined film model [21]. The application of the boundary conditions in Equations (4-13) to (4-16) to the general solutions in Equations (4-11) and (4-12) lead to the deflection of the adherends and the deflections within the interlayer in the bonded region.

Solution

The coefficients for Equations (4-11) and (4-12) are described by Equations (4-17) to (4-19).

$$A_1 = 3(a\lambda)\phi \quad A_3 = 3(2+a\lambda)\phi \quad A_4 = \sqrt{3}(2+3a\lambda)\phi \quad (4-17)$$

$$C_1 = -\lambda^3\phi \quad C_2 = 3a\lambda^3\phi \quad C_3 = 3\lambda(2+3a\lambda)\phi \quad C_4 = 6(1+a\lambda)\phi \quad (4-18)$$

$$\phi = \frac{(\Delta - h)}{2(6 + a\lambda(12 + a\lambda(9 + 2a\lambda)))} \quad (4-19)$$

The deflection of the adherend in the bonded and debonded region can then be expressed by Equations (4-20) and (4-21), respectively.

$$x < 0: \quad W(x) = \phi \left[3ae^{x\lambda} + e^{\frac{x\lambda}{2}} \left(3(2+a\lambda)\cos\left(\frac{\sqrt{3}}{2}x\lambda\right) + \sqrt{3}(2+3a\lambda)\sin\left(\frac{\sqrt{3}}{2}x\lambda\right) \right) \right] \quad (4-20)$$

$$x > 0: W(x) = \phi \left[6 + 6(x\lambda) - (x\lambda)^3 + 3(x\lambda)(1+x\lambda)(2+x\lambda) \right] \quad (4-21)$$

The deflection can also be described by the moment and shear force that occurs at the crack front, M_0 and F_0 defined in Figure 4-3, as shown by Equations (4-22) and (4-23).

$$x < 0: W(x) = \frac{e^{\frac{x\lambda}{2}}}{2\sqrt{3}Da\lambda^3\delta} \left[\sqrt{3} \left(ae^{\frac{x\lambda}{2}} \lambda + (2+a\lambda) \cos\left(\frac{\sqrt{3}}{2}x\lambda\right) \right) M_0 - a(2+3a\lambda) \sin\left(\frac{\sqrt{3}}{2}x\lambda\right) F_0 \right] \quad (4-22)$$

$$x > 0: W(x) = -\frac{6+6x\lambda-(x\lambda)^3+3(a\lambda)(1+x\lambda)(2+x\lambda)}{6D\lambda^3} F_0 = \frac{6+6x\lambda-(x\lambda)^3+3(a\lambda)(1+x\lambda)(2+x\lambda)}{6D\lambda^3 a} M_0 \quad (4-23)$$

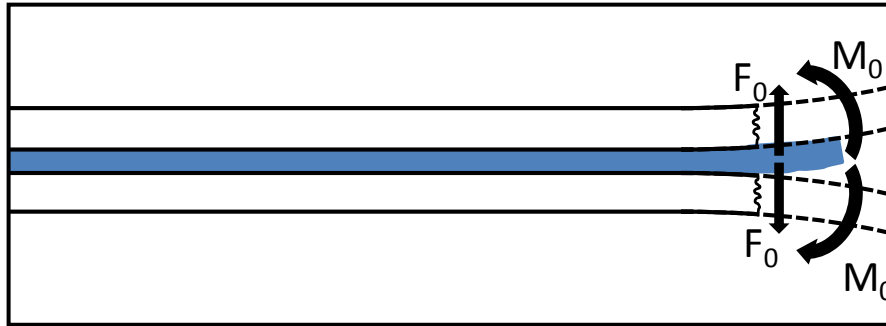


Figure 4-3: Moment, M_0 , and Shear Force, F_0 at the Crack Front

An example of the adherend deflection in the bonded region, expressed by Equation (4-20), is shown in Figure 4-4 for the parameters presented in Table 4-1 and various interlayer thicknesses.

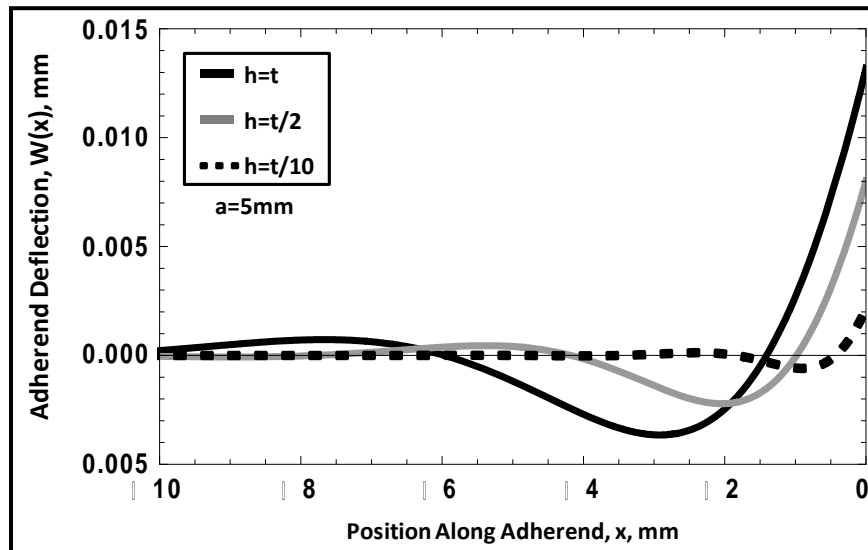


Figure 4-4: Deflection of Adherend along Bonded Length

Table 4-1: Parameters for Demonstration of Analytical Model

	Materials	Modulus (kPa)	Poisson's Ratio	Thickness (mm)	δ (mm)
Adherends	Substrate X	Elastic: $2.1E6$	0.410	$t = 0.7$	0.25
Interlayer	Hydrogel A	Shear: 168	0.5	h	

The deflection of the adherend decays faster as the ratio of the adherend to interlayer thickness increases. As the interlayer thickness decreases, its role decreases and the solution approaches the simple beam theory solution. A deflection of the adherend at the crack tip versus crack length for the parameters presented in Table 4-1 and various interlayer thicknesses is shown in Figure 4-5.

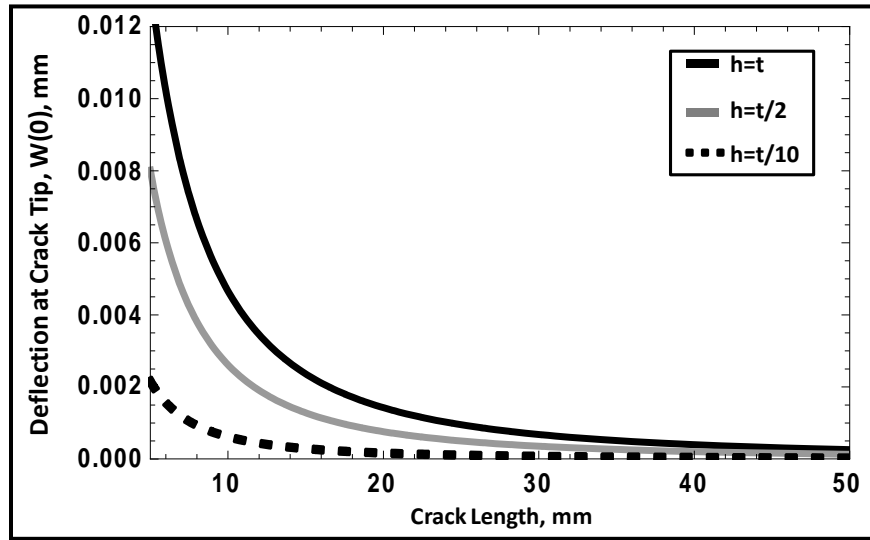


Figure 4-5: Deflection at the Crack Tip versus Crack Length

As the thickness of the interlayer increases, the deflection at the crack tip increases. There is more stretching of the interlayer at the crack tip but less bending of the adherend. For the SBT solution, deflection does not take place at the crack tip for all crack lengths. The deflection at the crack tip in the derived model results in a reduced reaction force at the point of loading, as shown in Figure 4-6 with the reaction force described by Equation (4-24).

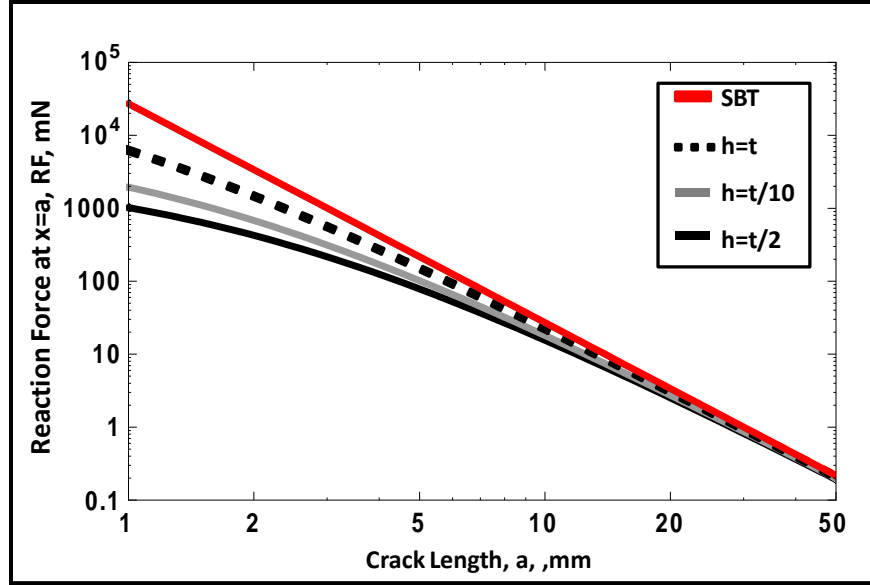


Figure 4-6: Reaction Force versus Crack Length for Different Crack Lengths and Interlayer Thicknesses

The reaction force at the point of loading is lower for short crack lengths for the adherend deflection expressed by Equation (4-21) than for the SBT deflection. It is this difference that leads to the compliance being underestimated by the SBT solution. In the application of fixed displacement, the SERR is overestimated when the compliance is underestimated.

Defining the Strain Energy Release Rate (SERR)

Once the deflection was established, it was applied to determine the SERR by evaluating the change in the compliance at the point of loading with increasing crack area. The change in the loading that occurred with the constant applied displacement and increasing crack area was determined and implemented to define the SERR. The force acting on each adherend at the point of loading, $P(x)$, was determined by Equation (4-24).

$$P(a) = -Db \left. \frac{\partial W^3(x)}{\partial x} \right|_{x=a} \quad (4-24)$$

The force acting on the point of loading was applied to the LEFM definition of the SERR as shown by Equation (4-25).

$$\mathcal{G} = -\frac{\delta}{2b} \frac{\partial P(a)}{\partial a} \quad (4-25)$$

Applying Equation (4-24) to each adherend in the system and applying Equation (4-25) resulted in the definition for the SERR provided by Equation (4-26).

$$G = \frac{9D\delta^2}{4a^4} \kappa(a\lambda) \quad (4-26)$$

where $\kappa(a\lambda)$ is the correction factor defined in Equation (4-27).

$$\kappa(a\lambda) = \frac{8(a\lambda)^4 + 12(a\lambda)^5 + 4(a\lambda)^6}{36 + 144(a\lambda) + 252(a\lambda)^2 + 240(a\lambda)^3 + 129(a\lambda)^4 + 36(a\lambda)^5 + 4(a\lambda)^6} \quad (4-27)$$

Comparison of Analytical Models

The analytical model is compared to the DCB-FTAL, DCSB, and confined film models for the Substrate X and Hydrogel A system in Figure 4-7. Plane strain was applied to all the models and the parameters utilized for the comparison are in Table 4-1.

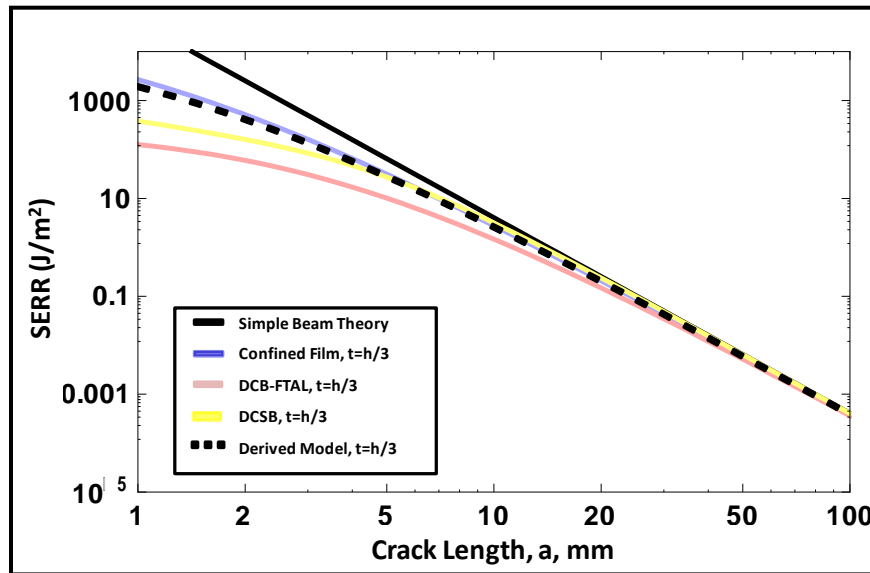


Figure 4-7: Comparison of Analytical Models over Large Range of Crack Lengths

The SERR values for the analytical model were less than that for the confined film. This is due to the increased mobility of the interlayer for the analytical model. The resulting SERR values remained higher than that for the DCSB and DCB-FTAL solutions, because the DCB-FTAL and DCSB models do not treat the adhesive as incompressible. The derived analytical model is an improvement over the confined film model due to the boundary conditions and assumptions being tailored to the wedge test geometry.

Summary

The derived analytical model is useful in that it can be applied for wedge tests in which there is an interlayer of finite thickness, as shown in Figure 4-1. The existing analytical models for such a geometry and loading are limited, because an interlayer of finite thickness adds complexity. There are improvements that can be made such as including the effect of the interlayer in the

debonded region and adjusting the coordinate system for asymmetrical cases. However, prior to these improvements, the model is an improvement over existing models for the geometry and loading of the wedge test with a finite thick elastomeric interlayer.

Chapter 5: Experimental and Analytical Results

Introduction

This chapter presents the results from applying the methods described in Chapter 3 and the model developed in Chapter 4. The analytical model was applied to the experimental results to establish a relationship between the crack propagation rate and the applied strain energy release rate (SERR) for each system. The process of building a master curve was stepped through for each hydrogel system. This provided insight into the adhesion of each system and the influences of both temperature and crack propagation rate.

In addition to the analysis of the wedge test results, qualitative and quantitative results from the investigation of the aging of samples are presented and discussed. The results from these tests bring insight to possible sources of variation in the wedge test results in addition into bringing greater insight to bridging and effects of solvent loss. Lastly, the results from the three-bend tests of Substrate X are reviewed.

Wedge Test Results

The images from the wedge test were used in order to measure the crack length at discrete times. The crack length measurements over time are shown in Figure 5-1 for the Hydrogel A and Substrate X system and in Figure 5-2 for the Hydrogel B and Substrate X system. Each data set represents samples tested at the prescribed temperature.

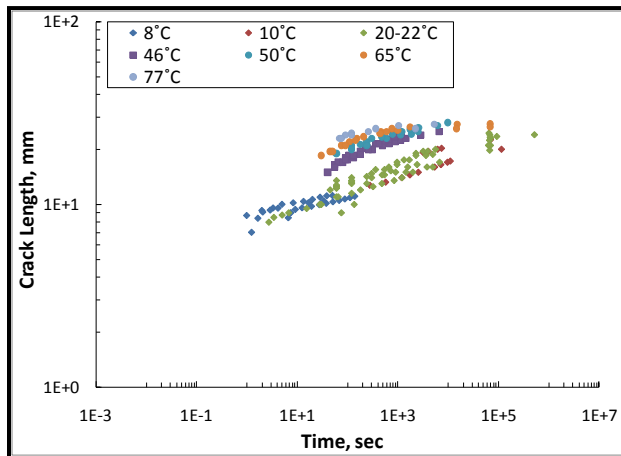


Figure 5-1: Crack Length versus Time for Hydrogel A and Substrate X

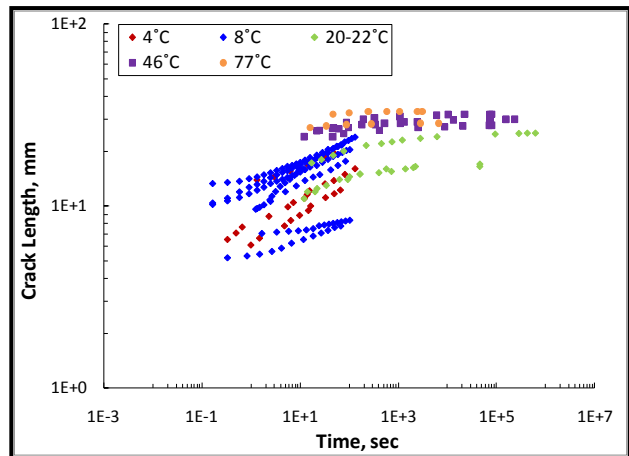


Figure 5-2: Crack Length versus Time for Hydrogel B and Substrate X

The test began at different points of crack growth for different samples. This caused the data sets in Figure 5-1 and Figure 5-2 to be for different time frames of crack growth. As a result, some data sets cover long crack length ranges and other data sets cover shorter crack length ranges

without a correlation to the time. This issue was resolved by observing crack propagation rates rather than time, as shown in Figure 5-3 and Figure 5-4.

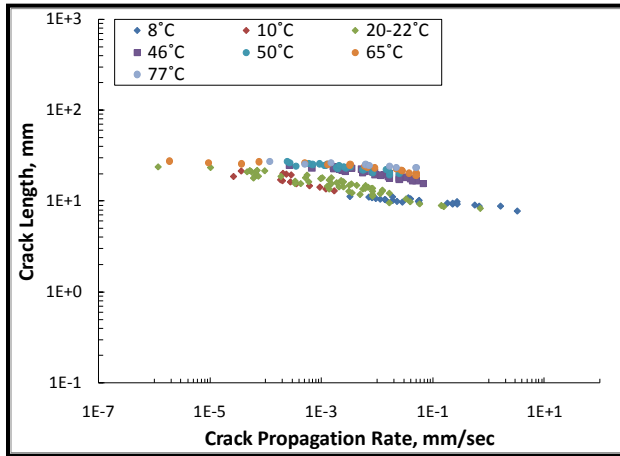


Figure 5-3: Crack Length versus Crack Propagation Rate for Hydrogel A and Substrate X

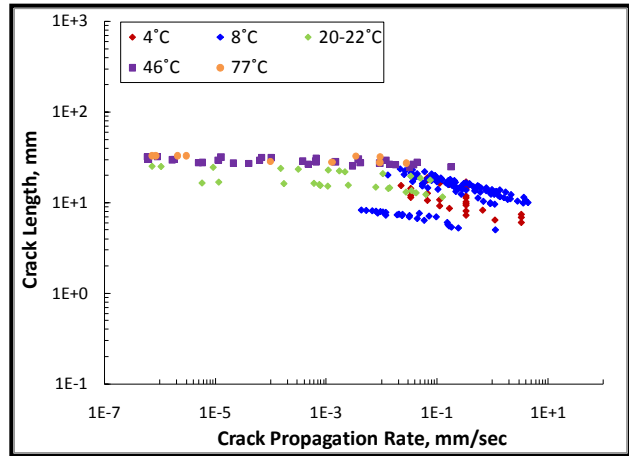


Figure 5-4: Crack Length versus Crack Propagation Rate for Hydrogel B and Substrate X

The sets covering the short crack lengths tend to be at higher crack propagation rates and the sets covering the long crack lengths tend to be at lower rates. By observing the crack length at crack propagation rates rather than time, the variation due to looking at different frames of time is removed. There remains variation due to differences between samples such as the thickness of the interlayer. By considering these differences in the analysis, much more of this variation is removed after the analysis is applied. For example, the analytical model considers the hydrogel interlayer thickness and removes variation between samples due to the different hydrogel interlayer thicknesses.

Application of Analytical Model

The analytical model derived in Chapter 4 was applied to the wedge test results for each system to interpret the experimental results into useful information on the adhesion of the system and to compare the interfacial fracture of each system to one another and the respective cohesive fracture of each hydrogel system.

Comparison of Applying Analytical and SBT Models

The results after application of the derived model and the simple beam theory model are shown in Figure 5-5 for Hydrogel A and Figure 5-6 for Hydrogel B. Each data set includes the results for data collected at all temperatures investigated.

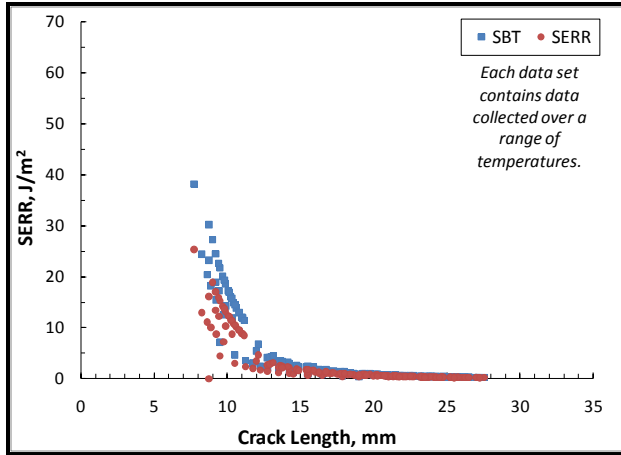


Figure 5-5: SERR versus Crack Length for Hydrogel A and Substrate X

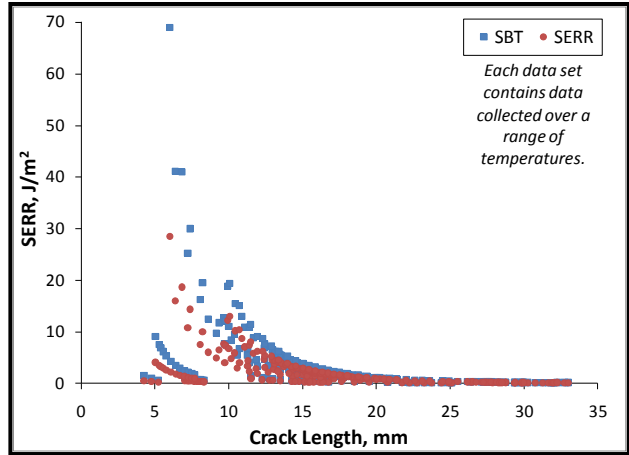


Figure 5-6: SERR versus Crack Length for Hydrogel B and Substrate X

Figures 5-7 and 5-8 show that the derived model provides lower values than the SBT model. The difference between the two solutions increases with decreasing crack length for both hydrogel systems. In general, the difference between the derived model and the simple beam theory solution appear greater for the Hydrogel B system than the Hydrogel A system.

Crack Rate versus SERR Prior to TTSP

The interfacial fracture is often characterized by the relationship between the crack propagation rate and the applied SERR. This relationship is presented for Hydrogel A in Figure 5-7 and Hydrogel B in Figure 5-8, prior to the application of TTSP.

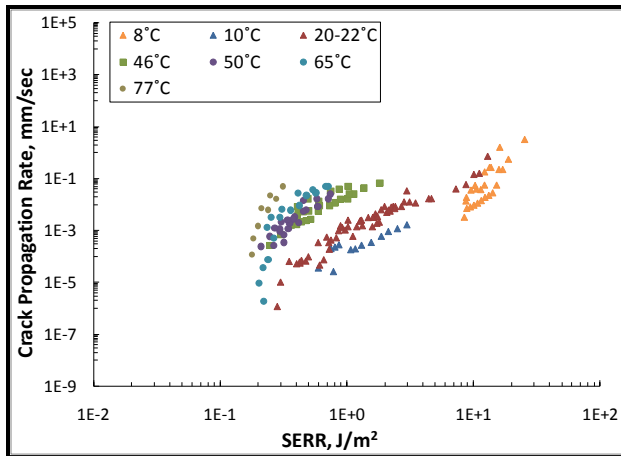


Figure 5-7: Crack Propagation Rate versus SERR Prior to Shifting for Hydrogel A and Substrate X

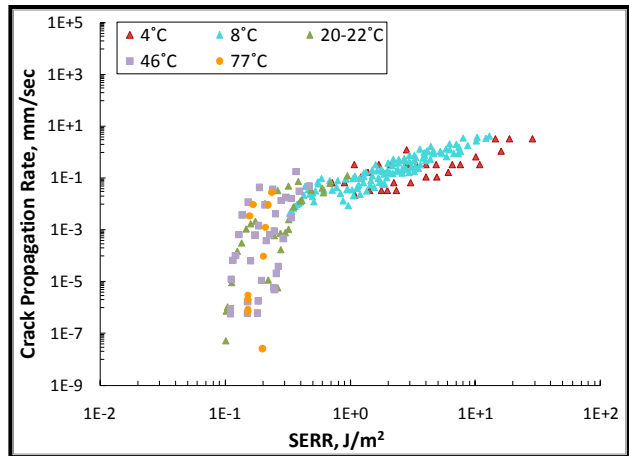


Figure 5-8: Crack Propagation Rate versus SERR Prior to Shifting for Hydrogel B and Substrate X

Each data set in Figure 5-7 and Figure 5-8 represents specimens tested at a given temperature. The temperature sets for Hydrogel A form an assortment of separate curves prior to applying TTSP. The results for Hydrogel B, however, tend to consolidate prior to applying TTSP.

Application of Time-Temperature Superposition

The curves in these plots were shifted into master curves by applying time-temperature superposition principle (TTSP). The Williams-Landel-Ferry (WLF) equation-based shift factor equation developed from the bulk behavior of the hydrogels, shown in Figure 5-9 [4], was applied. The coefficients of the WLF equation-based shift factor equation for Hydrogel A and Hydrogel B are presented in Table 5-1 for each hydrogel [4].

Table 5-1: WLF Equation Coefficients for the Bulk Behavior of Hydrogel A and Hydrogel B [4]

Hydrogel	C_1	C_2
A	5.95	119.60
B	4.57	142.20

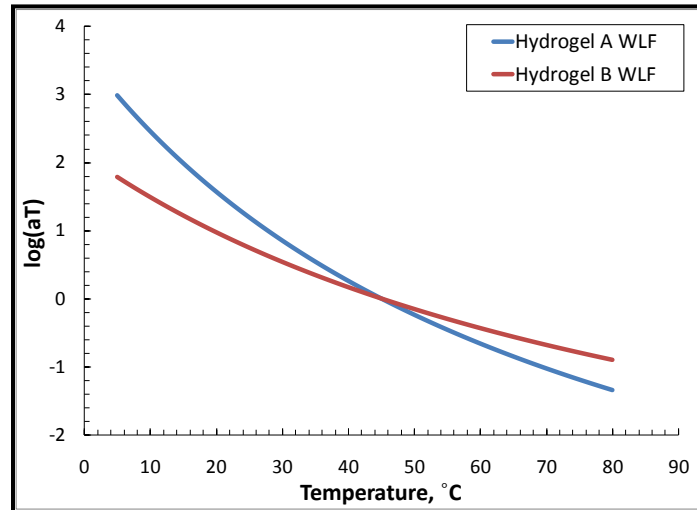


Figure 5-9: WLF equation-based Shift Factors for the Bulk Behavior of Hydrogel A and Hydrogel B [4]

The range of the WLF based shift factors for Hydrogel B cover a much smaller range than Hydrogel A for the same temperature range. This means that temperature plays a lesser role in the behavior of Hydrogel B than Hydrogel A for the range of temperatures investigated. The master curves resulting from the application of the shift factors in Figure 5-9 are shown in Figure 5-10 for Hydrogel A and Figure 5-11 for Hydrogel B.

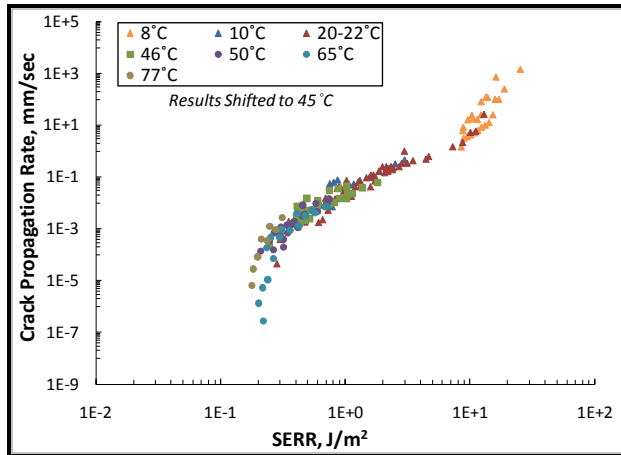


Figure 5-10: Crack Propagation Rate versus SERR Master curve for Hydrogel A and Substrate X at $T_{ref} = 45^{\circ}\text{C}$

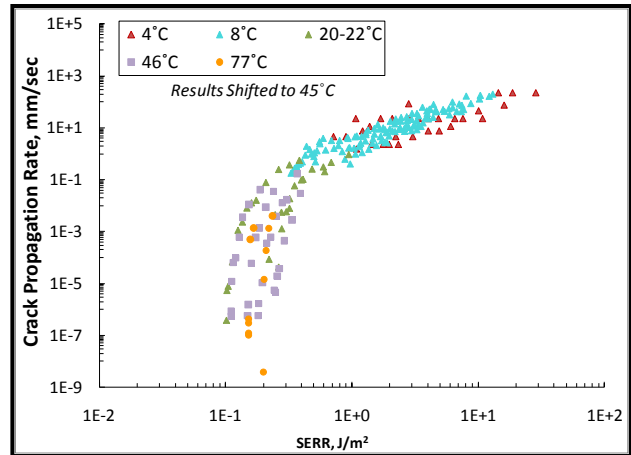


Figure 5-11: Crack Propagation Rate versus SERR Master curve for Hydrogel B and Substrate X at $T_{ref} = 45^{\circ}\text{C}$

For both systems, the WLF equation-based shift factors developed for the bulk behavior of the hydrogel appear to work well for shifting the rate-dependent fracture data. This implies that the viscoelastic characteristics of each hydrogel system play a large role in the adhesion between the hydrogel and Substrate X for the range of strains applied. For the Hydrogel A system, there is a significant difference between the results prior to and after applying TTSP. This is not so for the Hydrogel B results, which were less affected by changes in the crack propagation rate and temperature for the range of rates and temperatures investigated. This is expected when observing the shift factors in Figure 5-9 for each hydrogel for the range of temperatures covered. The range of shift factors for Hydrogel A was greater than that for Hydrogel B for the same range of temperatures. This difference between the data collections for each hydrogel system comes into play with fitting the data for each system and determining fracture parameters such as the threshold and critical SERRs.

Curve Fitting of the Master curves

Not only do the master curves provide a greater range of crack propagation rates, but they also provide a better understanding of the behavior of the system. The role of temperature and rate in the shifting gives insight into their influence on the adhesion of the system. The form also gives insight in that regions of the master curve can be observed and used to describe the system. The threshold, critical, and sub-critical region are expressed in Figure 5-12.

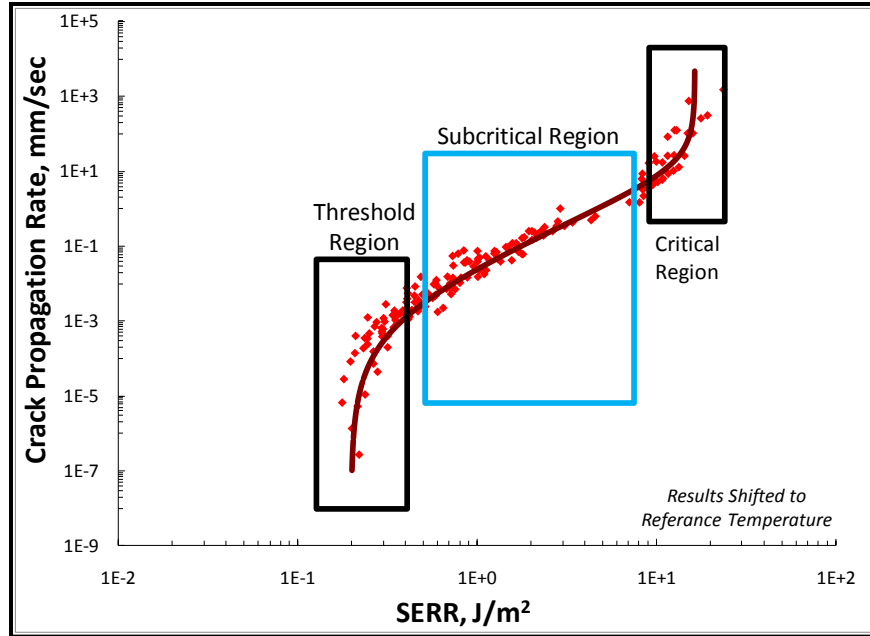


Figure 5-12: Demonstration of da/dt versus SERR curve with Threshold, Subcritical, and Critical Regions for Hydrogel A at $T_{ref} = 45^\circ\text{C}$

The critical region is where the crack propagates at a very high rate. The data in this region was collected at low temperatures and at high crack propagation rates that occur upon wedge insertion. The subcritical region is the region where relationship between the crack propagation rate and the SERR is steady and fairly linear. The crack growth halts in the threshold region where the SERR remains a constant value as the crack propagation rate decreases and approaches zero. The data in this region is that collected at high temperatures and at the low crack propagation rates that occur once the crack growth slows dramatically.

Each master curve was fitted to define the SERR as a function of the crack propagation rate. Fitting the master curve allowed for finding parameters to describe the relationship between the crack propagation rate and the SERR values. Two different models were applied in order to define both the threshold and critical region using the SERR values and crack propagation rates that describe them. The first of these fits is a power law formulation from Park and Kim that describes the critical region in addition to the threshold and subcritical region in Equation (5-1) [41].

$$G(v_{shifted}) = G_{Thresh} + \frac{G_{Crit}}{\left(1 + \left(\frac{v_{Crit}}{v}\right)\right)^n} \quad (5-1)$$

The critical SERR, G_{crit} , is the fracture energy of the system. In order for a crack to initiate, the applied SERR must be equal to or greater than the critical value. In the critical region, the crack is growing at a rapid but decreasing rate as the SERR remains a fairly constant value. It is at the

critical crack propagation rate, v_{crit} , in which the SERR begins to decrease and enter the subcritical region. In the subcritical region, both the SERR and crack propagation rate are decreasing with the slope n . At some point, a threshold SERR and crack propagation rate are reached, represented by \mathcal{G}_{thresh} and v_{thresh} . At this point, the SERR will become fairly constant once again while the rate of crack growth decreases rapidly until the crack appears to halt. This region is described, without the inclusion of the critical parameters, by Williams using another power law formulation shown in Equation (5-2) [42].

$$\mathcal{G}(v_{shifted}) = \mathcal{G}_{Thresh} \left(1 + \left(\frac{v}{v_{thresh}} \right)^n \right) \quad (5-2)$$

By fitting the results with Equations (5-1) and (5-2), the parameters describing the crack propagation and SERR relationship can be used to compare the adhesion of the each hydrogel to Substrate X.

Each fit can be applied to each master curve using the crack propagation rates that were already shifted. If working with results that are not yet shifted, temperature effects can be introduced to either fit in order to find the master curve fit. This can be accomplished by introducing the definition of the shifted velocity and the WLF equation to develop Equation (5-1) into (5-3) and Equation (5-2) into (5-4).

$$\mathcal{G}(v, T) = \mathcal{G}_{Thresh} + \frac{\mathcal{G}_{Crit}}{\left(1 + \left(\frac{v_{Crit}}{v} \left(\frac{-C_1(T - T_0)}{C_2 + (T - T_0)} \right) \right) \right)^n} \quad (5-3)$$

$$\mathcal{G}(v, T) = \mathcal{G}_{Thresh} \left(1 + \left(\frac{v}{v_{thresh}} \left(\frac{-C_1(T - T_0)}{C_2 + (T - T_0)} \right) \right)^n \right) \quad (5-4)$$

The threshold and subcritical regions are apparent for both curves but the critical region is not apparent for the Hydrogel B results. This is due to the crack propagation range investigated for Hydrogel B. The crack propagation rates were not high enough for Hydrogel B results to reach the critical region. As a result, both the Williams and Park fits could be performed on Hydrogel A, but only the Williams fit could be performed on Hydrogel B. The results presented in Figure 5-7 and Figure 5-8 are presented once again in Figure 5-13 and Figure 5-14 along with the Williams fit, described by Equation (5-2), and the Park fit, described by Equation (5-1).

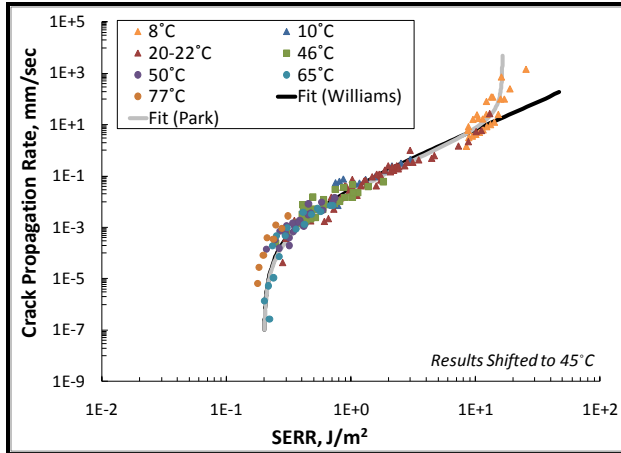


Figure 5-13: Crack Propagation Rate versus SERR Master Curve with Fit for Hydrogel A and Substrate X at $T_{ref} = 45^{\circ}\text{C}$

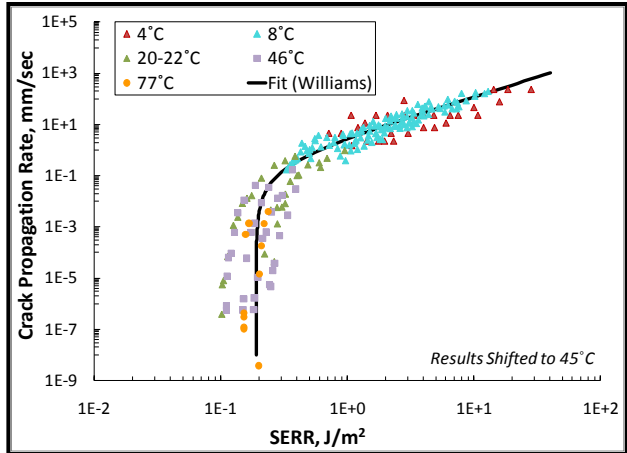


Figure 5-14: Crack Propagation Rate versus SERR Master Curve with Fit for Hydrogel B and Substrate X at $T_{ref} = 45^{\circ}\text{C}$

Both fits could be performed on the Hydrogel A results because the critical region was observed for the range of temperatures and rates tested. However, the power fit from Park does not fit the critical region as well as it fits the threshold region. The threshold region has a much steeper slope than the critical region, allowing for a straight line to fit that data. The SERR values in the critical region continue to increase with a small slope. This means that the critical value determined for Hydrogel A is likely conservative and that the true value is most likely higher. Only the Williams fit could be performed on Hydrogel B due to the critical region not being observed for the range of temperatures and rates tested. However, the fit for each master curve helps provide parameters useful in describing the adhesion of each system.

In order to compare the two hydrogel systems to each other, the master curves and the Williams fit are shown for both hydrogel systems in Figure 5-15.

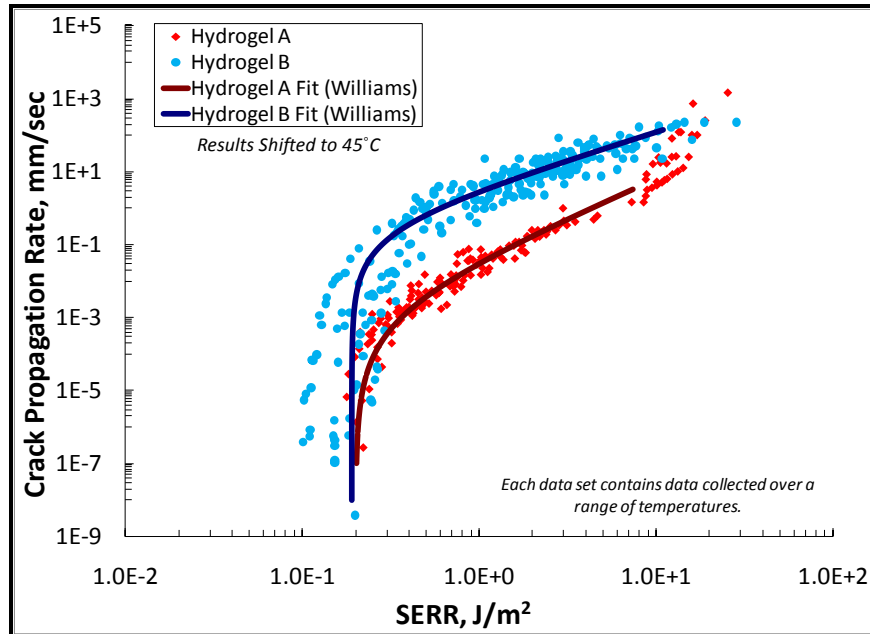


Figure 5-15: Crack Propagation Rate versus SERR Master Curve with Fit for Hydrogel A and Hydrogel B Results at $T_{ref} = 45^{\circ}\text{C}$

The two master curves appear to have approximately the same threshold but Hydrogel A deviates from the threshold region sooner than Hydrogel B. The Hydrogel A system then has a higher SERR value for a given crack propagation rate than the Hydrogel B system until the Hydrogel A reaches the critical region. The two curves cross in this region and the Hydrogel B system then has a higher SERR value for a given crack propagation rate. Although the Hydrogel B system needs a higher crack SERR for crack initiation, crack propagation slows and comes to a halt in the same region for the two hydrogel systems. This was apparent in testing in that the two systems behaved very differently at the initiation of the test. Debonding appeared to initiate with a much higher crack propagation rate for Hydrogel B than Hydrogel A. At long crack lengths, however, the two behave similarly. The parameters for the fits in Figure 5-13 and Figure 5-14 are presented in Table 5-1. Since the critical region for the Hydrogel B results was not characterized, no critical values are presented for Hydrogel B.

Table 5-2: Critical and Threshold Parameters from Fitting each Interfacial Fracture Master Curve¹

	G_{crit}	G_{thresh}	v_{crit}	v_{thresh}	n
Units	J/m^2	J/m^2	mm/sec	mm/sec	$kJ \cdot sec/m^3$
Hydrogel A	16.3	0.199	14.9	0.002	0.467
Hydrogel B	--	0.190	--	0.300	0.659

The two systems have nearly the same threshold SERR but the threshold crack propagation rate for Hydrogel B is two orders of magnitude greater. This means the Hydrogel B system enters the threshold region from the subcritical region at a much higher crack propagation rate than Hydrogel A. Control through rate and temperature is lost sooner with Hydrogel B when decreasing the rate. In addition, once in the subcritical region, a given SERR value correlates to higher crack propagation rate for Hydrogel B than Hydrogel A. Also, the span covered in the subcritical region appears to be greater for Hydrogel B, whose critical region could not be reached. The difficulty in reaching the critical region for Hydrogel B is likely due to the much lower glass transition temperature of Hydrogel B. For the temperatures and rates tested, all the threshold, subcritical, and critical regions of the Hydrogel A master curve could be fitted.

Hydrogel B needs higher crack propagation rates and lower temperatures in order to have rate and temperature play a significant role in the system and to characterize the critical region. This, however, was not done, because the rates and temperatures needed to reach the critical region exceeded the scope of the project and the information needed.

Not only can the two hydrogel systems be compared to each other, but they can be compared to the bulk fracture results for each hydrogel system. In Figure 5-16, the wedge test results for Hydrogel A and Substrate X system is compared to the constrained tension fracture (CTF) test results for the Hydrogel A system [4].

¹ Critical parameters not available for Hydrogel B

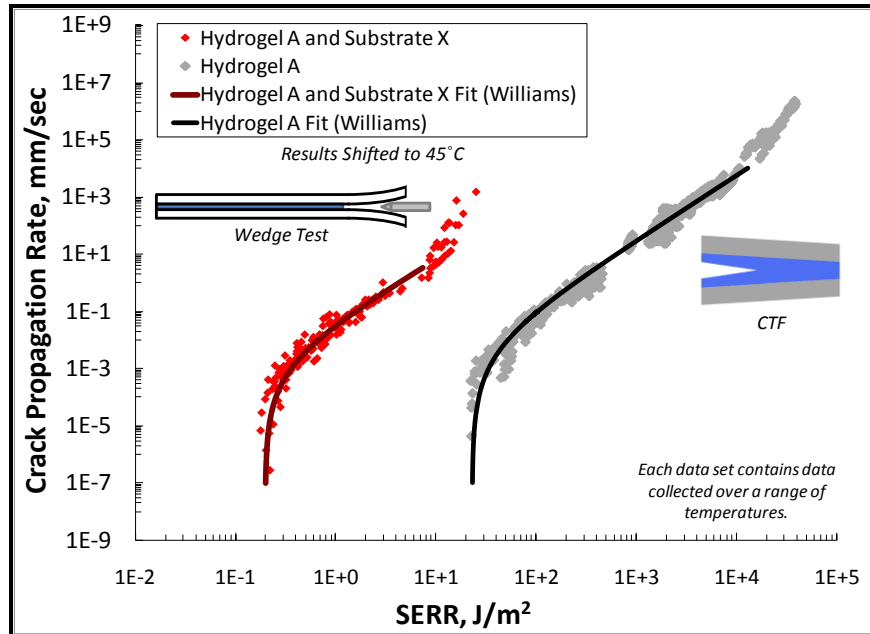


Figure 5-16: Crack Propagation Rate versus SERR Master Curve with Fit for Wedge Test and CTF Results for Hydrogel A at $T_{ref} = 45^{\circ}\text{C}$

The interfacial and cohesive fracture curves for Hydrogel A have similar crack propagation rates but the SERR values for the CTF results are consistently about two decades greater. The cohesive fracture SERR values are expected to be greater as debonding is desired to occur between Hydrogel A and Substrate X without damage occurring to the hydrogel. The critical SERR for the wedge test results, $16.3\text{J}/\text{m}^2$, is comparable to the threshold SERR value for the CTF results, $22.7\text{J}/\text{m}^2$. This means the energy needed to initiate an interfacial failure could continue a cohesive failure. However, any energy needed to initiate debonding would not cause cohesive failure in the region investigated. In the temperature and rate range tested, debonding was expected and observed to occur without cohesive fracture.

In Figure 5-17, the wedge test results for Hydrogel B and Substrate X system are compared to the constrained tension fracture (CTF) test results for the Hydrogel B system [4].

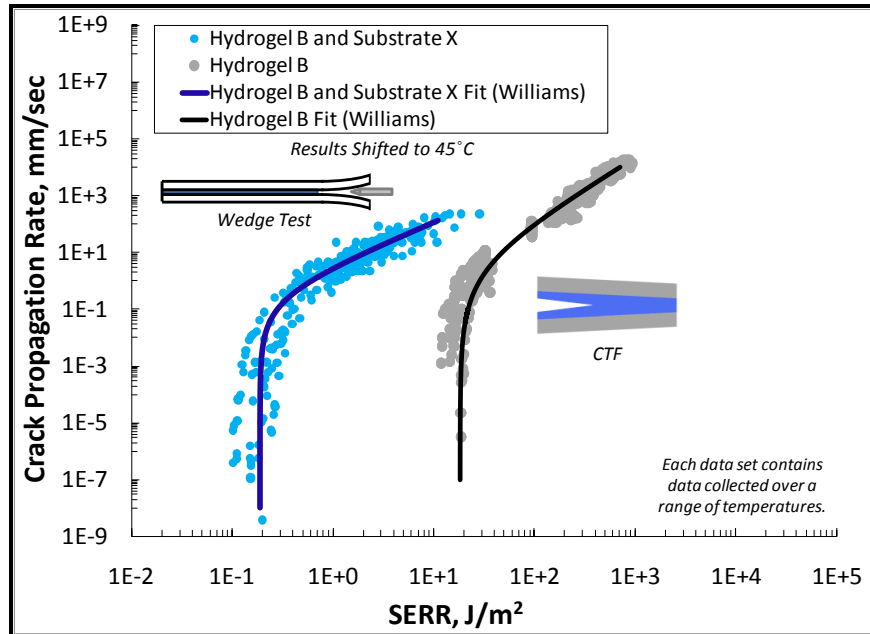


Figure 5-17: Crack Propagation Rate versus SERR Master Curve with Fit for Wedge Test and CTF Results for Hydrogel B at $T_{ref} = 45^{\circ}\text{C}$

The two Hydrogel B curves compare to each other similarly as the two Hydrogel A curves. However, for Hydrogel B, the slope of the subcritical region of the interfacial fracture curve appears to be lower than that for the cohesive fracture curve. As a result, the two decade difference in the threshold region reduces to slightly less than one decade at the crack propagation rate of $1000\text{mm}/\text{sec}$. Since the critical region was not reached for either Hydrogel B curve, it is unknown whether the two curves cross at some point, possibly resulting in undesired fracture of the hydrogel during debonding. In the range observed, the SERR values for the wedge test results remain below that for the CTF results for a given crack propagation rate. In the temperature and rate range tested, debonding is expected to occur without cohesive fracture of the hydrogel occurring. This is what was observed during testing. However, it appears possible that higher crack propagation rates and lower temperatures could have different results.

Full Results

The results presented in Figure 5-1 through Figure 5-17 do not represent all of the data collected throughout this research. Data was excluded for various reasons. Mainly, the experimental method was refined substantially as the research progressed to address variability and other issues. Experimental results that were collected prior to implementation of the final experimental method were removed from Figure 5-1 through Figure 5-17. The results for all of the data collected are shown for Hydrogel A in Figure 5-18 and for Hydrogel B in Figure 5-19 prior to shifting.

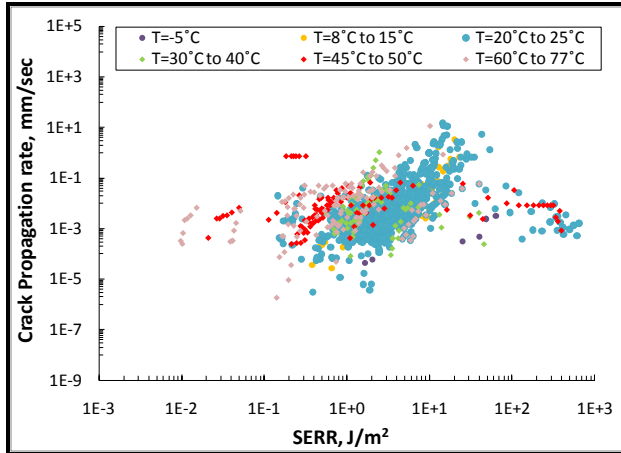


Figure 5-18: Crack Propagation Rate versus SERR Prior to Shifting for All Hydrogel A and Substrate X

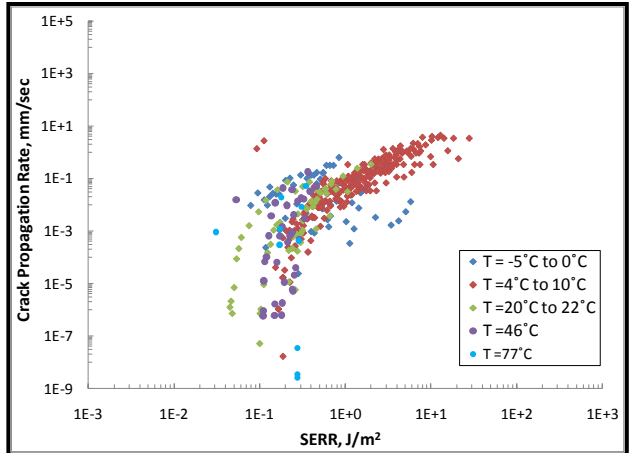


Figure 5-19: Crack Propagation Rate versus SERR Prior to Shifting for All Hydrogel B and Substrate X

The shifted results along with the Park fit for Hydrogel A and the Williams fit for Hydrogel B are shown in Figure 5-20 and Figure 5-21, respectively. The Park and Williams fit allow for orientation in comparing the overall results to the results presented in Figure 5-13 and Figure 5-14.

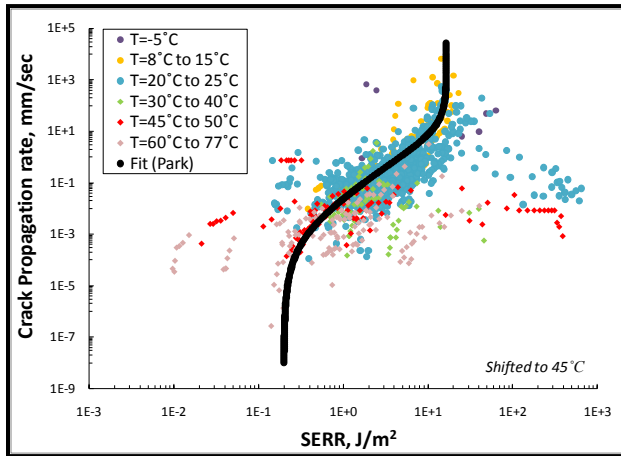


Figure 5-20: Crack Propagation Rate versus SERR Prior to Shifting for All Hydrogel A and Substrate X Data at $T_{ref} = 45^\circ\text{C}$

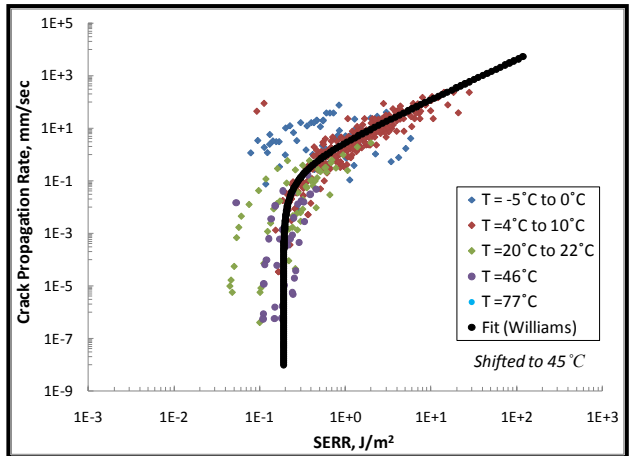


Figure 5-21: Crack Propagation Rate versus SERR Prior to Shifting for All Hydrogel B and Substrate X Data at $T_{ref} = 45^\circ\text{C}$

Changes were made in the experimental method throughout the project in order to remove sources of variation. Changes included reducing the time between curing and testing, increasing the time for each step during the sample preparation, preparing samples with high confinement of the hydrogel interlayer, method of temperature control, method of data collection, and increased documentation. Hydrogel A samples were used in developing the final experimental method. For this reason, there is a large amount of scattered Hydrogel A data. Much of the Hydrogel B testing was done after developing the final experimental method so that much of the data collected for Hydrogel B was used to build the master curve in Figure 5-11.

In working with these hydrogel systems, it was found that meticulous documentation is needed to note possible reasons for variation, bridging, and other phenomena observed. However, this was not fully realized early in the project when much testing was performed on Hydrogel A. This is another reason for the large amount of varied Hydrogel A data in Figure 5-20. Much of the early testing of Hydrogel A did not involve taking images of the wedge test but relied on observing and recording the crack length during the test. It was found that this method resulted in much error that could not be checked at a later point. Future work with these hydrogels should involve detailed documentation as well as standardized testing and careful data collection. Sources of possible variation that were investigated with side studies include the effects of waiting to test the specimen at increased periods of time after curing and preparing specimens with low confinement.

Effects of Aging

Testing at Discrete Times after Curing

A set of Hydrogel B and Substrate X samples were cured and held in the 65°C nitrogen environment. Once the samples were removed from the chamber, they were immediately measured, prepared, and tested at room temperature. Images of some of these samples are shown in Figure 5-22 in which the time provided is the time between when the specimens were done curing and when the wedge was inserted.

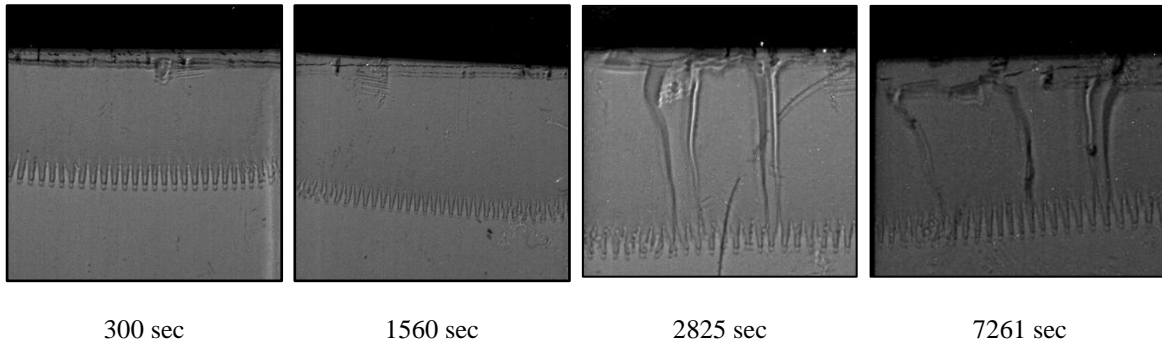


Figure 5-22: Hydrogel B Samples with Wedge Inserted at Discrete Times after Curing

Bridging, referring to the crack switching from one surface to another and shown by the schematic in Figure 5-24, tended to occur in samples tested more than 2700 seconds after curing.



Figure 5-23: Schematic of Bridging

During much of the testing, bridging was seen for both hydrogel systems. However, the amount of bridging varied between samples. Some samples did not exhibit any bridging while others had

one or multiple bridges. These bridges would typically appear at the beginning of the test and ‘pinch’ off at some point, as shown in Figure 5-24.

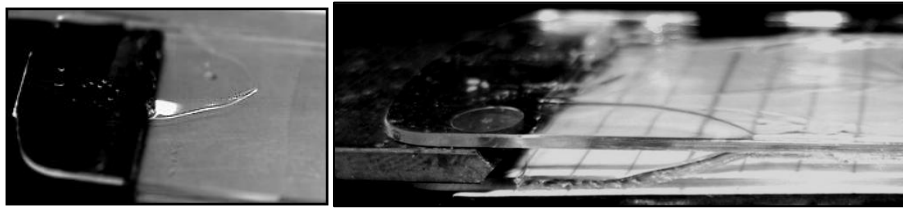
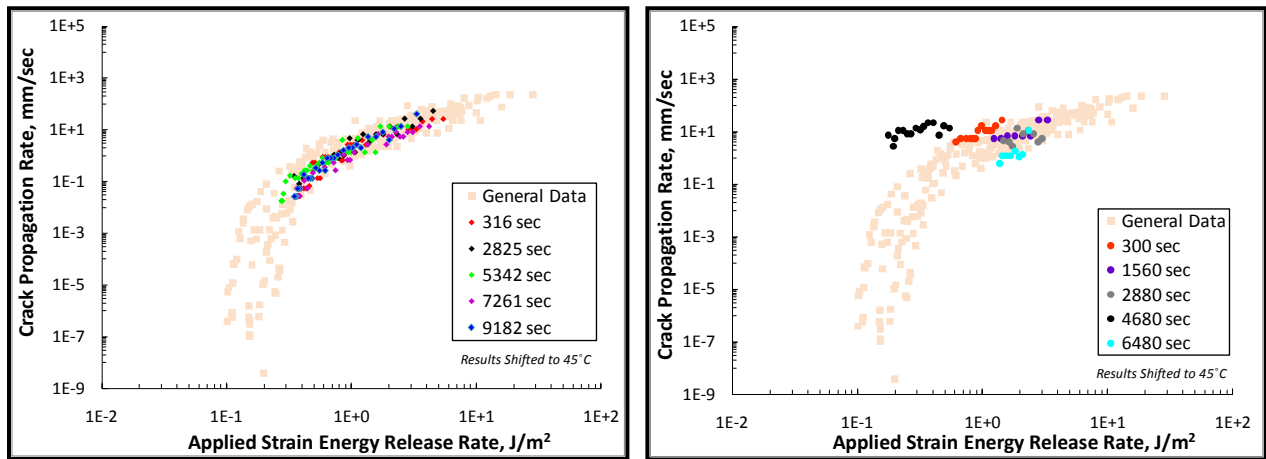


Figure 5-24: Bridging during Wedge Testing

The reasons for bridging are of interest since bridging is believed to result in cohesive failure or tearing of the hydrogel during the manufacturing process for applications of these materials. The main reason for bridging is not readily apparent and appears to be due to a mixture of different factors. However, since bridging did not appear in samples tested prior to 2700 seconds after curing, time was determined to be one of the factors. The effect on the results varies. Some results appear to be in line with the master curve of the wedge test results and other results appear very different, as shown by the Hydrogel B results at room temperature in Figure 5-25.



Sample Set 1 at $T_{ref} = 45^{\circ}\text{C}$

Sample Set 2 at $T_{ref} = 45^{\circ}\text{C}$

Figure 5-25: Hydrogel B Samples - Wedge Inserted at Discrete Times after Curing at 22°C

The samples sets represented in Figure 5-25 and Figure 5-25 remained in the heated and nitrogen environment after curing. At discrete times after curing, a specimen was removed from the chamber and immediately measured and tested at room temperature. Each sample set shown in Figure 5-25 was performed on different days. The results for the Sample Set 1 are within the mastercurve for the wedge test data for Hydrogel B and Substrate X despite the bridging in samples tested at least 27000 seconds after curing. The results for Sample Set 2 are very different and appear to have erratic results between specimens. The reason for the large difference between the two sample sets is not completely understood. There are some possible answers. One possibility is that there were issues due to the monomer used for the Sample Set 2. When

making these samples, it appeared that the monomer was congealing prior to curing. This is the only set of samples in which this occurred and could be the cause of the erratic behavior.

The behavior of the samples that were held at a low temperature prior to and during crack propagation was very different. None of the Hydrogel B samples in which the wedge was inserted at discrete times after curing at a temperature of 4°C had bridging. However, the results did not align with the master curve for the wedge test results, as shown in Figure 5-26.

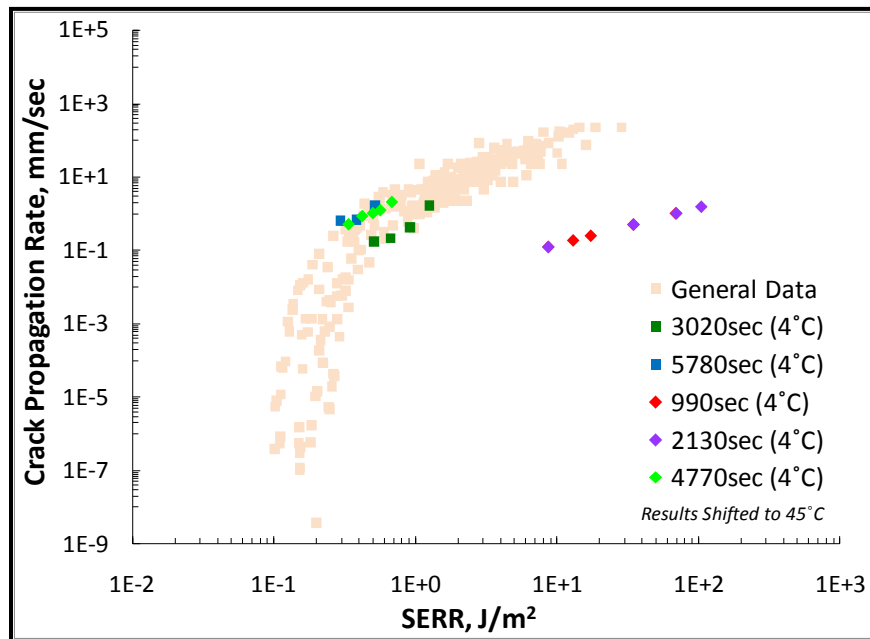


Figure 5-26: Hydrogel B Samples Tested at 4°C at Discrete Times after Curing Compared to General Wedge Test Results

This demonstrates that the temperature affects the occurrence of bridging. Bridging occurs with aging unless the specimen is kept at a low temperature prior to and during the initiation and propagation of debonding.

Some Hydrogel A samples were tested eight days after curing. After being cured, these samples remained in a room temperature and air environment until tested. The results are presented in Figure 5-27.

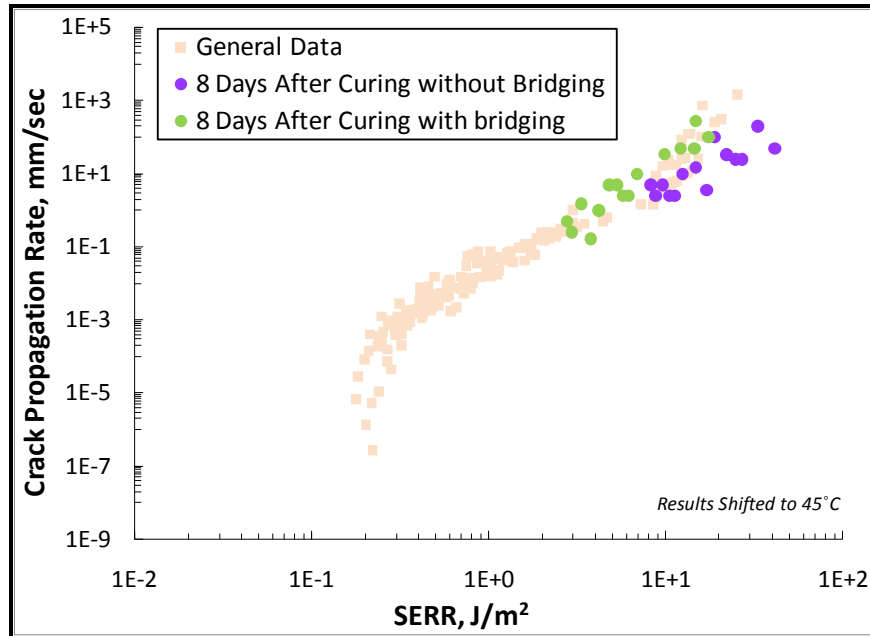


Figure 5-27: Hydrogel A Samples Tested at 22°C approximately 7 Days after Curing Compared to General Wedge Test Results at $T_{ref} = 45^{\circ}\text{C}$

Observing the results from Figure 5-27, it appears that increased time after cure could lead to an increased critical SERR. However, there are not enough results to substantiate this hypothesis.

It appears that the results after increasing the time between curing and wedge insertion may or may not be consistent with the former characterization of the system. In addition, bridging more often occurs in Hydrogel B samples with an increased amount of time between curing and wedge insertion unless testing at low temperatures. For the Hydrogel B samples, it appears that increasing the time between curing and wedge insertion can allow for any flaws in the specimen to have a greater influence on the system by resulting in erratic SERR values and bridging. Flaws can cause the debonding to switch interfaces or for the adhesion of the system to decrease. Decreasing the temperature increases the energy needed for debonding and increases the energy dissipation within the interlayer, which prevents flaws from causing bridging. The bridging, erratic SERR values, or both bridging and erratic SERR values are seen in most Hydrogel B sample tested more than 2700 seconds after curing. This is true for the samples tested at room temperature and in the cold temperature.

Change in the Specimen with Time

To further investigate reasons for the changes in the behavior with time following curing, the mass and thickness were tracked as time passed after curing. Bonded wedge test specimens were prepared in order to measure and record their mass over time. A wedge was not inserted into these samples at any time. The change in the mass of the hydrogel, m , is shown with respect to the first measurement, m_0 , for each of these specimens in Figure 5-28.

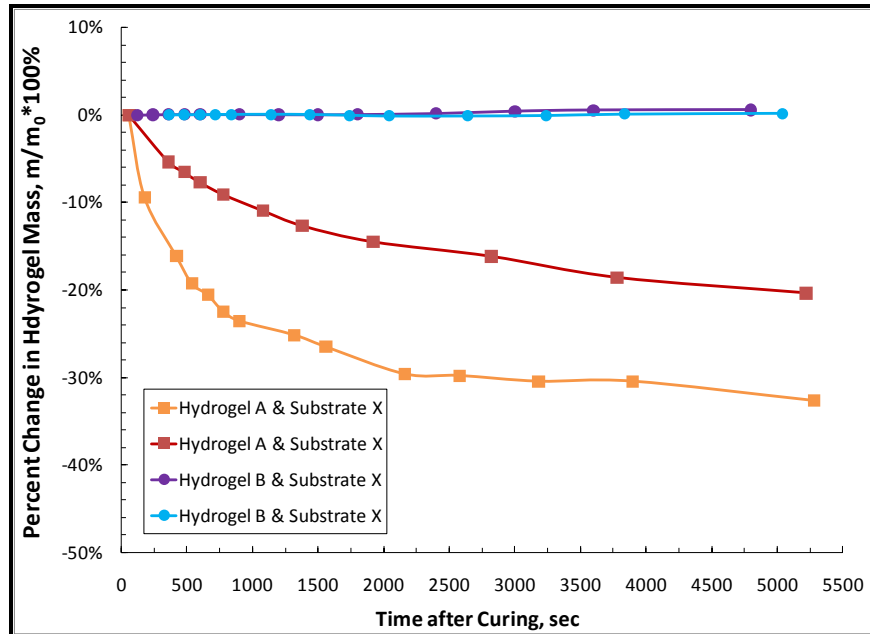


Figure 5-28: Percent Change in Hydrogel Mass over Time

The mass decreased with time for Hydrogel A and remained constant for Hydrogel B. Similar results were found by Tizard when investigating the bulk behavior of these systems [4]. The mass loss shown by Hydrogel A over time is assumed to be solvent loss. Solvent loss can affect the material behavior. However, the solvent loss does not appear to affect the behavior or results of the Hydrogel A specimens over time. The behavior of Hydrogel B, on the other hand, does appear to be affected by time, but there appears to be little solvent loss for the Hydrogel B results. One possibility is that solvent loss helps to induce dissipative fracture, preventing issues that could occur with time such as bridging. This is a similar effect as the lower temperature preventing bridging. Hydrogel A, overall, had fewer issues in testing. That is, once the experimental method was established, there appeared to be more consistent results for Hydrogel A than B. Hydrogel A also has higher solvent loss over time. The solvent loss may help stabilize the behavior and prevent flaws within the system to affect the adhesion or cause bridging. Another consideration is the higher crosslink density of Hydrogel A.

For both hydrogel systems, the thickness of the hydrogel interlayer would fluctuate over time without any consistent trend of increasing or decreasing. The change in the thickness of the hydrogel interlayer in the center of the specimen is shown in Figure 5-29, with a fifteen percent error because this was the variation in the hydrogel interlayer thickness during testing.

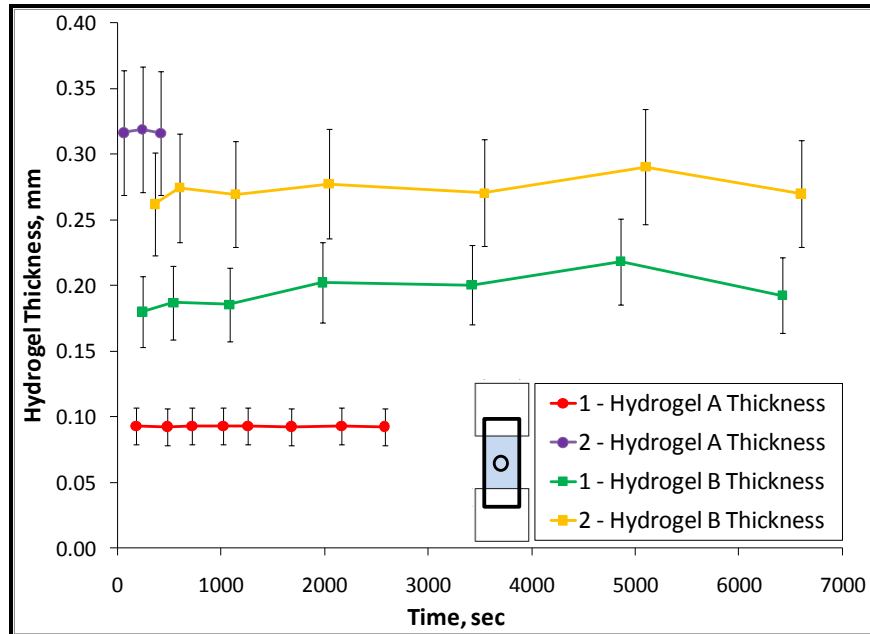


Figure 5-29: Hydrogel Interlayer Thickness at Center of Sample versus Time

None of the samples had a consistent increase or decrease in the thickness, and the reasons for the fluctuations are unknown. The Mitutoyo® digital indicator has a reported accuracy of 0.0015mm.

The thickness of the specimen did not change for Hydrogel A or Hydrogel B, the mass decreased for Hydrogel A and not for Hydrogel B, and initial debonding would occur around the edges of the specimens for both systems. This leads to the conclusion that a higher amount of solvent loss occurs in Hydrogel A. Since the debonding occurs in both hydrogel systems, it could be due to residual stress from being cured at a higher temperature.

The observations of the effects of time after cure provide further insight into possible factors for the adhesion of each system of interest. However, the testing performed led to many questions and concerns as well. The changes that occur appear to be influenced by time, temperature, solvent loss, and residual stresses. Similar but more extensive studies could provide more answers to the behavior variability of these systems.

Effects of Confinement

An undulating crack front was observed in the during the wedge tests which strengthens the understanding that the confinement of the interlayer is largely dependent on the ratio of the adherend to the hydrogel thickness. Confinement of the elastomer interlayer can be described by the confinement parameter, α , described by Equation (5-4) [37].

$$\alpha = \left(\frac{D}{Gh^3} \right)^{1/3} \quad (5-5)$$

The role of confinement was investigated because it was believed to play a role. Specimens prepared to demonstrate the difference between high confinement (undulating crack front) and low confinement (straight crack front) are shown in Figure 5-30.

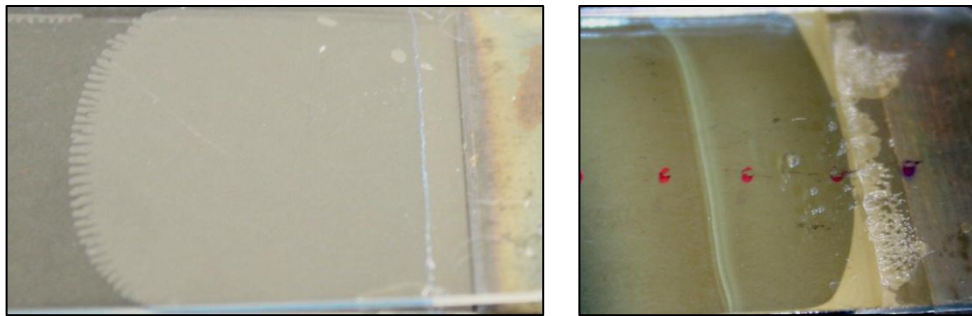


Figure 5-30: Specimens of High Confinement (Undulating Crack Front) and Low Confinement (Straight Crack Front)

Highly confined specimens had the undulating pattern at the crack front while specimens that were not highly confined had a non-undulating crack front. These results are similar to that shown in past studies in which the undulating crack front would appear if the confinement was above some critical value [37, 43]. A comparison of such specimens is presented in Figure 5-31. Specimens with a confinement parameter below 10 had a straight crack front and those with a confinement parameter greater than 20 had an undulating crack front.

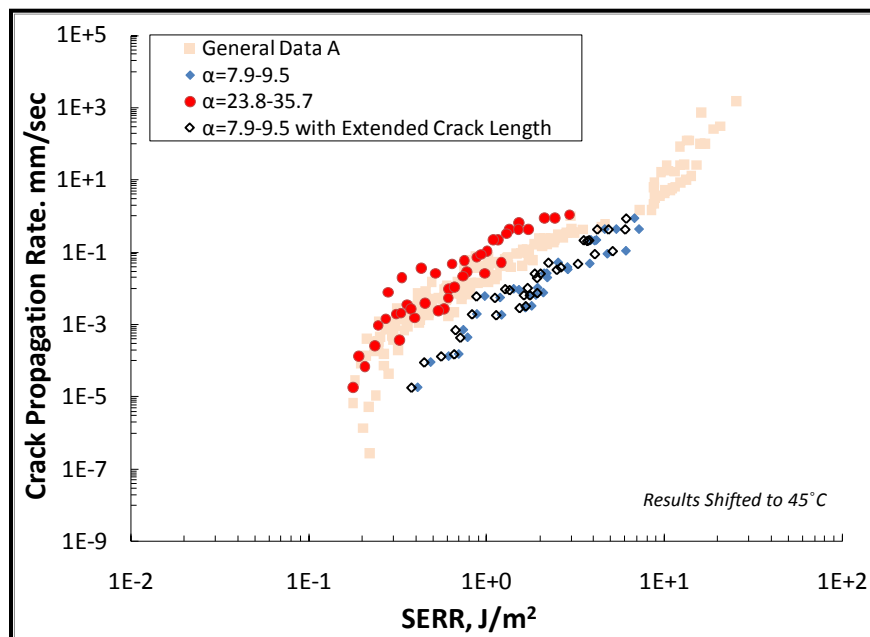


Figure 5-31: Comparison of SERR Values for Specimens with High and Low Confinement

The resulting SERR values for samples with a confinement parameter below 10 were greater than for the samples in with a confinement parameter above 20, as shown in Figure 5-31. The specimens with a confinement parameter above 20 aligned with the master curve for the wedge test results. The analytical model for determining the SERR removed variation due to thickness. However, there remains variation between specimens with and without high confinement. One reason for the difference could be that the analytical model developed in Chapter 4 was based on the case of a highly confined interlayer similar to the work done by Ghatak, Chaudhury, and Dillard [21, 23, 43]. In addition, decreasing the confinement of the hydrogel interlayer can allow for viscoelastic dissipation to play a greater role and change the mode of deformation for the interlayer, resulting in a change of the measurement of the adhesion of the system [20].

In addition to the tests in which different interlayer thicknesses were investigated, wedge test specimens with thick adherends were prepared and tested. These specimens had an interlayer thickness much greater than that for the majority of the wedge tests performed but still highly confined due to the Substrate X adherends with a greater thickness. As expected, the resulting crack front was undulating for both specimens because of the high confinement of the interlayer. The results for these specimens with a large adherend thickness were very similar to the master curve for the wedge test results as expected and shown in Figure 5-32.

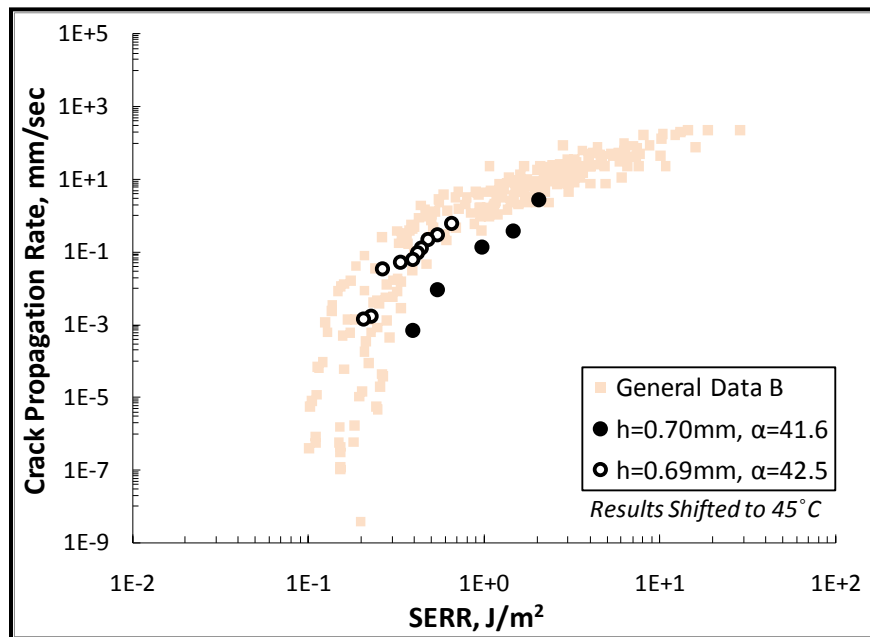


Figure 5-32: Hydrogel B and Substrate X Test with Thick Adherends

From Figure 5-32, the thick wedge test samples, in which the interlayer is very thick yet still highly confined, have results that align with the mastercurve for Hydrogel B. This further establishes the difference between a thin hydrogel interlayer and a highly confined interlayer. Since the adherends used for the collecting the general wedge testing were very thin (0.7mm - 1mm), the interlayer needed to be thin to remain highly confined. Although the results appear to

be affected if the interlayer is not highly confined, as shown by Figure 5-31, the results do not appear to be affected if the interlayer is very thick and yet highly confined due to thick adherends.

The wedge test results used to form the master curves for each hydrogel system were collected for specimens with a highly confined elastomeric interlayer. This prevented variation that could occur due to using specimens that are highly confined and specimens that are not.

Three-Point Bend Results for Substrate X

The three point bend testing on Substrate X in the in the screw-driven test machine was performed at room temperature on a set of three Substrate X adherends. Each specimen was subjected to five runs in which no permanent yielding occurred. The flexural stress versus strain curves for all runs on the screw-driven test machine are shown in Figure 5-33.

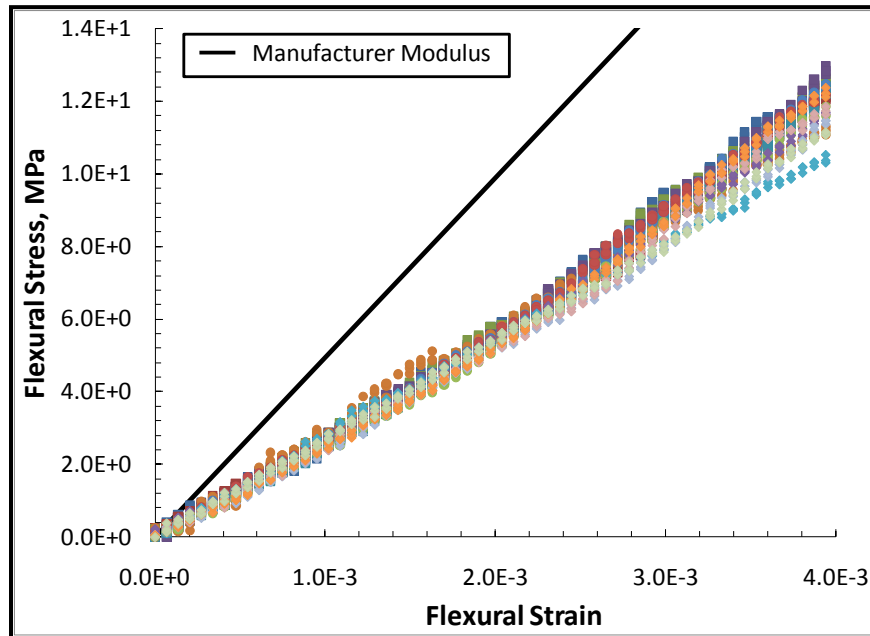


Figure 5-33: 3-Point Bend Tests on Substrate X in Screw Driven Testing Machine

The average resulting modulus using the screw-driven testing machine is $2765 \pm 114 \text{ MPa}$, which is 24% higher than the value reported by the manufacturer.

Some Substrate X specimens were tested in the DMA and underwent temperature and frequency sweeps within ranges of $35\text{-}80^\circ\text{C}$ and $1\text{-}21.5 \text{ Hz}$, respectively. The resulting modulus values are fairly consistent despite the range of frequencies and temperatures, as shown in Figure 5-34.

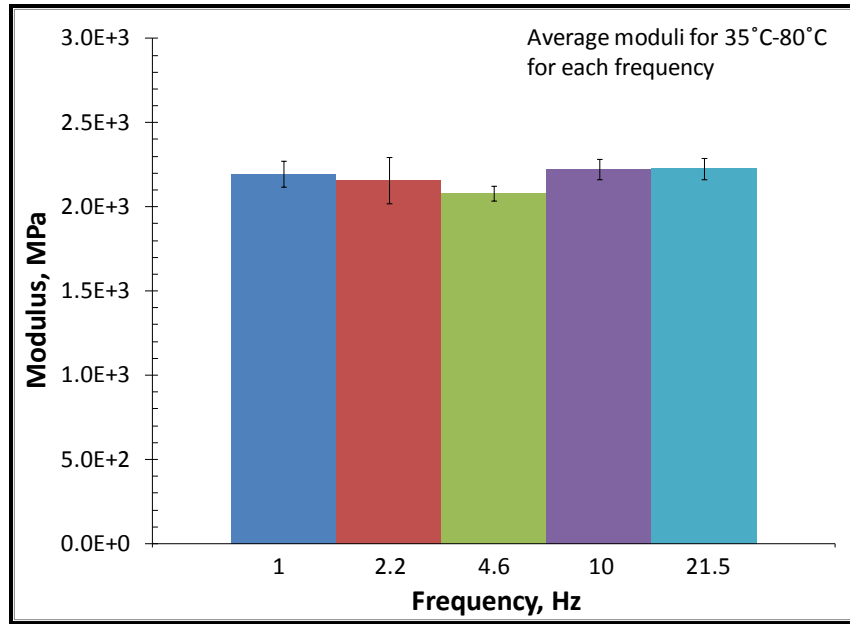


Figure 5-34: Three-Point Test on Substrate X in DMA

The average value of the modulus using the DMA for temperatures 35°C to 80°C and frequencies 1Hz to 21.5Hz is $2177\pm 98\text{MPa}$, which is equivalent to the value provided by the manufacturer. In addition, the modulus was determined to have insignificant variation with changes in temperature. Therefore, a constant value could be applied to wedge test results collected over a range of temperatures.

The difference in the modulus determined by the three-point bend testing in the screw-driven testing machine did not aid in validating the value provided by the manufacturer, but the value from the DMA did. The value of 2.1GPa from the manufacturer was chosen to be applied for the analysis. This was due to the DMA results matching the testing performed on the material by its manufacturer.

Summary

This chapter presented the results from the experimental methods described in Chapter 3. The raw data consisted of the crack length measurements at discrete times during the wedge test. The analytical model developed in Chapter 4 was applied in order to find the applied SERR values from the crack length measurements.

The crack propagation rate was then plotted against the applied SERR values, which resulted in disconnected curves that were each correlated to the temperature at which the testing was performed. These crack propagation rate versus applied SERR curves were then shifted to form master curves by applying TTSP to cover a wide range of applied SERR and crack propagation values. The ability to develop these master curves using the WLF equation-based shifted factors developed for the bulk behavior of the hydrogel systems demonstrated that the viscoelastic

nature of the hydrogel systems is a significant factor in the adhesion of each hydrogel system to the Substrate X. In addition, the smaller range of shift factors for Hydrogel B for the same temperature range demonstrated that the Hydrogel B system was less affected by TTSP in the range of temperatures observed.

Curve-fitting was performed for each master curve in order to define parameters useful in characterizing the adhesion of each system. These parameters described the applied SERR and crack propagation values at which each system entered and exited the subcritical region and allowed for comparison of the two systems. The power fits of the interfacial fracture curves were compared to the power fits of the cohesive fracture curves for Hydrogel A and Hydrogel B. For Hydrogel A, it was observed that the interfacial and cohesive fracture similar manner but with the cohesive applied SERR approximately two decades greater for a given crack propagation rate. However, the close vicinity of the interfacial fracture critical SERR and the cohesive fracture threshold SERR lead to the conclusion that the energy needed to initiate an interfacial fracture could also continue a cohesive failure. Critical SERR values were not collected for the interfacial fracture nor the cohesive fracture results for Hydrogel B. Although the threshold SERR for the cohesive fracture is much greater than that for the interfacial fracture, the difference is unknown for the critical values. However, the slope of the subcritical region is lower for the interfacial master curve. This could result in the two master curves crossing at higher rates and lower temperatures. A cross between these two could result in cohesive fracture occurring when debonding is desired.

Side studies, described in Chapter 3, were performed to learn more about the effects of increasing the time between curing and wedge insertion, the effects of the confinement hydrogel interlayer, and the parameters of the Substrate X material. It was established that as time passes after curing, the thickness of Hydrogel A and Hydrogel B specimens does not change, within the accuracy of the technique applied, and the mass of Hydrogel A specimens decreases. In addition, initial debonding would occur around the edges of the specimens for both systems. The effects of time after cure on the wedge test results are unclear for both hydrogels. However, it does seem that the increased time allows for bridging to occur for Hydrogel B specimens unless tested at lower temperatures, when energy dissipation is high. The increased energy dissipation at low temperatures may cause a reduction of initiation sites that could cause bridging to occur. Due to the much lower glass transition temperature of Hydrogel B, lower temperatures would be necessary to reach high enough energy dissipation to reduce bridging than for Hydrogel A.

From the side study on the effects of the confinement of the hydrogel interlayer, it was found that confinement plays a role in the adhesion of the system. For the large scale wedge tests performed, samples had varying hydrogel interlayer thickness but all samples were kept at high confinement such that the undulating crack front occurred. This was done due to the intended of these materials involving high confinement of the hydrogel. The analytical model applied was successful in removing the effects of the thickness of the hydrogel interlayer on the resulting applied SERR value. However, it was found that samples with low confinement not only had a

straight crack front, but also had higher applied SERR values. This could be due to the analytical model being derived for the case of high confinement. This could also be the confinement affecting the adhesion or energy dissipation of the system.

From the side study on the effects of the parameters of Substrate X, the elastic modulus value from the manufacturer was not confirmed but there was not enough evidence to change the value. In addition, changes in temperature were found to not affect the behavior of Substrate X in the range of temperatures at which wedge testing was performed. This was useful information for the analysis of the wedge test results since the wedge test was performed over a range of discrete temperatures.

Chapter 6: Numerical Modeling

Introduction

The goals of the finite element modeling effort were to validate the analytical model and to develop a finite element model of the interfacial fracture that occurs between each of the semi-interpenetrating (S-IPN) silicone hydrogels and the cyclo-olefin polymer (COP). First, a finite element model without debonding was developed to model the rotations and deflections that occur at the root due to the interlayer and compare the behavior to the analytical model. Then, a cohesive zone model (CZM) with debonding was developed by applying cohesive zone elements and the fracture parameters determined by experimental and analytical results. This model was also compared to the analytical model and provided further insight into the behavior of each hydrogel and COP system.

Manual Crack Growth

The manual crack growth model did not have debonding. Its purpose was to study the rotations and deflections at the root of the bond termination.

Methods

Half of the wedge test configuration was modeled, as shown in Figure 6-1, and assumed to be symmetrical about bottom edge, which used the mid-plane of the hydrogel interlayer in the complete wedge test configuration.



Figure 6-1: Finite Element Configuration for the Manual Crack Growth Method

Two parts representing the adherend and interlayer were tied together at the interface to prevent separation once the load was applied. The bottom edge of the interlayer was restricted in the vertical direction. One end of the adherend was fixed in the horizontal direction, and a displacement was applied in the vertical direction at the opposite end. The interlayer was prescribed a shorter length than the adherend and the two parts were aligned at the opposite end of the point of loading. The area near the point of loading in which the interlayer was not present was referred to as the crack length for the manual crack growth model, even though it is not a crack but an unbonded area. The crack length was defined by the difference in length between the interlayer and adherend, a , as shown in Figure 6-2.

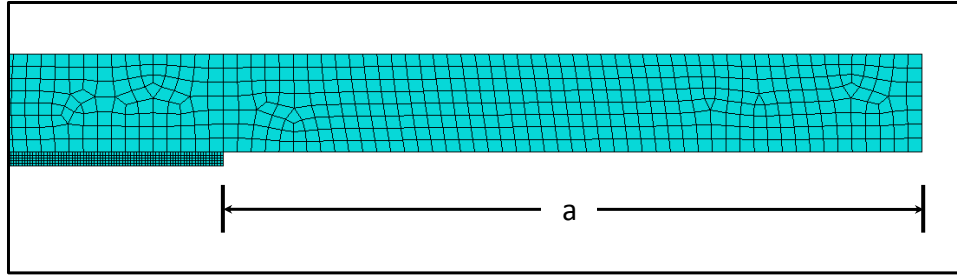


Figure 6-2: Prescribed Crack Length for Manual Crack Growth

Each adherend was described as an isotropic elastic material with a modulus of 2.1GPa and a Poisson's ratio of 0.41 . These are the same values applied for the analysis of the experimental and analytical results. In order to determine the mesh size necessary to have accurate behavior within each finite element model, three point bend testing was applied to the adherend within Abaqus. This allowed for determining the maximum element size for accurate behavior. That is, it was desired to find the maximum mesh size that would result in a stress-strain relationship that correlated to the prescribed elastic modulus of the material. The test method and results are presented in Appendix A. The following mesh sizes were investigated: 0.035mm , 0.07mm , 0.1mm , 0.2mm , and 0.35mm . The percent error of each mesh size in comparison to the expected behavior using simple beam theory was calculated for the reaction force at the point of loading. The mesh size of 0.1mm had a percent error of less than 2% and was determined to be a good balance between accuracy and efficiency.

The hydrogel interlayer could not be defined in Abaqus as an elastic and isotropic material due to the high strains that occur with the low moduli of the hydrogels. To allow for strains higher than five percent, the limit for an elastic material in Abaqus, the hydrogel interlayer was defined as a hyperelastic material with a neo-Hookean fit. It was shown in past work on both hydrogel systems that each can be described with a neo-Hookean fit for strains under 80% [4]. The coefficients applied in Abaqus for the neo-Hookean fit, C_{10} and D_1 defined in Equation (6-1) and Equation (6-2), were determined using the shear modulus (G_a), Poisson's ratio (ν_a), and bulk modulus (K_a) of each hydrogel [27].

$$C_{10} = \frac{G_a}{2} \quad (6-1)$$

$$D_1 = \frac{2}{K_a} = \frac{3(1-2\nu)}{G_a(1+\nu)} \quad (6-2)$$

Since the hydrogels are viscoelastic, the shear moduli values depend on the frequency or rate. For Hydrogel A, the shear modulus value of 199kPa , measured at 20°C and 1mm/sec , was applied. For Hydrogel B, the shear modulus value of 75kPa , the average of the values measured over the range of temperatures and rates, was applied. This allowed for demonstrating the difference of the Hydrogel B behavior compared to Hydrogel A due to a much smaller shear

modulus. The second coefficient, D_1 , can be set to zero to describe the interlayer as fully incompressible. A comparison of the nearly incompressible and fully incompressible conditions is further discussed in the results for the manual crack growth. Due to the small thickness of the hydrogel interlayer, a fine mesh of $0.03mm$ to $0.05mm$ was prescribed.

Models were run that covered a range of applied displacements, shear modulus values of the interlayer, and thickness values for the interlayer. In general, models were tested as fully incompressible, but some models were run with the Poisson's ratio value of 0.499 for comparison. Each model had a combination of the values in Table 6-1.

Table 6-1: Finite Element Parameters for Adherends for Manual Crack Growth

Modulus	E	GPa	2.1
Poisson's Ratio	ν	--	0.41
Length	L	mm	100
Thickness	t	mm	0.70
Applied Disp.	δ	mm	0.10
Width	b	mm	1.0
Mesh Size	ES	mm	0.10
Elements	CPE4I	4-node bilinear plane strain quadrilateral, incompatible modes	

Table 6-2: Finite Element Parameters for Interlayer for Manual Crack Growth

Shear Modulus	G_a	kPa	199, 75
Poisson's Ratio	ν	--	0.499, 0.5
Thickness	h	mm	0.10, 0.30
Width	B	mm	1
Mesh Size	ES_a	mm	0.02
Elements	CPE4H	4-node bilinear plain strain, hybrid, constant pressure	

The compliance at the point of loading was compared between the two models. For the finite element model, the compliance, C , was determined by the deflection, U_2 , and reaction force, RF , at the point of loading, as shown by Equation (6-4).

$$C_{FE} = \frac{U_2}{RF} \quad (6-3)$$

For the analytical model, the compliance was determined using the deflection equations developed in Chapter 4, the deflection at the point of loading in the finite element model, and the effective crack length of the finite element model. Equation (6-4) was applied to calculate the compliance for the analytical model.

$$C_A = \frac{6 + 12(a\lambda) + 9(a\lambda)^2 + 2(a\lambda)^3}{6Db\lambda^3} \quad (6-4)$$

Results

The effect of the bulk modulus, which is very important for cases of high confinement such as the system tested, was observed by comparing finite element results with different bulk modulus values. The bulk modulus values of interest were based on the Poisson's ratio values of 0.5 and 0.499 since the Poisson's ratio of each hydrogel is believed to be within the range of 0.499 and 0.5. A comparison of the compliance at the point of loading with crack length is presented in Figure 6-3.

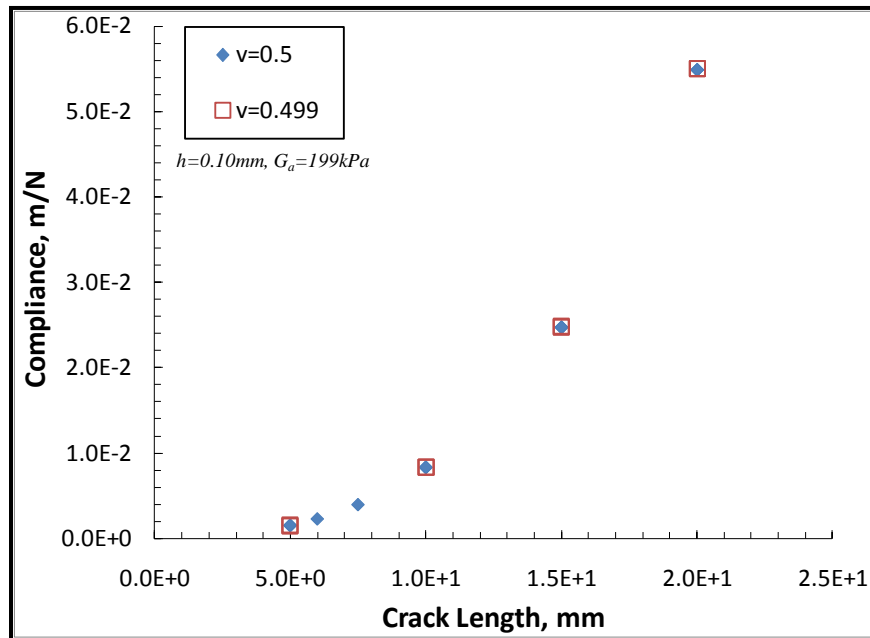


Figure 6-3: Comparison of Compliance versus Crack Length for Different Poisson's Ratio Values

The compliance for model in which the Poisson's ratio was set at 0.499 was less than two percent higher than for a Poisson's ratio of 0.5 for the range of values in Figure 6-3. The Poisson's ratio is not known for either hydrogel, but most hydrogels have a Poisson's ratio of between 0.499 and 0.50. The small difference in Figure 6-3 shows that an estimate for Poisson's ratio within the range of 0.499 and 0.50 suffices and that the value will not have a significant effect on the results for the range observed.

A comparison of the compliance at the point of loading with crack length is shown for the finite element and analytical models for two different interlayer thicknesses in Figure 6-4 for Hydrogel A and Figure 6-5 for Hydrogel B.

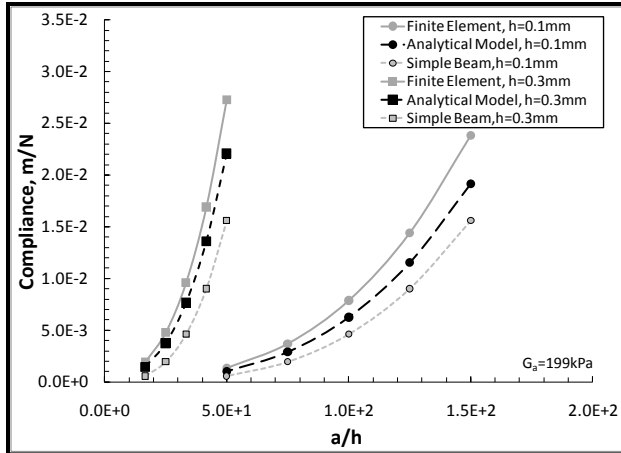


Figure 6-4: Compliance at Point of Loading v. Crack Length for Increasing Crack Length for Hydrogel A

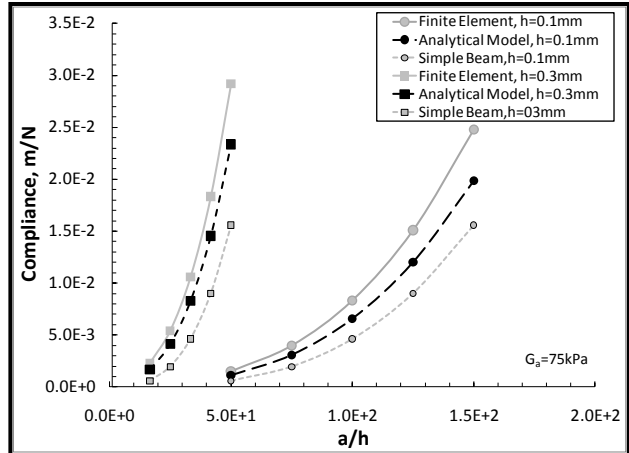


Figure 6-5: Compliance at Point of Loading v. Crack Length for Increasing Crack Length for Hydrogel B

For both systems, the analytical model provided compliance values that were 20% to 30% below that for the finite element model. The difference is greatest at the small crack lengths and decreases as the crack become long. This does not appear so in Figure 6-4 and Figure 6-5 because the compliance is significantly less at the shorter crack lengths than at the long crack lengths.

A reason for the difference between the two models could be short beam shear contribution, which would lead to the decreasing difference as the unbonded length increases. The deflection of the adherend in the analytical model is assumed to be that of a plate on an elastomeric foundation, and contribution to the compliance due to shear stress was not considered. This is considered in the finite element analysis, resulting in the difference of the compliance between the two. However, when the reaction force at the end of a cantilever beam with the Substrate X properties was compared between finite element and simple beam theory, the compliance for the simple beam theory solution was higher.

The difference between the finite element and analytical models could be the small deflection assumptions of the analytical model. The adherend and interlayer at the interface were assumed to deflection in the vertical direction only. The assumption of small deflections assumed that the deflections in the horizontal direction of the adherend were small enough to be considered zero. The deflections applied to the finite element model were kept small as to be considered small deflections ($\delta/a < 0.15$). However, the adherend of the finite element model did deflect in both the horizontal and vertical directions. These deflections that are not accounted for in the analytical model can lead to a greater amount of strain on the interlayer for the finite element model than the analytical model. A greater amount of strain in the interlayer would than lead to a greater compliance.

The difference between the finite element and analytical models could also be due to the finite length of the finite element model. The analytical model was prescribed an infinite length while

the finite element model, although very long in comparison to the other dimensions, does have a bonded area of finite length. This could lead to behavioral differences between the two. This could be addressed by introducing a finite length to the bonded area in the analytical model or by further increasing the bonded area in the finite element model.

Conclusions

It was determined that the finite element model of the hydrogel interlayer behaved in a similar manner for fully and nearly incompressible properties. The behavior of the two models appears similar by observation of the compliance as a function of the length of the debonded area. However, the compliance of the finite element model is 20% higher than the compliance of the analytical model. Reasons for this difference could be due to the following reasons: a greater amount of mobility in the interlayer, the definition of the behavior of the hydrogel interlayer, applying only half of the wedge test, and the absence of the crack growth in the finite element model. Confidence in the finite element model is increased by observing the complete model and adding crack growth in the cohesive zone model. Confidence in the finite element could be increased by further improvements in describing the interlayer. This would be done by repeating tests performed on the hydrogels, such as uniaxial testing, in Abaqus and refining the properties for the finite element model in order to match the results. Further testing on the hydrogels to find Poisson's ratio and hysteresis effects will allow to further improve the description of the finite element model.

Cohesive Zone Model

Methods

For the application of cohesive elements, the complete wedge test configuration was modeled. This was done by adding a second adherend to the bottom edge of the interlayer and adjusting the boundary conditions such that the mid-plane was no longer fixed and each adherend was pinned at one end. The displacement applied to the adherends was symmetrical in the amount and timing. Last of all, a layer of cohesive elements was added between the interlayer and the top adherend, as shown in Figure 6-6 with an exaggerated thickness for demonstration of their location.

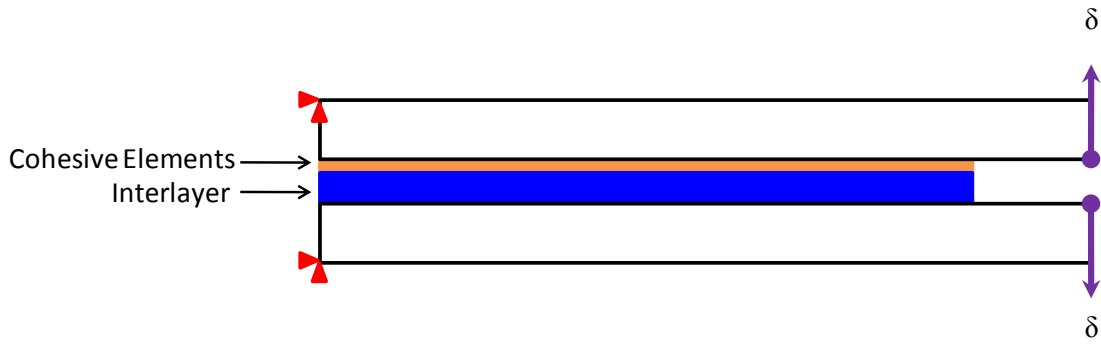


Figure 6-6: Finite Element Configuration for the CZM Method

The cohesive elements were placed at only one of the two interfaces under the assumption that the debonding only occurs at one interface. This assumption was made for the analytical model and was observed in the experimental results. This also prevented the hydrogel from debonding from both interface under the symmetrical loading.

The layer of cohesive elements spanned across the bonded area and was only one element deep. The cohesive elements had an aspect ratio of one and a fine mesh, $ES_{COH} = 0.01mm$, in order to ensure that there were multiple cohesive elements along the cohesive zone length [31]. Although the cohesive elements were very small, they were prescribed an effective thickness of unity. This allowed for interchanging the elastic modulus and stiffness, the traction and nominal stress, and the damage separations and nominal strain in the application of the linear traction-separation law.

Due to the increased computations necessary for the addition of the cohesive elements, the length of the entire model was reduced half to the length used during the manual crack growth method. This reduced the number of elements and nodes for the whole system and decreased the computation time. There were previous concerns of end effects with a shorter model but none appeared in the results. In addition, the thickness of the hydrogel interlayer was reduced in order to increase its effective stiffness and reduce possible computational error due to large amounts of strain.

A linear traction-separation law was applied to the cohesive elements by describing the interface with an effective stiffness, strength, and fracture energy. There are other options for the shape of the traction-separation law. The linear law is largely used for cohesive elements and suggested in the Abaqus literature. Other shapes were not attempted but would be an option in future work. The effective stiffness was estimated using the elastic modulus (E_a) and thickness of the hydrogel interlayer (h), as shown in Equation (6-5) [31].

$$K_{eff} = 50 \frac{E_a}{h} \quad (6-5)$$

The strength of the interface was estimated using a relationship between the elastic modulus of the interlayer, the fracture energy (G_c), the desired number of cohesive elements along the cohesive zone length (N_e), and the mesh size of the cohesive elements (S_e) [31].

$$T_{ult} = \sqrt{\frac{9\pi E_a G_c}{32 N_e S_e}} \quad (6-6)$$

A linear traction separation curve was assumed and the parameters determined for each system were checked by determining the related separation at failure (δ_f) and onset of damage (δ_o). The adhesion between each hydrogel and Substrate X is viscoelastic due to the viscoelastic nature of the hydrogels. This was shown through the application of time-temperature superposition (TTSP) to the experimental and analytical results. Although rate and temperature were not applied in the numerical analysis, the viscoelastic nature was considered by applying the critical and threshold SERR values as the fracture energy of the system to represent the limiting cases bounding the viscoelastic response. The cohesive element parameters were then determined for the critical and threshold behavior of the interfacial fracture that occurs. However, only the threshold behavior was modeled for Hydrogel B due to the critical parameters being unknown.

The parameters in Table 6-2 were applied to Hydrogel B with the exception of the interlayer thickness, which was $0.09mm$ for the CZM model. For the CZM model, Hydrogel A and Hydrogel B were assumed fully incompressible. The parameters for the cohesive elements at the Hydrogel B and Substrate X interface are presented in Table 6-3.

Table 6-3: Cohesive Element Parameters for Hydrogel B and Substrate X Interface

Fracture Energy	G_c	J/m^2	0.2
Max Stress	T_{ult}	kPa	30.49
Effective Stiffness	K_{eff}	MPa	125
Mesh Size	ES_{COH}	mm	0.01
Elements	COH2D4	4-node 2D cohesive elements	

The stress versus strain curve for the Hydrogel B cohesive elements is shown in Figure 6-7 and provides insight to their behavior.

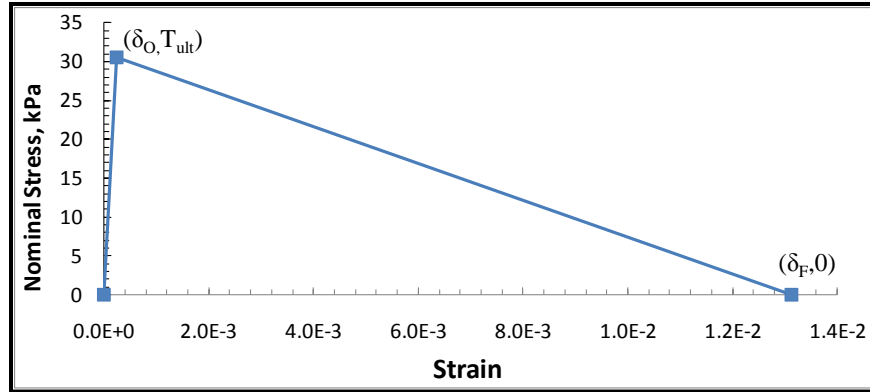


Figure 6-7: Nominal Stress versus Strain Curve for Hydrogel B Cohesive Elements

Damage occurs in the cohesive elements with only a small amount of strain applied. Once the stress reaches the strength of the interface, damage begins to occur in the cohesive elements. The damage increases as the stress decreases in a linear fashion until complete failure has occurred. The vast majority of the area under the curve is between the onset of failure and complete failure. This shows that the damage to the interface occurs with small strains applied, but then must accumulate in order to lead to failure. It is believed that this accurately portrays the weak adhesion between each soft hydrogel and Substrate X in which debonding occurs for small displacements.

The parameters in Table 6-2 were applied to Hydrogel A with the exception of the interlayer thickness, which was 0.09mm for the CZM model. The parameters for the cohesive elements at the Hydrogel A and Substrate X interface are presented in are shown in Table 6-4.

Table 6-4: Hydrogel A Parameters and Corresponding Cohesive Element Parameters

Fracture Energy	\mathcal{G}_c	J/m^2	0.2	16	16
Max Stress	T_{ult}	kPa	31.08	308.67	954
Effective Stiffness	K_{eff}	MPa	280	280	567
Mesh Size	ES_{COH}	mm	0.01	0.01	0.01
Elements	COH2D4	4-node 2D cohesive elements			

The stress versus strain curve for the Hydrogel A cohesive elements is shown in Figure 6-8 and provides insight to their behavior.

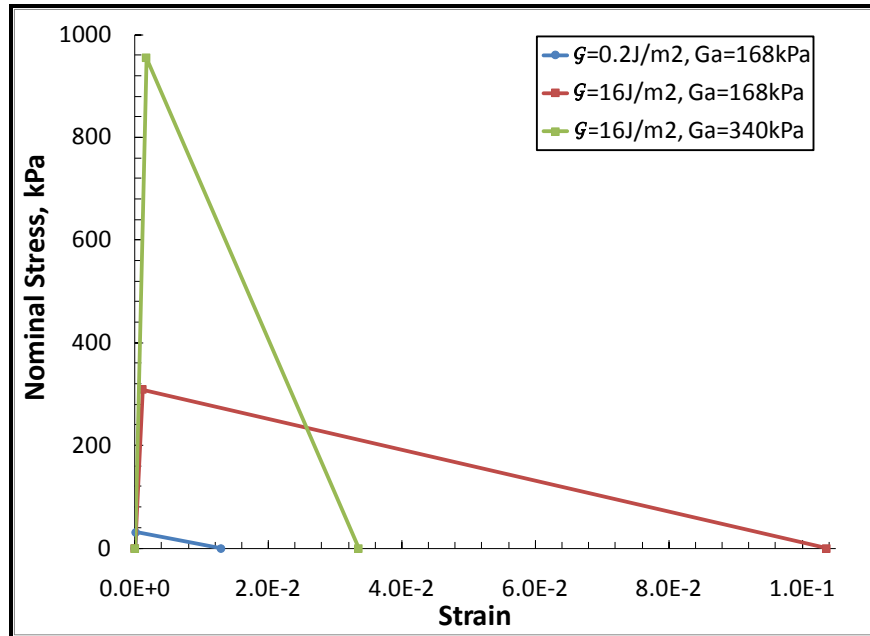
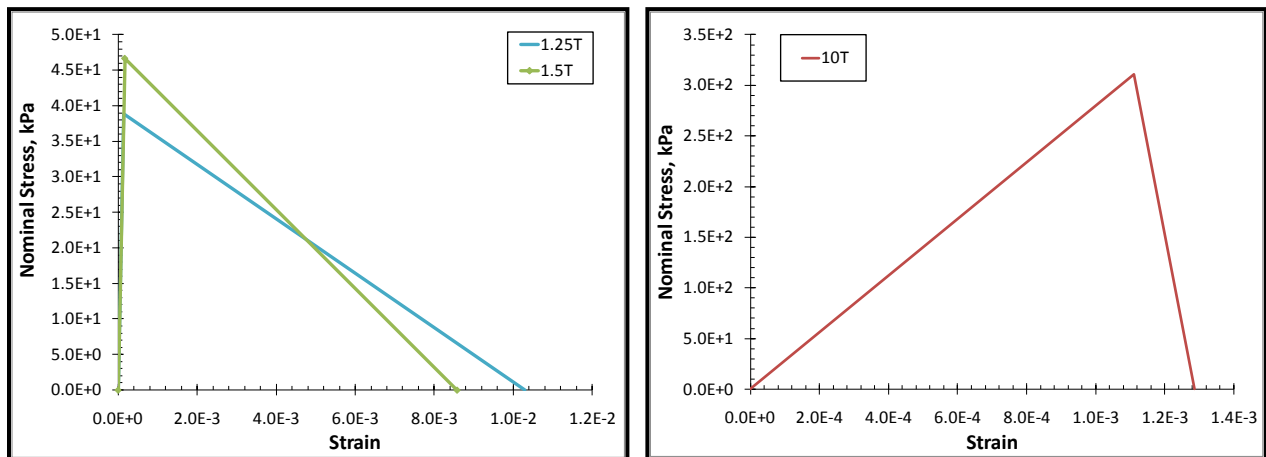


Figure 6-8: Nominal Stress versus Strain Curve for Hydrogel A Cohesive Elements

Two shear moduli values were applied for the Hydrogel A model in which the fracture energy was defined by the critical SERR value. The modulus of the interlayer was increased on the basis that temperature and rate affect the modulus of the interlayer. The majority of the critical SERR results from the experimental and analytical work was collected at lower temperatures and was described by an increased modulus. This shear modulus was applied to consider debonding occurring at the critical SERR based on the understanding the TTSP applies to the system.

In order to demonstrate the effect of changing the cohesive element parameters, the nominal stress and the stiffness, finite element models were ran with increased and decreased interface nominal stress and stiffness. The traction separation curves for these variations applied to the Hydrogel A model are shown below. The stiffness remained constant with varying the nominal stress and the nominal stress remained constant when varying the stiffness.



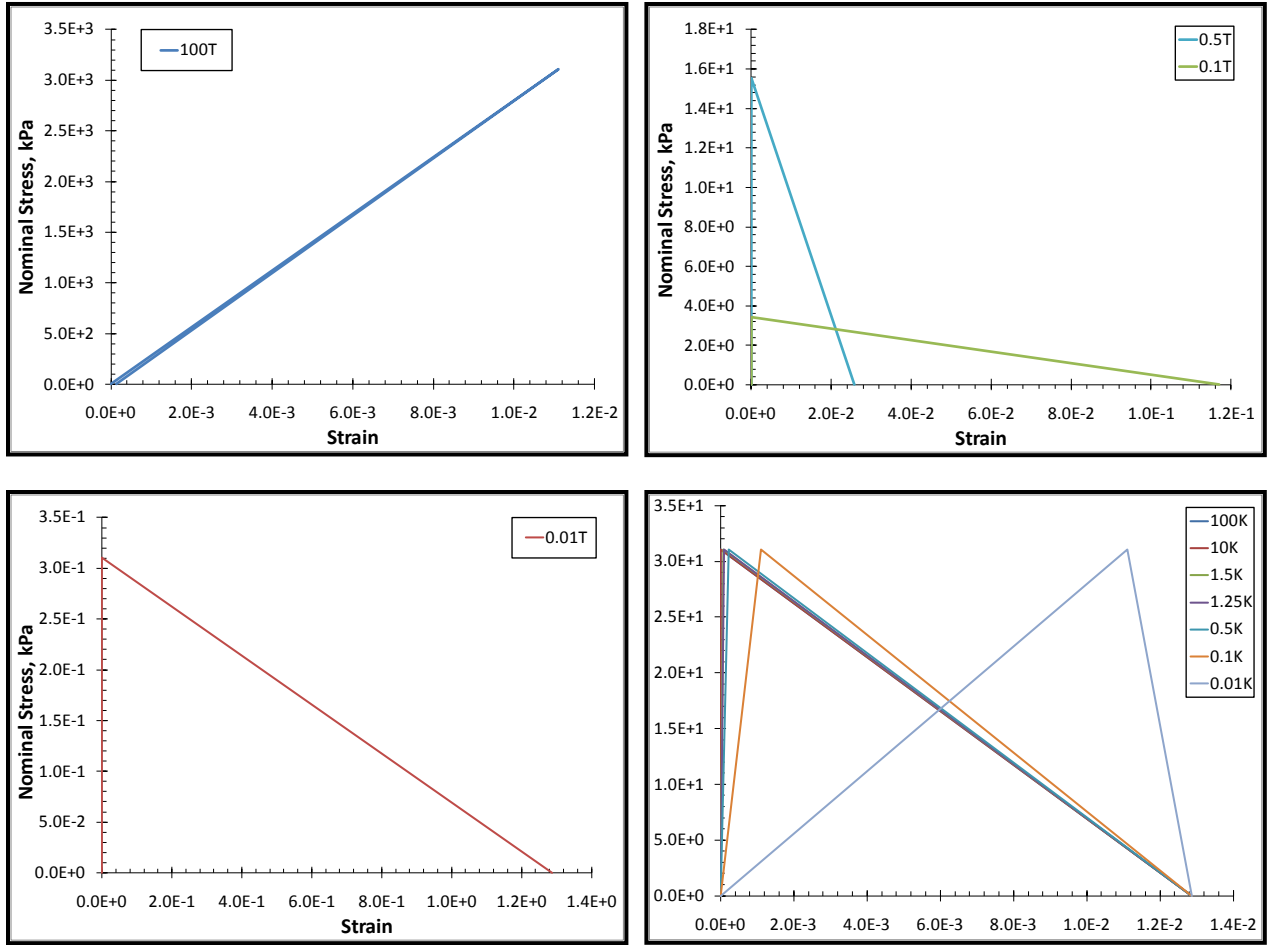


Figure 6-9: Separation versus Traction Curves for variations in Interface Stiffness and Nominal Stress for the Hydrogel A with $G=0.2J/m^2$

Results

Finite element models with initial debond lengths of $5mm$ and $10mm$ are compared to the analytical model in Figure 6-10 in which the compliance increases with increasing displacement and crack length.

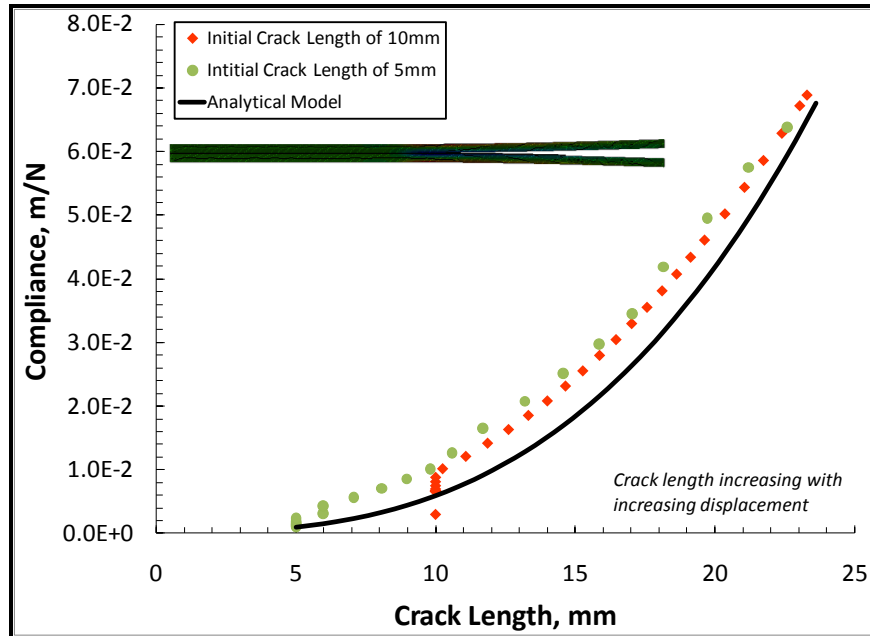


Figure 6-10: Increasing Compliance at Point of Loading with Increasing Displacement and Crack Length for Hydrogel B with $G=0.2J/m^2$

Each data set in Figure 6-10 ends at the maximum crack length reached for that model. The compliance of the numerical model is greater than that for the analytical model and approaches the analytical model as the crack length increases. The difference due to the behavior of the interlayer reduces as more of the adherend is free and no longer bonded to the interlayer.

The cohesive elements can be applied in order to model other geometries as well. However, it is important to note that the difficulty increases with increasing the hydrogel interlayer due to the effective stiffness decreasing. In addition, more material testing may be necessary for the hydrogels in order to ensure that appropriate material properties for more complex geometries are obtained.

Finite element models with initial debond lengths of $5mm$ and $10mm$ are compared to the analytical model in Figure 6-11 in which the compliance increases with increasing displacement and crack length.

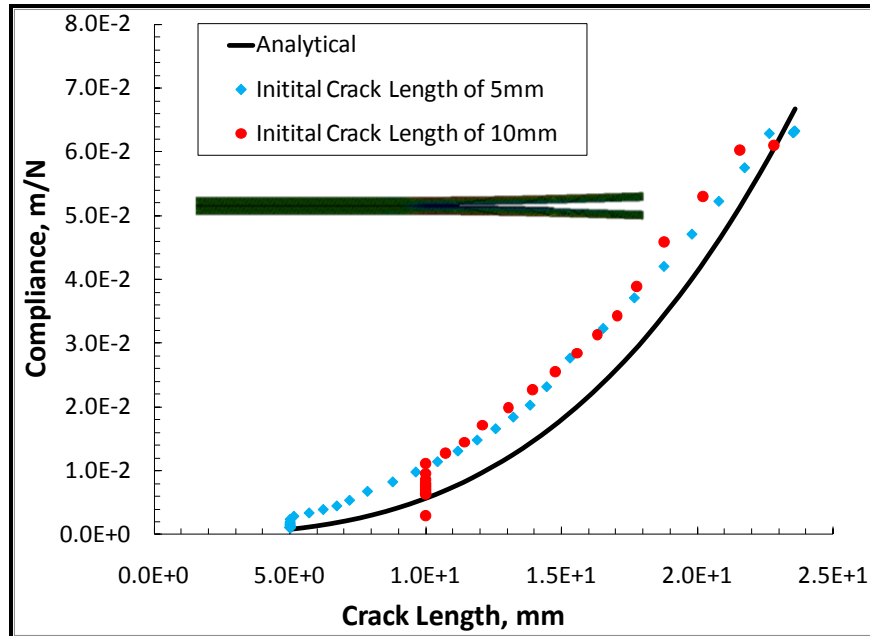


Figure 6-11: Increasing Compliance at Point of Loading with Increasing Displacement and Crack Length for Hydrogel A with $G=0.2J/m^2$

The finite element and analytical models compare to each other similarly to that shown for the Hydrogel B results in Figure 6-10. The effects on the compliance versus crack length curve of variations in interface nominal stress, shown in Figure 6-12, and interface stiffness, shown in Figure 6-13.

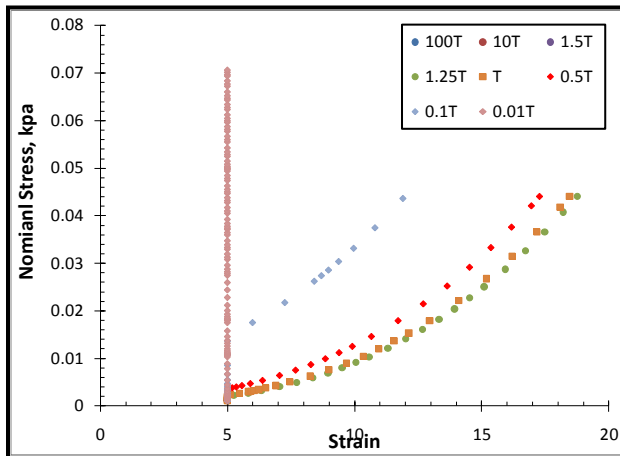


Figure 6-12: Compliance versus Crack Length for Variations in Interface Nominal Stress for Hydrogel A with $G=0.2J/m^2$

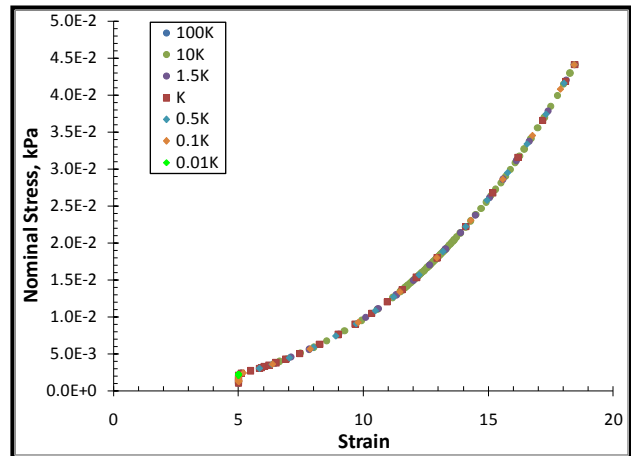


Figure 6-13: Compliance versus Crack Length for Variations in Interface Stiffness for Hydrogel A with $G=0.2J/m^2$

While maintaining constant interface stiffness, increasing the interface strength results in decreased compliance or for large numerical issues and decreasing the interface results in increased compliance. While maintaining constant interface strength, increasing or decreasing

the interface stiffness does not result in variation of the compliance. The results show that the interface stiffness can be approximated while much greater care must be given in determining the interface strength.

Crack growth did not occur for Hydrogel A models in which the critical SERR defined the fracture energy of the system. The hyperelastic material is capable of large strains that restrict high stresses from acting on the cohesive elements. By restricting stress acting on the cohesive element, damage does not accumulate enough to cause failure and debonding does not occur between the interlayer and adherend. In addition, the area of interlayer near at the crack tip had a higher ability to strain than the restricted area ahead of the crack tip. This caused the cohesive elements ahead of the crack tip to have a larger amount of damage, as shown Figure 6-14.

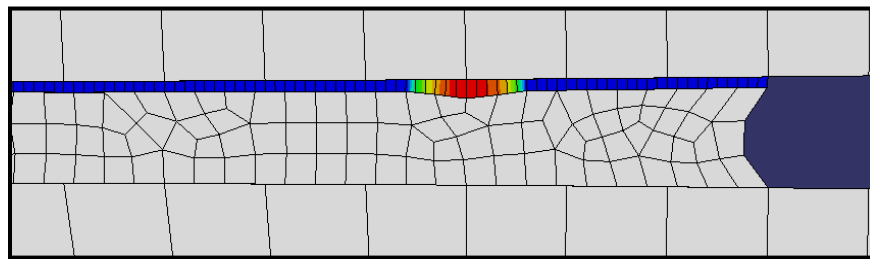


Figure 6-14: Damage of Cohesive Elements Ahead of the Crack Tip for Hydrogel A
Cohesive Elements with Fracture Energy of $16 J/m^2$

The effect observed in Figure 6-14 relates to the cavitation bubbles ahead of the crack tip that observed in other studies involving debonding between a soft and more rigid material [43]. Ghatak et al. determined that for thin adhesive film, bubbles will initially form ahead of the crack tip due to adhesion induced stability that will coalesce to form an undulating crack front prior to the crack moving forward [43]. To further show this, the critical SERR applied as the fracture energy of the interface was applied to models with a range of interlayer thickness, and thus confinement. The interlayer thickness was increased, causing the confinement of the interlayer to decrease. The difference in the resulting behavior is shown for these in Figure 6-15 to Figure 6-20, in which a displacement of 0.3mm was applied to each adherend and the stiffness remained constant for all models shown.

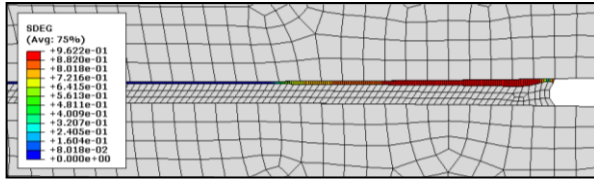


Figure 6-15: Cohesive Element Damage

$G_a=199kPa$, $G = 16J/m^2$, $T_{ult}=308.67kPa$, $h=0.09mm$

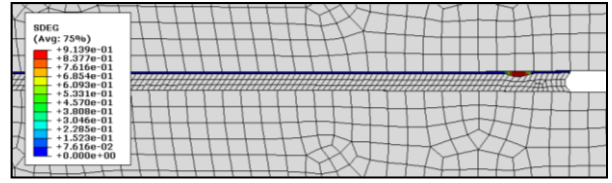


Figure 6-16: Cohesive Element Damage

$G_a=340kPa$, $G = 16J/m^2$, $T_{ult}=954kPa$, $h=0.09mm$

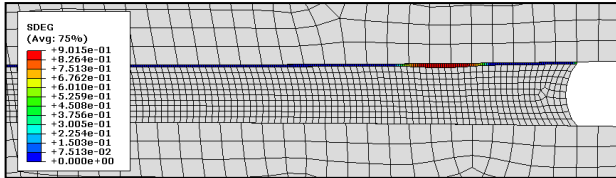


Figure 6-17: Cohesive Element Damage

$G_a=199kPa$, $G = 16J/m^2$, $T_{ult}=308.67kPa$, $h=0.27mm$

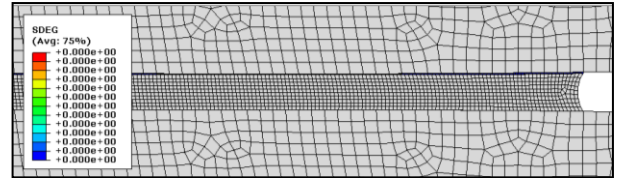


Figure 6-18: Cohesive Element Damage

$G_a=340kPa$, $G = 16J/m^2$, $T_{ult}=954kPa$, $h=0.27mm$

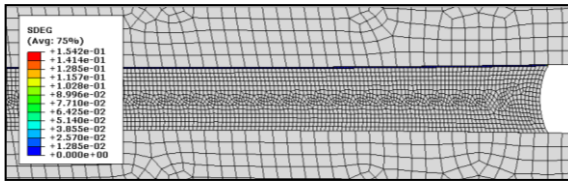


Figure 6-19: Cohesive Element Damage

$G_a=199kPa$, $G = 16J/m^2$, $T_{ult}=308.67kPa$, $h=0.45mm$

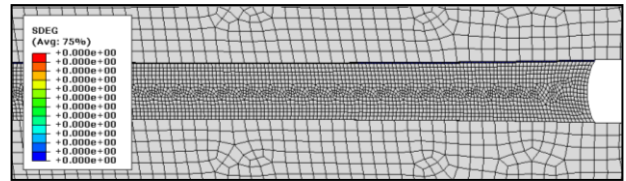


Figure 6-20: Cohesive Element Damage

$G_a=340kPa$, $G = 16J/m^2$, $T_{ult}=954kPa$, $h=0.45mm$

For both models, in which a low or high shear modulus was applied to the interlayer, the resulting behavior was dependent on the thickness of the interlayer. For the model in which a low shear modulus of the interlayer was applied, the interface elements stretched for the interlayer thickness of $0.09mm$. The cohesive element did not stretch when the interlayer thickness was increased to $0.27mm$, and a cavitation bubble ahead of the crack tip formed. No apparent damage occurred to the interface for an interlayer thickness of $0.45mm$. For the model in which a high shear modulus of the interlayer was applied, an interlayer thickness of $0.09mm$ had a cavitation bubble ahead of the crack tip. No apparent damage to the interface occurred for interlayer thicknesses of $0.27mm$ and $0.45mm$.

Comparisons of the compliance at the point of loading for the different levels of confinement are shown in Figure 6-21 and Figure 6-22.

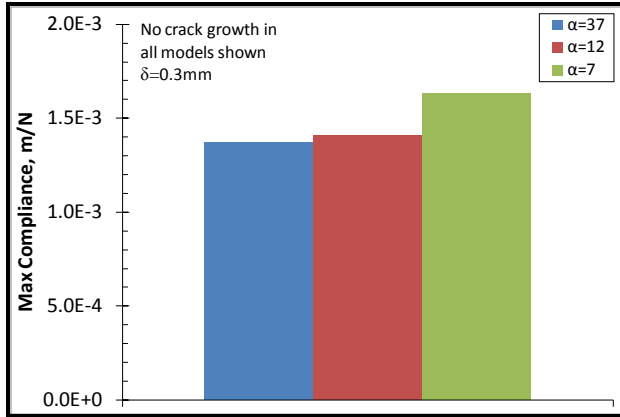


Figure 6-21: Max Compliance for $G_a=199kPa$, $\mathcal{G}=16J/m^2$, $T_{ult}=308.67kPa$, $\alpha=7$

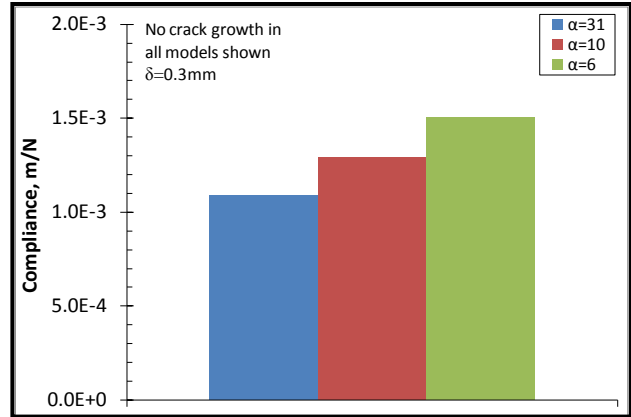


Figure 6-22: Max Compliance for $G_a=340kPa$, $\mathcal{G}=16J/m^2$, $T_{ult}=954kPa$, $\alpha=6$

For both models, the compliance increased with increasing thickness of the interlayer. This demonstrates the change in compliance that occurs with changing interlayer thickness and the need to compensate changing thickness with the analytical model. For the model in which a low shear modulus of the interlayer was applied, the compliance for the highest confinement was overestimated due to the interface elements significantly stretching.

It appears that the higher shear modulus applied to the model leads to more accurate results. That is, the interface does not stretch. The cavitation bubble ahead of the crack tip did show to be dependent on the thickness, and thus confinement, of the interlayer and was not apparent for greatest thickness evaluated for either model. This strengthens the possibility of the cavitation bubble being an indicator of undulating crack growth. However, the undulating crack growth can only be shown with the width of the sample. This means three dimensional modeling of the wedge test needs to be performed to better understand this effect.

Conclusions

A linear traction-separation law in combination with stress estimations based on the desired ratio of cohesive elements to the cohesive zone length was shown to work well in modeling the interfacial fracture between each hydrogel and the COP substrate. However, this was shown for the following restrictions: a thin hydrogel interlayer for increased effective stiffness that allowed for damage in the interface, separation of the threshold and critical fracture behavior since viscoelastic properties were not applied, and the insertion of the cohesive elements at only one interface to prevent debonding at both interfaces with the symmetrical loading. The compliance versus crack length curves showed similar behavior between the numerical and analytical models for the case of applying the threshold SERR as the fracture energy. The compliance for the numerical model was higher but approached the analytical model as the crack length increased. This behavior was due to the interlayer having a greater influence on the finite element model due to the reduced restrictions on its mobility. Crack propagation was not achieved in the case of applying the critical SERR of Hydrogel A as the fracture energy. However, the cavitation bubble

that appeared ahead of the crack tip is believed to be an indicator of the undulating crack growth that was observed during experimentation. The bubble ahead of the crack tip did not appear when the thickness of the interlayer was increased to cause decreased confinement. According to Ghatak, these bubbles will form in confined elastomers and coalesce to form a crack front prior to the crack propagating [43]. The finite element results representing the critical interfacial fracture behavior, capturing the behavior prior to crack growth and indicating undulating crack front. This theory could be validated through three-dimensional modeling of the wedge test.

Summary

The finite element results validated the analytical model in multiple ways. First, it was shown that the analytical model reacts to the shear modulus and thickness of the interlayer in a similar manner as the finite element model. Second, the shapes of the compliance versus crack length curves were similar between the two models but with the analytical model having lower compliance values. Last of all, the finite element results from applying the threshold and critical SERR values as the fracture energy for Hydrogel A showed behavior that would be expected for the assigned value. This provides confidence that the critical and threshold SERR values determined through experimental and analytical results are approximately correct.

Chapter 7: Conclusions

Key Observations and Conclusions

Experimental Methods

Experiments using S-IPN silicone hydrogels require precise procedures including:

- Ability to cure samples
 - The sample preparation needs to include the steps necessary for proper curing of the samples.
- Careful handling for the soft and sensitive nature of the hydrogels
 - The behavior of the materials was found to be very sensitive to changes in procedure or conditions. It was found that the procedure, from specimen preparation to testing, needed to be standardized and well documented.
 - Because the hydrogels were soft, measurements of the thickness were difficult. This was handled by taking multiple measurements and using a highly accurate thickness gauge.
 - Time was a major issue in early testing. Hydrogels should be tested shortly after curing to prevent the changes seen in the side studies. It was found that too large of a delay after curing could cause erratic results, bridging, debonding around the edges, and solvent loss.
- Ability to control temperature
 - An important aspect of working with hydrogels is their viscoelastic nature. To characterize the behavior, the response to changes in temperature and the crack propagation rate need to be known.

Analytical Model

The analytical model developed in Chapter 4 is a variation of the confined film model from Ghatak and Chaudhury [21] and included theory from Dillard, Lefebvre, and Komatsu [19, 20, 23]. The model was needed to analyze the results from the application of the experimental methods described in Chapter 3. The model had the following beneficial features:

- The deflections of the adherends in the bonded and debonded region were characterized. In addition, the deflections that occur within the interlayer and at the crack tip were established. This aided in comparing the analytical model to other analytical models and the finite element model.
- The energy contributions of the deformed interlayer and the adherends were considered when the strain energy release rate (SERR) was determined.
- Boundary conditions appropriate for the variation of the wedge test and the materials utilized were applied.

Experimental and Analytical Results

The experimental and analytical results provided parameters to describe the adhesion of each system of interest. The adhesion of each system could be compared to one another and to the cohesive fracture behavior of each hydrogel system. The parameters and insight gained on the adhesion of each system include the following:

- The WLF equation-based shift factors developed for the bulk behavior of the hydrogels worked well to develop the interfacial fracture master curve for each hydrogel to Substrate X. This implies that the viscoelastic characteristics of each hydrogel system played a large role in the adhesion between the hydrogel and Substrate X.
- The critical strain energy release rate for the interfacial fracture between Hydrogel A and Substrate X was determined to be about $16.3 J/m^2$. The critical strain energy release rate could not be determined for Hydrogel B, because the crack propagation rates were not high enough for Hydrogel B debonding to reach the critical region. For a similar temperature range, the crack propagation rates were not high enough to reach the critical region of the cohesive fracture master curve for Hydrogel B [4]. Some of the likely factors for Hydrogel B not reaching the critical region in the temperature and rate ranges investigated include the very low glass transition temperature of Hydrogel B and the higher amount of stretching at the crack tip.
- The threshold strain energy release rate for the interfacial fracture was determined to be 0.190 to $0.199 J/m^2$ for Hydrogel A and Hydrogel B. The similar values show that the two systems behave similarly at long crack lengths. In addition, these values are far below the threshold strain energy release rates for the cohesive fracture for both Hydrogel A and Hydrogel B. These were previously determined to be between 18 and $22 J/m^2$ [4].

Other testing, such as the investigation of the effects of aging, would provide further insight into the two systems and considerations for the application of these systems. The observations and conclusions of these side studies include the following:

- Time between curing and testing is a factor in the behavior of the system.
 - It was observed that increasing time between curing and inserting the wedge resulted in bridging. This was found to occur at room temperature. However, bridging did not occur with increasing time after curing for specimen tested at a low temperature of $4^{\circ}C$.
 - A pattern was not observed for the results of the wedge tests performed at discrete times after testing.
 - For Hydrogel A and Hydrogel B, a change of specimen thickness was not observed as time passed after curing. However, debonding would appear around the edges for both Hydrogel A and Hydrogel B specimens. This is likely due to the hydrogel pulling from the edges, due to residual stresses, and causing the thickness of the specimen to remain constant despite the changes occurring

visually. Such debonding could serve as multiple initiation sites that could lead to bridging.

- A change in the specimen mass was only observed for Hydrogel A. This led to the conclusion that Hydrogel A experiences a greater solvent loss than Hydrogel B as time after curing passes.

Numerical Results

The finite element and analytical models compared well to each other in the following ways:

- It was shown that the analytical model reacts to the shear modulus and thickness of the interlayer in a similar manner as the finite element model.
- The shapes of the compliance versus crack length curves were similar between the finite element and analytical models.

However, there are still issues with the comparison of the finite element and analytical models:

- The analytical model provided lower compliance values than the finite element model.

The finite element results provided confidence in the fracture parameters developed for each hydrogel system from the experimental and analytical results.

- The application of the threshold SERR for each system as the fracture energy of the finite element model resulted in behavior similar to that in the experimental results.
- The application of the critical SERR for each system as the fracture energy of the finite element model suggested the onset of an undulating crack front by the formation of a cavitation bubble ahead of the crack tip. This was representative of the type of crack growth observed during the application of the experimental methods.

Future work

Future work could build upon the insights this work presented into the adhesion and parameterization of each system.

Proposals for future experimental work on these systems include the following:

- Testing of Hydrogel B at higher rates and lower temperatures in order to characterize the critical region.
- The introduction of mode II fracture and mode mixity by using adherends of different thicknesses or applying displacement in an unsymmetrical fashion.
- Refined standards to further reduce the variation in the results.
- Develop an imaging method to validate the analytical model experimentally.

The accuracy of the analytical model could be increased by accounting for the role of the interlayer in the debonded region in which it remains bonded to one of the two adherends. Removing assumptions such as incompressibility, plane strain, and small deflections would

expand the model to other configurations and provide solutions for cases such as low confinement.

The finite element fracture models developed were useful in validating the analytical model and applying the fracture parameters determined through the experimental and analytical results. However, they could be refined with the following:

- The addition of viscoelastic properties to accurately replicate the behavior of the hydrogel. This could be done by building a correlation between the raw data collected and the finite element results.
- The development of parameter definitions unique to the materials involved, a soft interlayer and glassy adherends, and independent of the geometry and dimension in order to build more complex geometries while maintaining confidence in the finite element results.
- Improvement of the material definitions for the hydrogel interlayer
 - Perform additional experimental testing to find useful parameters such as the Poisson' ratio
 - Replications of bulk testing of the hydrogel in Abaqus to optimize parameters and bring the finite element results as similar to experimental results as possible.
 - Add cohesive fracture properties to the hydrogel interlayer.

References

1. Ottenbrite, R.M., *Biomedical Applications of Hydrogels Handbook*, K. Park and T. Okano, Editors, Springer: New York.
2. Petrie, E.M., *Handbook of Adhesives and Sealants*. 2007, New York: McGraw-Hill.
3. Shin, J.Y., et al. (2005) *Chemical Structure and Physical Properties of Cyclic Olefin Copolymers*. Pure Appl. Chem. **77**, 801-814 DOI: 0.1351/pac200577050801.
4. Tizard, G.A., *Characterization of the Viscoelastic Fracture of Solvated Semi-Interpenetrating Polymer Network (S-IPN) Silicone Hydrogels*, in *Engineering Mechanics*. 2010, Virginia Tech: Blacksburg. p. 104.
5. *Biomedical Applications of Hydrogels Handbook*, R.M. Ottenbrite, K. Park, and T. Okano, Editors. 2010, Springer: New York.
6. Anseth, K.S., C.N. Bowman, and L. Brannon-Peppas, *Mechanical Properties of Hydrogels and their Experimental Determination*. Biomaterials, 1996. **17**: p. 1647-1657.
7. Bistac, S., J. Guillemenet, and J. Schultz, *Fracture of Metal/Polymer/Metal Assemblies: Viscoelastic Effects*. The Journal of Adhesion, 2002. **78**: p. 987-996.
8. Brinson, H. and C. Brinson, *Polymer Engineering Science and Viscoelasticity: An Introduction*. 2008, New York: Springer Science+Business Media, LLC.
9. Adams, R.D., et al., *The Relative Merits of the Boeing Wedge Test and the Double Cantilever Beam Test for Assessing the Durability of Adhesively Bonded Joints*. International Journal of Adhesion and Adhesives, 2009. **29**(6): p. 609-620.
10. *ASTM D3762: Standard Test Method for Adhesive-Bonded Surface Durability of Aluminum*. 2003, ASTM International: West Conshohocken, PA.
11. *ISO 10354: Characterization of durability of structural-adhesive-bonded assemblies*. 1992, International Organization for Standardization: Geneva, Switzerland.
12. Ratta, V., *Crystallization, Morphology, Thermal Stability and Adhesive Properties of Novel High Performance Semicrystalline Polyimides*. 1999, Virginia Polytechnic Institute and State University.
13. Wang, C.H., *Introduction to Fracture Mechanics*, D.o. Defence, Editor. 1996, DSTO Aeronautical and Maritime Research Laboratory: Melbourne.
14. Anderson, T.L., *Fracture Mechanics: Fundamental and Applications*. Third ed. 2005, Boca Raton: CRC Press.
15. Pocius, A.V., D.A. Dillard, and M.K. Chaudhury, *The Mechanics of Adhesion*. Adhesion Science and Engineering, ed. A.V. Pocius. 2002, Amsterdam: Elsevier Science B.V.
16. Biel, A. and U. Stigh, *An Analysis of the Evaluation of the Fracture Energy using the DCB Specimen*. Arch. Mech., 2007. **59**(4-5): p. 311-327.
17. Erpolat, S., et al. (2004) *On the Analytical Determination of Strain Energy Release Rate in Bonded DCB Joints*. Engineering Fracture Mechanics **71**, 1393-1401.

18. Kanninen, M.F., *An Augmented Double Cantilever Beam Model for Studying Crack Propagation and Arrest*. International Journal of Fracture, 1973. **9**(1): p. 83-92.
19. Komatsu, K., H. Sasaki, and T. Maku, *Strain Energy Release Rate of Double Cantilever Beam Specimen with Finite Thickness of Adhesive Layer*. Wood research : bulletin of the Wood Research Institute Kyoto University, 1976. **59/60**: p. 80-92.
20. Lefebvre, D.R., D.A. Dillard, and H.F. Brinson, *The Development of a Modified Double-Cantilever-Beam Specimen for Measuring the Fracture Energy of Rubber to Metal Bonds*. Experimental Mechanics, 1988. **28**(1): p. 38-44.
21. Ghatak, A., L. Mahadevan, and M.K. Chaudhury, *Measuring the Work of Adhesion between a Soft Confined Film and a Flexible Plate*. Langmuir, 2005. **21**: p. 1277-1281.
22. O'Brien, S.B.G. and L.W. Schwartz, *Theory and Modeling of Thin Film Flows*, in *Encyclopedia of Surface and Colloid Science*. 2002, Marcel Dekker, Inc. p. 5283-5297.
23. Dillard, D.A., *Bending of Plates on Thin Elastomeric Foundations*. Journal of Applied Mechanics, 1989. **56**: p. 383-386.
24. Banks, H.T., G.A. Pinter, and H. Yeoh, *Analysis of Bonded Elastic Blocks*. Mathematical and Computer Modelling, 2002. **36**.
25. Adda-Bedia, M. and L. Mahadevan, *Crack-front instability in a confined elastic film*. Proc. R. Soc., 2006. **462**: p. 3233-3251.
26. Reddy, J.N. (2006) *An Introduction to the Finite Element Method*.
27. *Abaqus 6.9 Documentation*. 2009, Dassault Systèmes Simulia Corp: Providence, RI, USA.
28. Burlayenko, V.N. and T. Sadowski, *FE Modeling of Delamination Growth in Interlaminar Fracture Specimens*. Budownictwo i Architektura, 2008. **2**: p. 95-109.
29. Diehl, T., *On Using a Penalty-Based Cohesive-Zone Finite Element Approach, Part I: Elastic Solution Benchmarks*. International Journal of Adhesion & Adhesives, 2008. **28**: p. 237-255.
30. Ferracin, T., et al., *On the Determination of the Cohesive Zone Properties of an Adhesive Layer from the Analysis of the Wedge-Peel Test*. International Journal of Solids and Structures, 2003. **40**(11): p. 2889-2904.
31. Turon, A., et al., *An engineering solution for mesh size effects in the simulation of delamination using cohesive zone models*. Engineering Fracture Mechanics, 2007. **74**(10): p. 1665-1682.
32. Bouvard, J.L., et al., *A cohesive zone model for fatigue and creep-fatigue crack growth in single crystal superalloys*. International Journal of Fatigue, 2009. **31**(5): p. 868-879.
33. Dugdale, D.S., *Yielding of steel sheets containing slits*. Journal of the Mechanics and Physics of Solids, 1960. **8**(2): p. 100-104.
34. Barenblatt, G.I., *The Mathematical Theory of Equilibrium Cracks in Brittle Fracture*, in *Advances in Applied Mechanics*. 1962, Elsevier. p. 55-129.

35. Xie, D. and S.B.B. Jr., *Progressive Crack Growth Analysis using Interface Element based on the Virtual Crack Closure Technique*. Finite Elements in Analysis and Design, 2006. **42**(11): p. 977-984.
36. Gustafson, P.A. and A.M. Waas. *Efficient and Robust Traction Laws for the Modeling of Adhesively Bonded Joints*. in *49th AIAA/ASME/ASCE/AHS/ASC Structures, Structural Dynamics, and Materials Conference*. 2008. Schaumburg, IL: American Institute of Aeronautics and Astronautics, Inc.
37. Adda-Bedia, M. and L. Mahadevan (2006) *Crack-front instability in a confined elastic film*. Proceedings of the Royal Society A.
38. *MatWeb: The online Materials Information Reference*. 2010, Automation Creations, Inc.
39. Timoshenko, S.P. and S. Woinowsky-Krieger, *Theory of Plates and Shells*. 1959, McGraw-Hill.
40. Gent, A.N. and E.A. Meinecke, *Compression, bending, and shear of bonded rubber blocks*. Polymer Engineering & Science, 1970. **10**(1): p. 48-53.
41. Park, S.W. and Y.R. Kim, *Fitting Prony-Series Viscoelastic Models with Power-Law Presmoothing*. Journal of Materials in Civil Engineering, 2001.
42. Williams, J.G., *Fracture Mechanics of Polymers*. 1984, Halsted Press: Chinchester, New York.
43. Ghatak, A. and M.K. Chaudhury, *Adhesion-Induced Instability Patterns in Thin Confined Elastic Film*. Langmuir, 2003. **19**: p. 2621-2631.

Appendix A: Determining Mesh Size for Adherends

Three-point bending was performed on the adherend within Abaqus to compare the results for different mesh sizes to expected behavior. The material and section properties applied are presented in Table A.1.

Table A.1: Material and Section Properties Applied to Adherend Material in Abaqus

Material behavior	Elastic
Material Type	Isotropic
Young’s Modulus	2.1GPa
Poisson’s Ratio	0.41
Length	70mm
Thickness	0.7mm
Section Type	Solid, Homogenous

The resulting behavior for different mesh sizes was compared to the expected behavior. The following mesh sizes were prescribed: 0.035 mm, 0.07 mm, 0.1 mm, 0.2 mm, and 0.35 mm. An image of the loading applied and the resulting behavior for an element size of 0.35mm is shown in Figure A.1..

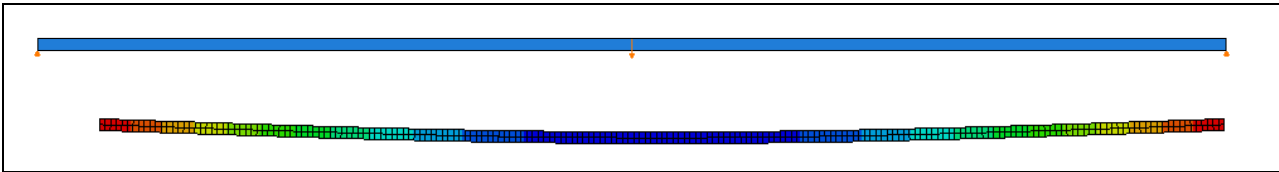


Figure A.1: Three-Point Bending of Adherend in Abaqus (Element Size=0.35mm)

The deflection and reaction force at the point of loading are plotted along with the expected behavior using simple beam theory in Figure A.2.

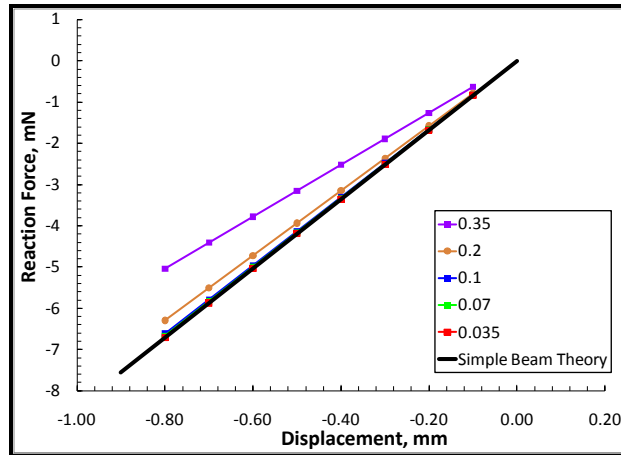


Figure A.2: Reaction Force versus Displacement for Abaqus Three Point-Bend Tests

The force-displacement curves appear to align well with the expected curve, with the exception of the two largest element sizes observed, 0.2 mm and 0.35 mm . The results for each mesh size are compared to simple beam behavior in Tale A.2.

Table A.2: Results for Abaqus Three-Point Bend Tests

Mesh Size (mm)	Final Reaction Force (mN)	Percent Error wrt SBT(%)
0.035	-6.71	-0.17
0.070	-6.1	-0.79
0.100	-6.61	-1.58
0.200	-6.29	-6.35
0.350	-5.04	-24.97

The three smaller mesh sizes of 0.035 mm , 0.07 mm , and 0.1 mm have a percent error compared to the simple beam theory solution of less than 2%.

Appendix B: Finite Element Cohesive Zone Models

Images of the finite element models with the cohesive element parameters presented in Chapter 5 are shown in Figures B.1 to B.4.

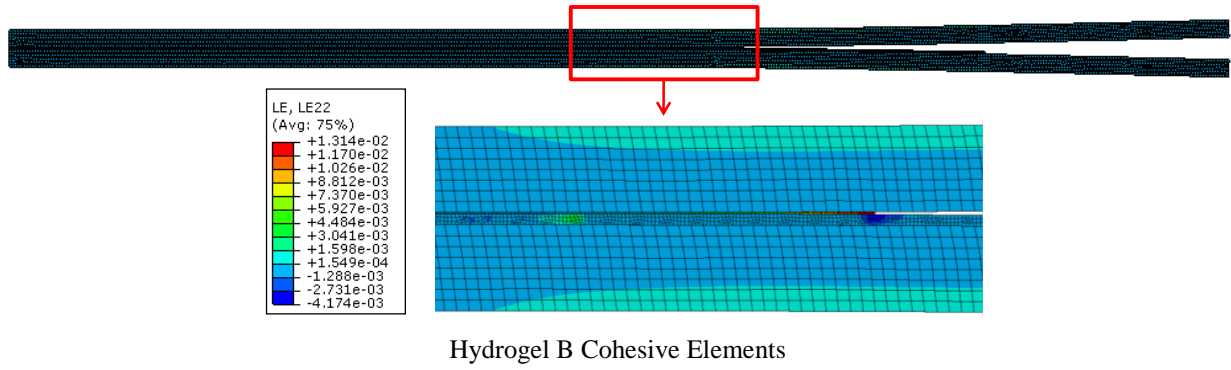


Figure B.1: $G_c = 0.2 \text{ J/m}^2$, $T_{ult} = 30.49 \text{ kPa}$, $E_{COH} = 1.25E5 \text{ kPa}$, $a_0 = 10 \text{ mm}$

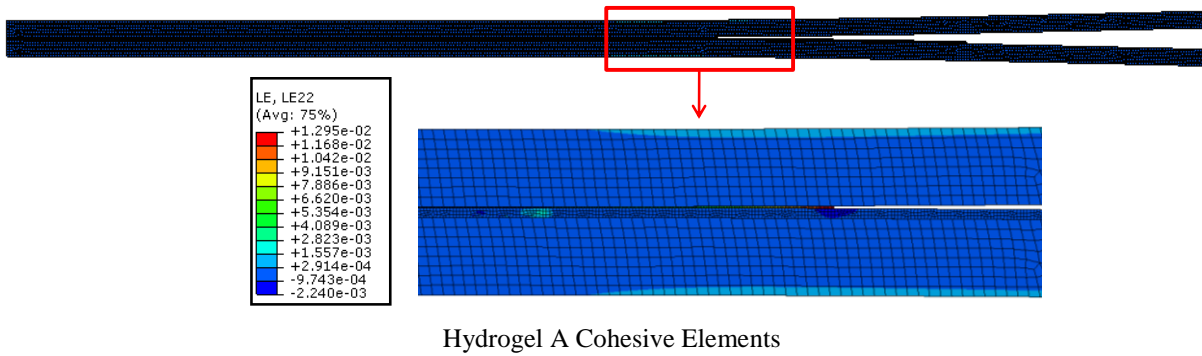


Figure B.2: $G_c = 0.2 \text{ J/m}^2$, $T_{ult} = 30.08 \text{ kPa}$, $E_{COH} = 2.80E5 \text{ kPa}$, $a_0 = 10 \text{ mm}$

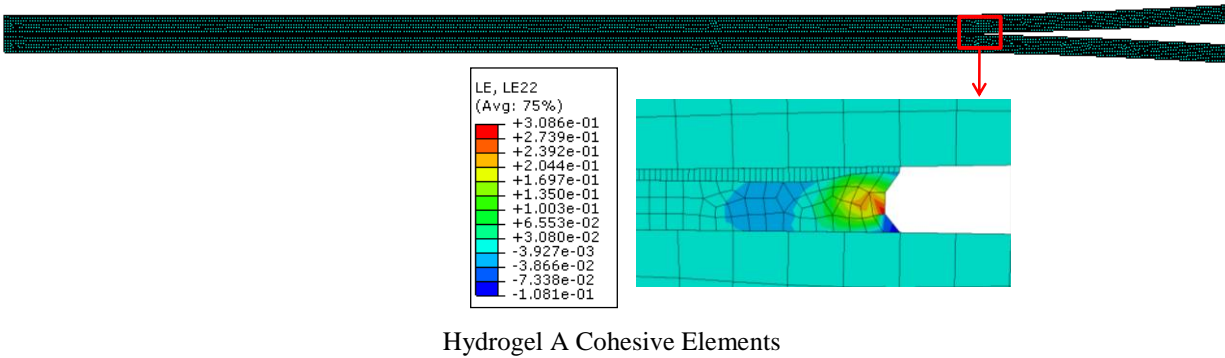
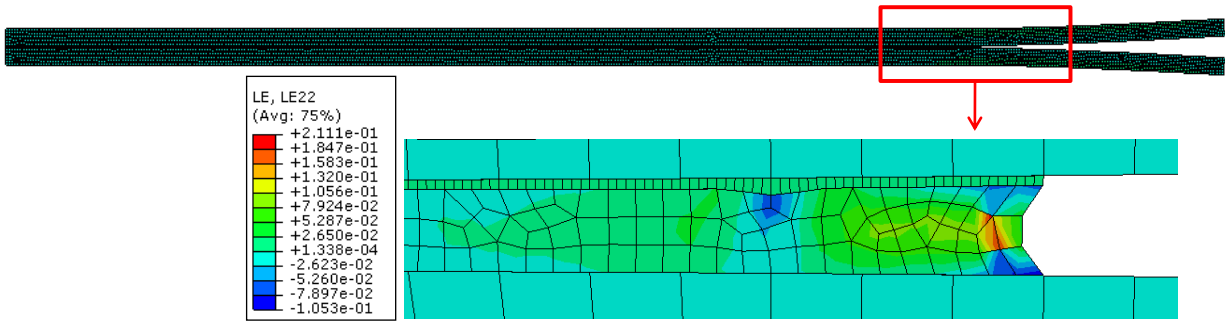


Figure B.3: $G_c = 16 \text{ J/m}^2$, $T_{ult} = 308.67 \text{ kPa}$, $E_{COH} = 2.80E5 \text{ kPa}$, $a_0 = 10 \text{ mm}$



Hydrogel A Cohesive Elements

Figure B.4: $G_c = 16 \text{ J/m}^2$, $T_{ult} = 954 \text{ kPa}$, $E_{COH} = 5.67E5 \text{ kPa}$, $a_0 = 10\text{mm}$